

Current State-of-the-Art in the Interface/Surface Modification of Thermoelectric Materials

Shiyang He, Sebastian Lehmann, Amin Bahrami,* and Kornelius Nielsch*

Thermoelectric (TE) materials are prominent candidates for energy converting applications due to their excellent performance and reliability. Extensive efforts for improving their efficiency in single-/multi-phase composites comprising nano/micro-scale second phases are being made. The artificial decoration of second phases into the thermoelectric matrix in multi-phase composites, which is distinguished from the second-phase precipitation occurring during the thermally equilibrated synthesis of TE materials, can effectively enhance their performance. Theoretically, the interfacial manipulation of phase boundaries can be extended to a wide range of materials. High interface densities decrease thermal conductivity when nano/micro-scale grain boundaries are obtained and certain electronic structure modifications may increase the power factor of TE materials. Based on the distribution of second phases on the interface boundaries, the strategies can be divided into discontinuous and continuous interfacial modifications. The discontinuous interfacial modifications section in this review discusses five parts chosen according to their dispersion forms, including metals, oxides, semiconductors, carbonic compounds, and MXenes. Alternatively, gas- and solution-phase process techniques are adopted for realizing continuous surface changes, like the core-shell structure. This review offers a detailed analysis of the current state-of-the-art in the field, while identifying possibilities and obstacles for improving the performance of TE materials.

1. Introduction

Thermoelectric (TE) materials are auspicious candidates for direct thermal-to-electrical energy conversion applications and sustainable energy solutions, owing to their combined heat and electricity attributes. The key challenge for enhancing the performance of TE materials is establishing a balance between their property indicators in the equation describing their dimensionless figure of merit (zT) value (Equation (1)).^[1,2]

$$zT = S^2 \sigma \kappa^{-1} T \quad (1)$$

where S , σ , κ , and T are the Seebeck coefficient, electrical conductivity, total thermal conductivity, and absolute temperature, respectively. The total thermal conductivity comprises the contributions^[3] the from lattice vibrations (κ_l) and charger carriers (κ_e) and can be expressed by $\kappa = \kappa_l + \kappa_e$. High zT values require a high power factor ($S^2 \sigma$, PF) and a low total thermal conductivity.^[4] The energy conversion efficiency (η) of TE materials in conventional TE generators is determined by the zT value, and can be presented by Equation (2):^[5]

$$\eta = \frac{T_h - T_c}{T_h} \frac{\sqrt{1 + zT} - 1}{\sqrt{1 + zT} + \frac{T_h}{T_c}} \quad (2)$$


where T_h , T_c , and T are the hot-side temperature, cold-side temperature, and average temperature of the TE material. Although enhancing the temperature gradient ($T_h - T_c$) benefits the improvement of the conversion efficiency, different TE materials exhibit optimum TE performance in different temperature ranges; therefore, the desired TE materials should be selected within a given temperature range. To realize a higher η , higher zT values are generally required for various temperature ranges. Overall, TE materials with zT values higher than 1 are preferred for practical applications in TE generators. If a TE material with a zT value exceeding 3 is used, the corresponding η would be high enough to replace traditional power generators/refrigerators with TE generators.^[6]

However, optimizing the TE performance is a relatively complex task, due to the intercorrelation between the transport parameters,^[7] making obtaining a zT value of 3 challenging. It

S. He, S. Lehmann, A. Bahrami, K. Nielsch
Institute for Metallic Materials
Leibniz Institute of Solid State and Materials Science
01069 Dresden, Germany
E-mail: a.bahrami@ifw-dresden.de; k.nielsch@ifw-dresden.de

S. He, K. Nielsch
Institute of Materials Science
Technische Universität Dresden
01062 Dresden, Germany

K. Nielsch
Institute of Applied Physics
Technische Universität Dresden
01062 Dresden, Germany

 The ORCID identification number(s) for the author(s) of this article can be found under <https://doi.org/10.1002/aenm.202101877>.

© 2021 The Authors. Advanced Energy Materials published by Wiley-VCH GmbH. This is an open access article under the terms of the Creative Commons Attribution-NonCommercial-NoDerivs License, which permits use and distribution in any medium, provided the original work is properly cited, the use is non-commercial and no modifications or adaptations are made.

DOI: 10.1002/aenm.202101877

should be noted that the S , σ , and κ parameters are intercorrelated by Equations (3)–(5):^[8]

$$\sigma = ne\mu \quad (3)$$

$$S = \frac{8\pi^2 k_B^2 T}{3eh^2} m^* \left(\frac{\pi}{3n} \right)^2 \quad (4)$$

$$\kappa = \kappa_1 + L\sigma T \quad (5)$$

where n , e , μ , h , k_B , m^* , and L stand for the carrier concentration, elementary charge, mobility, Planck constant, Boltzmann constant, carrier effective mass near the Fermi level, and temperature-dependent Lorenz number, respectively. For a degenerated semiconductor with parabolic band dispersion, assuming that the dopant does not alter the scattering or band structure, the Equation (4) for S is valid.^[8] Therefore, how to decouple the PF and κ is still a challenge in the TE field. In recent decades, numerous strategies were applied to investigate the rational design and development of TE materials. The main concepts for optimizing the zT value converge toward two approaches: i) enhancing the PF in terms of electrical properties by point-defect engineering,^[9–11] band engineering,^[12–14] texturing,^[15–17] and energy filtering;^[18–20] ii) decreasing the independent lattice thermal conductivity via nanostructuring,^[21–23] phonon engineering,^[24–26] interfacial modifications,^[27–29] or searching for new TE materials with intrinsically low thermal conductivity.^[30–32]

Single-phase TE materials have been thoroughly investigated, including PbTe,^[33–35] SnSe,^[36–38] Cu₂Se,^[39–41] and Bi₂Te₃-based alloys,^[42,43] skutterudites,^[44–46] Mg₃Sb₂,^[47–49] and Half-Heusler alloys,^[50,51] which can achieve zT values above 1 by element doping; however, their zT values can be further enhanced through the aforementioned strategies. Thus, the introduction of new materials into TE multiphase composites is another prominent approach attracting major scientific interest. When following the conventional melting route, second phases may occur and disperse heterogeneously in the TE material due to the nonequilibrium state; however, a uniform distribution can be achieved by directly dispersing the nanoparticles or forming a core-shell structure (Figure 1). Depending on the modification methods, the techniques of dispersion decorating or second-phase coating could establish discontinuous interfaces or continuous interfaces, respectively, between the matrix and the second phases. It should be noted that surface modification approaches provide the possibility to combine different dispersions and matrices in such a way that two or more constituents with different thermodynamic stability conditions can be gathered in one system, endowing the final system with their specific advantageous characteristics. Furthermore, as opposed to other alteration methods (e.g., phase precipitation), the resulting chemical composition can be more finely tuned.

Interfacial modifications can carry a highly beneficial effect in that a second phase on the interface can boost the material's thermoelectric properties in a variety of ways. In regard to thermal transport, heat flow tends to bypass the dispersion when the κ of the matrix is higher than that of the dispersion.^[52] Owing to the larger mismatch in the acoustic impedance or phonon spectra between the second phase and the matrix phase, the introduced high-density interfaces between the dispersed

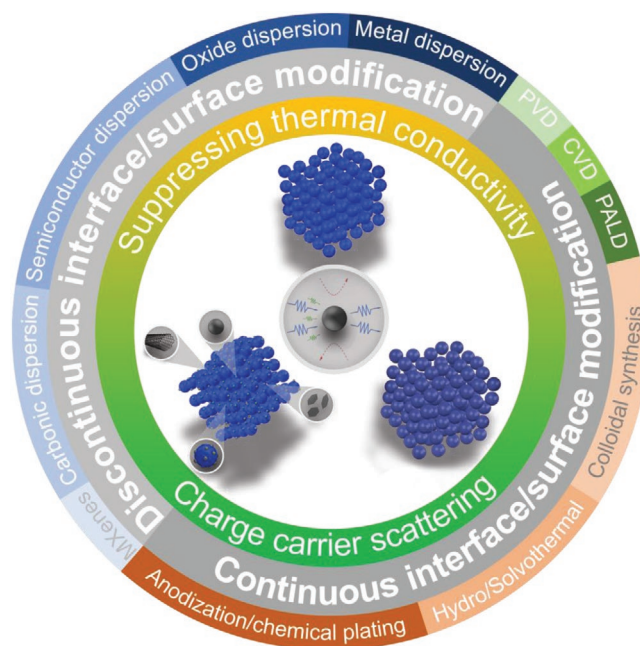


Figure 1. Schematic illustration of discontinuous interfacial modifications with different dispersions and continuous interfacial modifications with core-shell structure, resulting in low energy carrier scattering and phonon scattering.

nanoparticles and matrix are more effective in phonon scattering than normal grain boundaries. According to theoretical calculations, by increasing the dispersion size and thickness of the second phase coating, the second phase scatters phonons from short to long wavelengths.^[53] Because of the mid-wavelength phonon scattering, the scattering will be more effective if the second phase is properly selected in terms of dispersion concentration/size or thickness of the second phase coating, allowing for the zT values to be further improved.^[54] In terms of electrical transport, S can be enhanced by a mechanism known as electron energy filtering,^[55] as well as by modifying the resistance between the dispersion and the matrix. This is achieved by curving the electron bands at the interfaces between the second phase and the bulk matrix, enabling the high-energy electrons pass, while scattering the low-energy electrons. This selective scattering procedure can increase the value of S , and therefore requires the appropriate materials to be used as second phases so as to ensure a beneficial band bending. However, research in the literature corroborating this energy filtering effect (e.g., carrier concentration, mobility/homogeneity of second phase) remains scarce.^[56–58] Consequently, the energy filtering mechanism responsible for the PF boosting will be further investigated.

In this review, the most prominent interfacial modification techniques currently used for inorganic materials were categorized into two main parts according to the interface morphological features: i) discontinuous interfacial modifications and ii) continuous interfacial modifications. The discontinuous interfacial modifications contain different sections, namely, metals, oxides, semiconductors, carbonic materials, and MXenes. To form the core-shell structure, the continuous interfacial modification technique can be accomplished through gas-phase deposition or a wet chemical route. Methods for modifying interfaces in organic TE

materials have been discussed elsewhere.^[6,59,60] Here, we summarize the advancements regarding the interfacial modification of inorganic TE materials for the purpose of enhancing the electrical properties or reducing the thermal conductivity. Finally, the current challenges and outlook for future developments in thermoelectric nanocomposites are discussed. We hope for our work to serve as a systematic overview of the state-of-the-art in the field and help determine the opportunities and challenges for boosting the thermoelectric performance of TE materials.

2. Discontinuous Interface Modification

The dispersion of the second phase into the TE material matrix is an essential approach for improving the thermoelectric properties. It should be noted that the dispersion of the second phase differs from the precipitation which occurs mostly during the cooling stage of the synthetic process. In the process of thermal transport, owing to the middle-length phonon scattering and thermal resistance between the dispersion and matrix interfaces, a high decrease in lattice thermal conductivity that is unaffected by carrier transportation, can be expected. Meanwhile, in terms of electrical transport, the energy filtering can be considered when nano-inclusions are embedded into the matrix-forming heterostructures. There are mainly two key factors underlying the influence of the carriers on the electrical properties: i) the interface density and ii) the band alignment between the TE matrix materials and nano-inclusions. The interface density might be altered by the size and volume/weight fraction of the matrix and the dispersion. Additionally, the rate of nucleation and growth can be regulated through the appropriate selection of precursors and synthetic methods applied on both the matrix and the dispersion, especially when using solution-processed chemical synthetic methods. Band alignment can be adjusted by selecting dispersion materials matching the electronic band structure (e.g., bandgap, work function, or electron affinity) that can form suitable charge carrier traps or barriers.^[61] A controlled potential barrier for energy filtering is expected to be optimized in the PF enhancement as reported by previous theoretical

studies. Faleev^[62] et al. proposed that in a semiconductor matrix with randomly dispersed metallic particles, only a certain fraction of the charge carriers is captured by the potential barrier. Within the framework of the Born approximation, the scattering relaxation time^[63] with scattering centers of dispersion-matrix interfaces, can be expressed by Equation (6):

$$\tau_i(E) = E^{-\frac{3}{2}} \frac{1 + 2E/E_g}{(1 + E/E_g)^2} \frac{x}{R} \frac{3\xi(E, R)}{4\sqrt{2m^*}} \quad (6)$$

Here, $\xi(E, R) = \int_0^{2kR} \left| \int_1^\infty \sin(\gamma t) V(\gamma R) \gamma dy \right|^2 t dt$. x , R , and E_g are the volume fraction, average radii of the potential barrier E_b , and direct energy gap, respectively. $\xi(E, R)$ is a variable function that depends on E . The potential barrier E_b is determined by the work functions and band alignment of matrix and second phase. Here, we only considered the ideal case where the essential electronic properties are described by the band structure and the position of the Fermi levels, and we limited the discussion to n-type semiconductors. When the two materials are brought into contact, the alignment of the Fermi levels causes the flow of charge from one material to the other. The direction of the charge flow depends on the relative difference between the work function of the metal (ϕ_M) and the electron affinity (χ_{SC}) of the semiconductor. If the ϕ_M is larger than χ_{SC} , the metal is theorized as possessing a high work function. Contrarily, a low work function metal implies that ϕ_M is smaller than χ_{SC} .

We consider the first case where the metal has a high work function forming Schottky barriers (**Figure 2a**); thus, electrons flow from the semiconductor to the metal, inducing a negatively charged surface on the latter and a positively charged surface on the former. The surface charge will be screened by electrons in the vicinity to keep the band diagram unperturbed deep inside the body. For the metal, the screening length is in the several-Angstroms range, due to their high carrier density of $\approx 10^{22} \text{ cm}^{-3}$.^[55] For the semiconductor, the screening length is much longer, with the lower carrier densities ranging from $\approx 10^{17}$ to 10^{20} cm^{-3} .^[55] Therefore, the overall charge on the boundary is negative. Obviously, the accumulation of negative charge (electrons) is energetically unfavorable, thus the

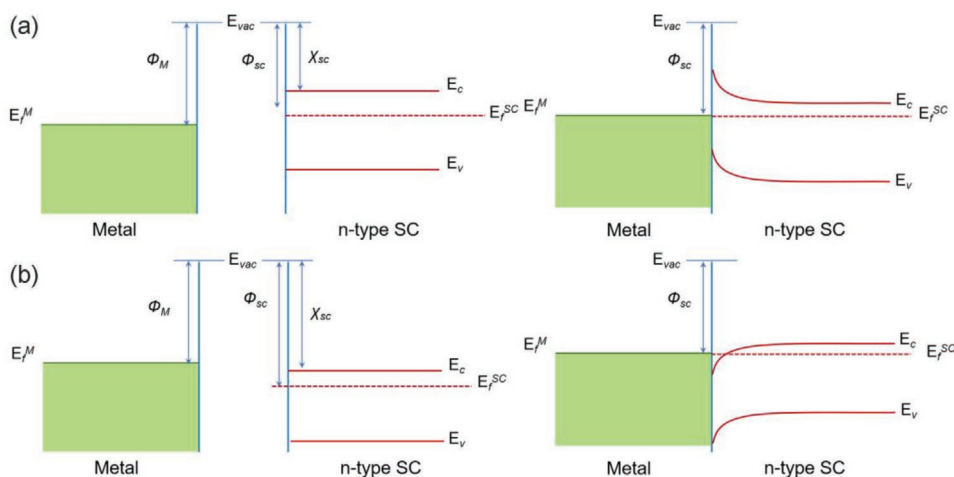


Figure 2. The band diagram of an n-type semiconductor and a metal with a) high and b) low work function before contact (left) and after contact (right).

bands of the semiconductor tend to bend upward to decrease the boundary charge density. In this case, an interface potential barrier is generated and the electronic band bending will occur at the side of the semiconductor closer to the dispersion/matrix interface, which preferentially scatters the low energy carriers. Due to the charge carrier relaxation time (which depends on the electron energy), the carrier energy filtering effect will occur, allowing for the values of σ and S to be further modified.^[62]

On the other hand, when a metal with a low work function is combined with an n-type semiconductor (Figure 2b), an ohmic contact is established and the boundary is positively charged due to the electron flow from the metal to the semiconductor, in conjunction with the screening-length difference on both sides. Thus, the semiconductor band tends to bend downward and enhance the accumulation of electrons, to compensate for the positive charges on the boundary. It is even possible for the bended conduction band to cross the Fermi level, leading to the degeneration of the semiconductor surface, which possesses higher electrical conductivity compared with the bulk. In contrast, no potential barrier exists for the ohmic contact, allowing all carriers to freely pass through the interface; however, they can still serve as a scattering center, due to the potential energy variations at the interface.

The dimensionality of the second phase also plays a critical role in the manipulation of the carrier and phonon scattering, as well as attaining a factorial improvement in the zT values. In the following sections, the inclusion of different material types (i.e., metals, oxides, semiconductors, carbonic materials, and MXenes) in TE matrices, as well as the effects of their dimensions, are discussed. The aim of this section is to provide insight into the challenges and opportunities for maximizing the potential utilization through the thorough analysis of an ample and diverse reference source.

2.1. Metallic Dispersions

Through electronic structure modifications, metal nano-inclusions can increase the zT of TE materials. This is accomplished by incorporating metal nano-inclusions into the semiconducting TE matrix, resulting in improved thermal (reduced κ) and electronic (enhanced PF) transport properties. Furthermore, the instinct magnetic moments of metals have an impact on the matrix carrier transport, which can also improve TE efficiency. In this chapter, we divide metals into two groups based on their magnetic states, namely those with and without magnetic moments, and demonstrate how they affect the performance of TE matrices.

2.1.1. Metallic Dispersions without Magnetic Moments

After the junction of the metal and the TE matrix is formed, the metal will transfer electrons to the TE matrix depending on its work function. Different metals have dissimilar work functions, as they depend on their unique crystal orientations and surface impurities.^[55] If the work function of dispersion differs substantially from the work function (or electron affinity) of the matrix, the charge carriers could be easily trapped easily in

potential wells.^[64] The action of the metal work function can be further understood by dispersing different metals in Bi_2Te_3 . Considering the work function of ≈ 5.4 eV for Au, the ϕ_B of ≈ 0.1 eV can be obtained. Therefore, the occurrence of carrier scattering is expected by introducing the energy well.^[65] In addition, there is an optimal work function range value for each semiconductor matrix which results in the highest TE performance. For instance, Pt has a work function of ≈ 5.65 eV, forming a potential barrier of $E_b \approx 0.2$ eV for the Pt– Bi_2Te_3 interface, which is significantly larger than the one formed in the Au– Bi_2Te_3 system. According to the theoretical calculations for the enhancement of PF, the optimal potential barrier is approximately 0.1 eV,^[66] suggesting that Au is a better candidate than Pt. In the case of a metal with a smaller work function than that of Bi_2Te_3 (e.g., Cu and Bi), the formation of a potential barrier is conditional. Incorporating Cu into the Bi_2Te_3 matrix might not necessarily generate energy filtering, which is attributed to the absence of E_b , stemming from the lower work function of Cu (4.5–5.1 eV) than that of Bi_2Te_3 .^[65] When Bi is embedded in Bi_2Te_3 , due to the lower work function of Bi (≈ 0.425 eV) than Bi_2Te_3 , the obtained E_b value of ≈ 0.2 eV can effectively improve the S value, as reported by Chu et al.^[67] Thus, a suitable metal dispersion level should be opted for according to the work functions of both the matrix and the metal. **Table 1** presents the main parameters of metals which should be considered for the effective charge carrier energy filtering in metal-semiconductor systems. These experimental results indicate that the inclusion of metals is a promising strategy for achieving interface/surface modifications in various TE materials.

The simultaneous improvement of the electrical conductivity and the notable reduction of the lattice thermal conductivity were reported by dispersing Ag nanoparticles with a diameter

Table 1. Main parameters for the effective energy filtering of charge carriers in metal-semiconductor systems.^[56,68]

Metal	Effective electron density	Work function [eV]	Atomic chemical potential [V]
Sb	5	4.55	13.13
Sn	4	4.3	11.58
Al	3	4.28	10.24
Fe	2.69	4.5	9.84
Co	3.03	4.92	1.64
Ni	3.37	5.15	11.39
Ti	3.34	3.96	9.61
V	3.69	4.3	9.61
Cr	4.03	4.5	10.12
Mn	2.34	4.1	9.06
Zr	4	4.05	8.74
Nb	4.69	4.3	9.62
Mo	5.03	4.6	10.54
Ag	1.39	4.26	8.32
Au	2	5.1	10.10
Cu	1.58	4.65	9.18
Bi	5	4.22	12.64
Te	6	4.95	14.82

of 60 nm in a Bi_2Te_3 system, by employing a fabrication procedure combining a hydrothermal method with magnetic stirring.^[69] The interfaces of the dispersed Ag nanoparticles at the Bi_2Te_3 grain boundaries could be clearly observed, realizing a unique combination of phonon scattering and carrier concentration enhancement, resulting in the remarkable improvement of zT to 0.77 at 475 K. The PF of a Bi_2Te_3 system modified with 1.5 vol% Ag nanoparticles was augmented by more than two times, namely from 0.49 to $1.14 \text{ mW m}^{-1} \text{ K}^{-2}$. Similarly, such significantly improved electrical properties were observed in a FeSb_2 -Cu NPs system.^[70] The remarkable obtained enhancement of approximately 90% (over pure FeSb_2) was comparable with the results achieved by other approaches, such as band engineering^[71,72] and modulation doping.^[73,74] This phenomenon can be theoretically attributed to the band alignment between FeSb_2 and Cu, along with the microstructure of the FeSb_2 -Cu nanocomposite. Despite the existence of an energy barrier in the range of 0.15–0.2 eV at their interfaces, the closed work function (the work function of FeSb_2 for the (001) plane and Cu are 4.723 and 4.7 eV, respectively) may have positive influence on the electron transfer performance. Additionally, the dispersion of Cu nanoparticles could also provide charge carriers from its conduction band to FeSb_2 . Although the increase of the carrier concentration in the FeSb_2 matrix can be reasonably expected, there are no detailed results concerning Hall mobility and carrier concentration for the FeSb_2 -Cu system. In order to investigate the effect

of metal nanoparticle inclusion on the electrical properties of TE matrices, various typical systems have been summarized in **Figure 3**. With the exception of Hall mobility, almost all systems exhibited an increase in carrier concentration after adding and increasing the content of metal nanoparticles, resulting in an enhanced electrical conductivity. For example, the electrical conductivity of the $\text{Bi}_{0.5}\text{Sb}_{1.5}\text{Te}_3$ system^[75] increased by 6 times after 0.2 wt% Cu dispersion. The S only decreased by approximately two times, which was assigned to the increased carrier concentration.

Besides the chemical composition of the dispersion, the size of the metal nanoparticles also has a significant influence on the TE properties. When the size of the second-phase particles is below 10 nm, they can be categorized as quantum dots (QDs) with zero dimensionality. QDs have emerged in lots of contemporary applications, such as biosensing probes,^[78–80] solar cells,^[81–83] and light-emitting diodes.^[84–86] QDs, which have a typical diameter of 2–10 nm,^[87] can significantly contribute to the energy filtering performance of TE materials, as reported by a series of theoretical studies.^[62,63,66,88,89] In the work of Zhou and Yang,^[90] QDs with diameter (a) and interdot distance (D) were periodically embedded in the matrix, as shown in **Figure 4a**. Here, we define V_{CP} as the height of the confinement potential, and V_{bo} as the band offset between the second phase in the QDs and the host materials. Due to the overlap of the electron wave function tails that extend from the QDs into the matrix, the carriers will not be confined by the interface

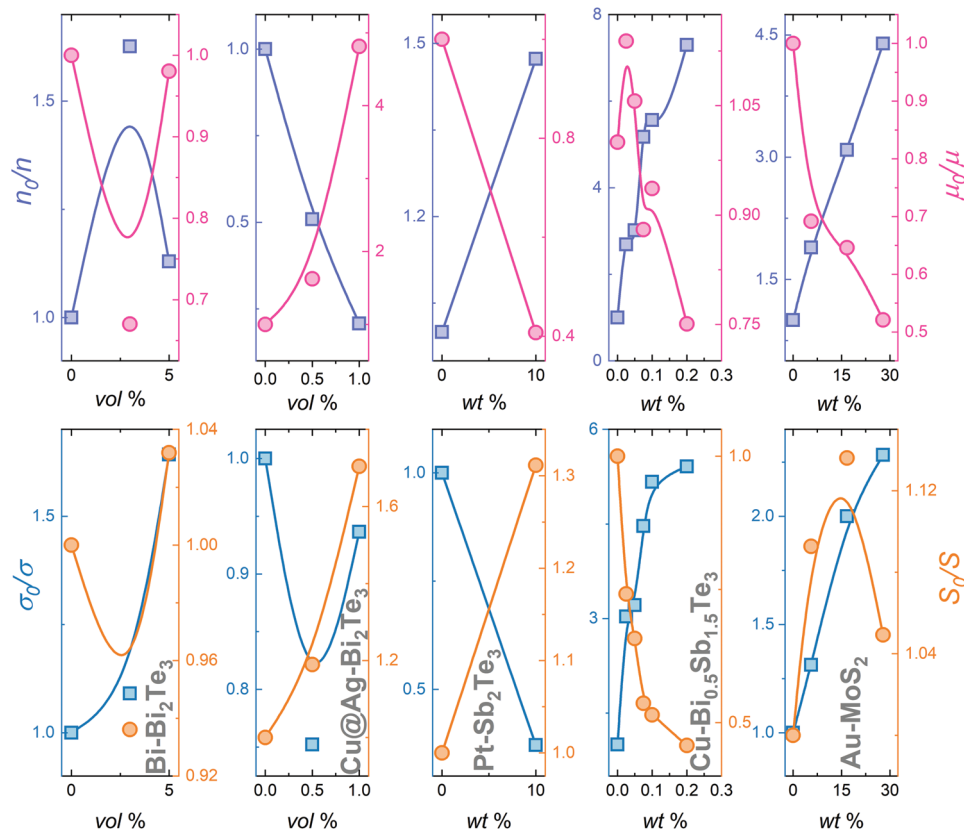


Figure 3. Dispersion content dependence of n/n_0 , μ/μ_0 , σ/σ_0 , and S/S_0 at 300 K (Subscripts with zero stand for pristine materials).^[56,67,75–77]

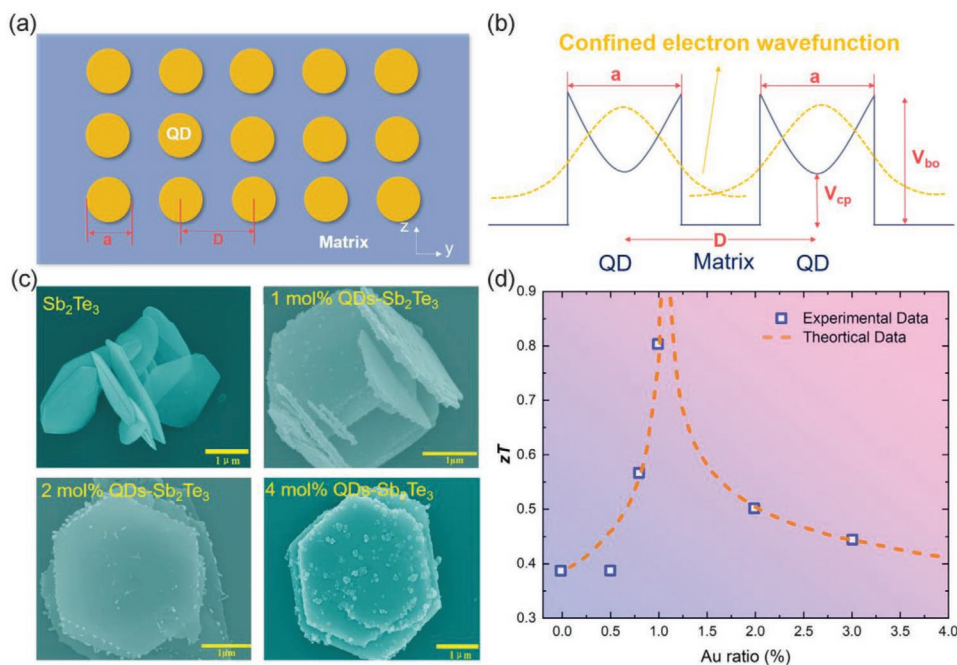


Figure 4. a) Illustration of the QDs structure in the matrix; b) Schematic diagram of the quantum confinement of the electron wave functions; c) Scanning electron microscopy (SEM) image of pure Sb_2Te_3 and Au QDs- Sb_2Te_3 composites with an Au mole ratio of 1, 2, 4 mol; d) Comparison of experimental and theoretical zT value of an Au QDs- Sb_2Te_3 system using the percolation theory at 300 K.^[91] Reproduced with permission.^[91] Copyright 2019, American Chemical Society.

and travel through the QDs by hopping across the periodical arrays of quantum-confined electrons. Figure 4b demonstrates the effect of energy filtering between the QDs and the matrix, where high bulk-like energy carriers can easily move across the confinement potential, whereas the movement of the low-energy carriers is restricted. This energy filtering effect can lead to an enhancement in S but a decrease in σ . Figure 4c illustrates that the application of a solution with low Au concentration (1 mol%) can result in the uniform distribution of Au QDs (with a mean size of ≈ 10 nm) on the edges and surfaces of Sb_2Te_3 nanoplates. Increasing the Au concentration (4 mol%) will cause an increase in the size of the distributed particles (≈ 40 nm) and, in turn, an agglomeration of Au QDs.^[91] By applying the classical percolation power law, while controlling the content/size/distribution of QDs, the zT value can reach a maximum of 0.8 if a 1.08 mol% Au solution is used (Figure 4d).

Besides the positive effect of metals on the TE performance of the matrix, the thermal instability and rapid agglomeration of metal nanoparticles should also be considered during the material selection process. In the Au- Bi_2Te_3 system, Au nanoparticles with a mean size below ≈ 10 nm can melt and diffuse into the Bi_2Te_3 matrix if the nanoparticle content increases. The formation of $\text{Au}_{\text{Bi}}^{2-}$ defects can alter the carrier concentration, resulting in the suppression of the energy filtering effect. Figure 5 illustrates the combined effects of Ag doping and Ag/Pt QDs embedding on the T -dependent carrier concentration (p) of MnSi_2 .^[92] Interestingly, the p of the sample with 1 at% Ag QDs was almost comparable with that of $\text{Mn}_{0.99}\text{Ag}_{0.01}\text{Si}_{1.8}$, whereas the carrier concentration of the sample with 1 at% Pt QDs was much lower than that of $\text{Mn}_{0.99}\text{Si}_{1.8}$ (MS). The subtle difference between Ag-doping and dispersing Ag QDs

indicates that Ag QDs may diffuse into the matrix, weakening the thermal stability of the Ag QDs compared to their Pt equivalents. In addition, by comparing the MS-1 at% Ag QDs and MS-1 at% Ag/Pt QDs (Ag to Pt molar ratio 2:1), it can be observed that p decreases with the appearance of Pt QDs appeared in the $\text{Mn}_{0.99}\text{Si}_{1.8}$ matrix, further confirming that some Ag QDs from the Ag/Pt QDs diffused into matrix, as opposed to the dispersion of pure Pt QDs (Figure 5a). All these phenomena are illustrated in the schematic diagram shown in Figure 5. In the p-type MS, the dominant carriers in the Pt QDs are electrons which are restricted within the nano-inclusion/matrix interface. When the temperature increases, the localized electrons will escape from the Pt QDs and inject into the MS matrix. Therefore, the free electrons and holes are neutralized, causing the p to decrease. However, Ag QDs occupy the Mn vacancies as impurity acceptors and generate hole carriers, which is commensurate with the direct doping of Ag in MS. This demonstrates that an adequate amount of QDs can diffuse into the defect positions in the parent material.

2.1.2. Metallic Dispersions with Magnetic Moments

Apart from non-magnetic and noble metals (such as Pt,^[56] Ag,^[93] and Au^[77]), the introduction of magnetic metallic nanoparticles (Co/Ni/Fe) with different magnetic states than that of the TE matrix can significantly improve its thermoelectric performance.^[94] It should be noted that the process of magnetic second-phase dispersion in TE matrices must be separated from the one of doping effect, since due to the extremely low solubility of most magnetic ions in TE materials, the improvement

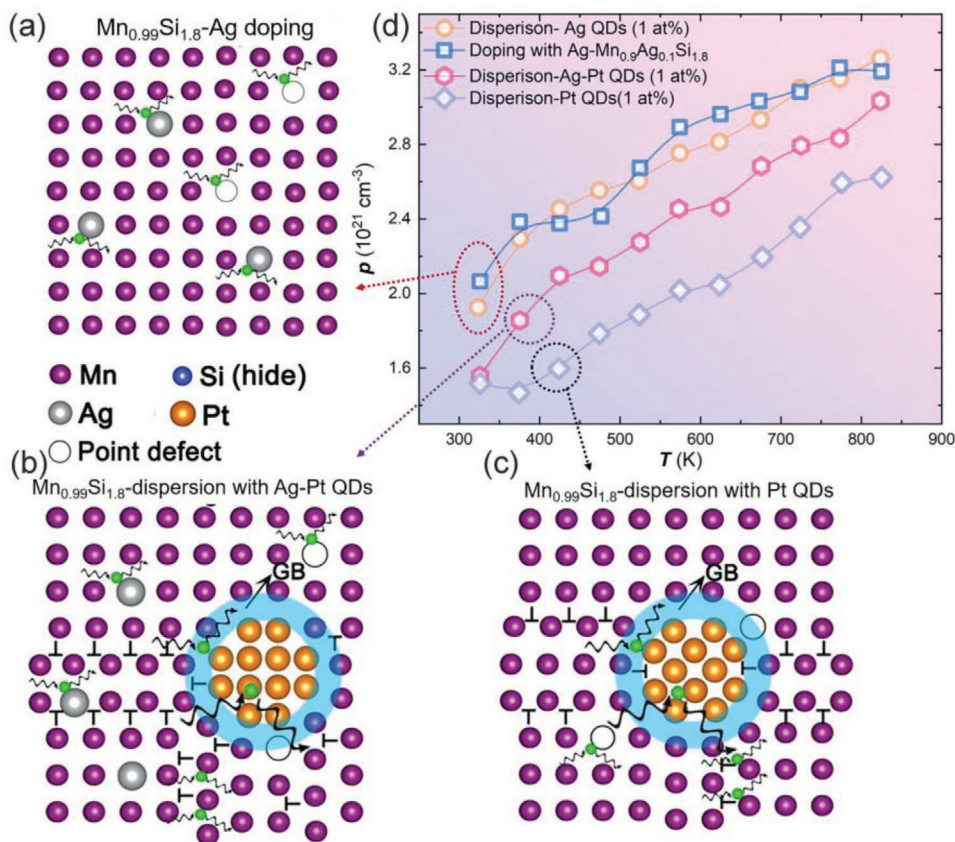


Figure 5. a) The carrier variation mechanism derived from the Ag-doping effect in conjunction with the embedding of Ag/Pt and Pt QDs; b) Hall carrier concentrations of MnSi₂ containing Ag, Ag/Pt, and Pt QDs and Mn_{0.9}Ag_{0.1}Si_{1.8} as a function of temperature.^[92] Reproduced with permission.^[92] Copyright 2021, Elsevier.

in terms of thermoelectric performance after doping is insignificant. However, many studies which focused on doping magnetic ions into non-magnetic TE materials have demonstrated that the thermoelectric properties can be improved by the magnetic-drag effect and spin entropy in a variety of systems, such as Li-MnTe,^[95] Fe/Co-doped Bi_{0.48}Sb_{1.52}Te₃,^[96] Ni-doped BiCuSeO,^[97] and Ni/Co-doped Cu₂ZnSnS₄.^[97] When the doping content exceeds the solid solubility, pure metal particles may precipitate on the grain boundary, making the distribution and content of magnetic metals on the interfaces difficult to control. Thus, by introducing magnetic nanoparticles or nanoclusters into a non-magnetic TE matrix, the interaction between the magnetic moment and the charge carriers can optimize the thermoelectric properties.

Notably, the charge carrier concentration can be altered by introducing magnetic particles, similarly with non-magnetic metal particles. By exploiting the phenomenon of magnetic phase transition, the electrical properties deterioration, which derives from the interfacial scattering, can be suppressed within a desired certain temperature range due to magnetic phase transition of magnetic metals. Du et al. investigated the dispersion of Ni nanoparticles into a Bi₂Te_{2.7}Se_{0.3} matrix and discovered that the carrier concentrations were significantly improved after the dispersion.^[98] In the magnetization versus magnetic field ($M-H$) curves, the Ni nanoparticles exhibited a very low

coercivity at 350 K, confirming their superparamagnetic states and ferromagnetic properties. When in the paramagnetic phase, the nanoparticles can release their electrons through intrinsic excitations and thereby increase the carrier concentration. By exploiting the interactions between the embedded magnetic nano-inclusions and itinerant carriers, Lu et al.^[99] achieved significant enhancements in terms of both carrier mobility and the Seebeck coefficient in a p-type Ti_{0.25}Zr_{0.25}Hf_{0.5}NiSn_{0.975}Sb_{0.025} TE system. Improved carrier concentrations were also displayed in the Ni-Yb_{0.2}Co₄Sb₁₂^[100] and Fe/Co-MnSi_{1.787}Al_{0.01}^[101] systems. Obviously, magnetic metals can provide a good platform for utilizing such magnetic phenomena and optimize the thermoelectric performance of materials.

It should be noted that some unique magnetic phenomena can only manifest when the size of the particles is reduced to a certain value.^[102] A ferromagnetic nanoparticle can be magnetized into a paramagnet under an external magnetic field if its size is small enough to contain one magnetic domain,^[103] a phenomenon dubbed as “super-paramagnetism.” Under such size-dependent magnetic phenomena, super-paramagnetism can be achieved in Co/Ni/Fe nanoparticles embedded in Bi_{0.3}In_{0.3}Co₄Sb₁₂. The scanning electron microscopy (SEM) image of Co nanoparticles with a diameter of 5–10 nm decorating the surface of Bi_{0.3}In_{0.3}Co₄Sb₁₂ grains^[94] is shown in **Figure 6a**. The ohmic contact is established after the dispersion

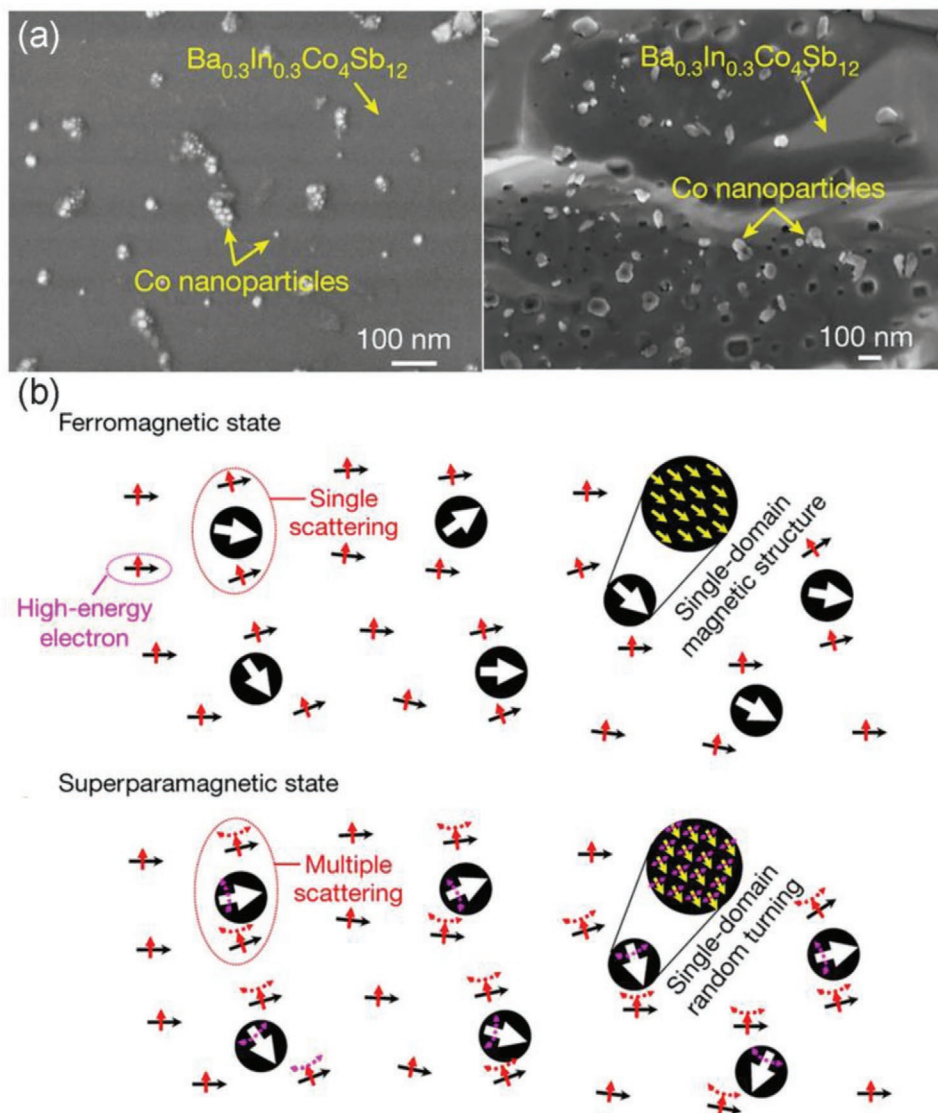


Figure 6. a) Field emission scanning electron microscopy (FESEM) images of as-prepared powders (left panel) and bulk material (right panel); b) Single scattering of electrons via s–d spin coupling and multiple scattering of electrons caused by the turning of the magnetic domains within the superparamagnetic Co nanoparticles.^[94] Reproduced with permission.^[94] Copyright 2017, Springer Nature.

of the metals, where magnetic Co species provide extra free electrons under a paramagnetic temperature state, resulting in the reduction of the electrical conductivity degradation rate. More specifically, the transition of the nanoparticles from ferromagnetism to super-paramagnetism induces magnetic fluctuations, causing the multiple scattering of electrons (Figure 6b). High zT values of 1.5–1.8 were obtained by further suppressing thermal conductivity,^[94] confirming that the dispersion of magnetic metals is an excellent technique for improving the thermoelectric performance of certain TE materials. It should be noted, however, that certain metal nanoparticles may react with the matrix or generate additional charge carriers, resulting in the increase of the electrical thermal conductivity due to electrical contribution, a phenomenon which has been observed in several systems.^[67,75,93,104]

2.2. Oxide Dispersion

Oxide compounds are typically characterized by low thermal conductivity and reasonably good chemical and thermal stability, indicating that they seldomly react with other compounds or can even decompose under high temperatures and certain atmospheres.^[105] Thus, oxide nanoparticles attract significant attention for application in TE materials. The ultralow thermal conductivity of $0.6 \text{ W m}^{-1} \text{ K}^{-1}$ was achieved by dispersing Al_2O_3 nanopowder into the W matrix,^[106] providing with an effective approach for suppressing the lattice thermal conductivity of the system through the establishment of a high-density interface between dissimilar constituents.

To get insight into the influence of nanoparticle size on thermal conductivity, a theoretical model was applied

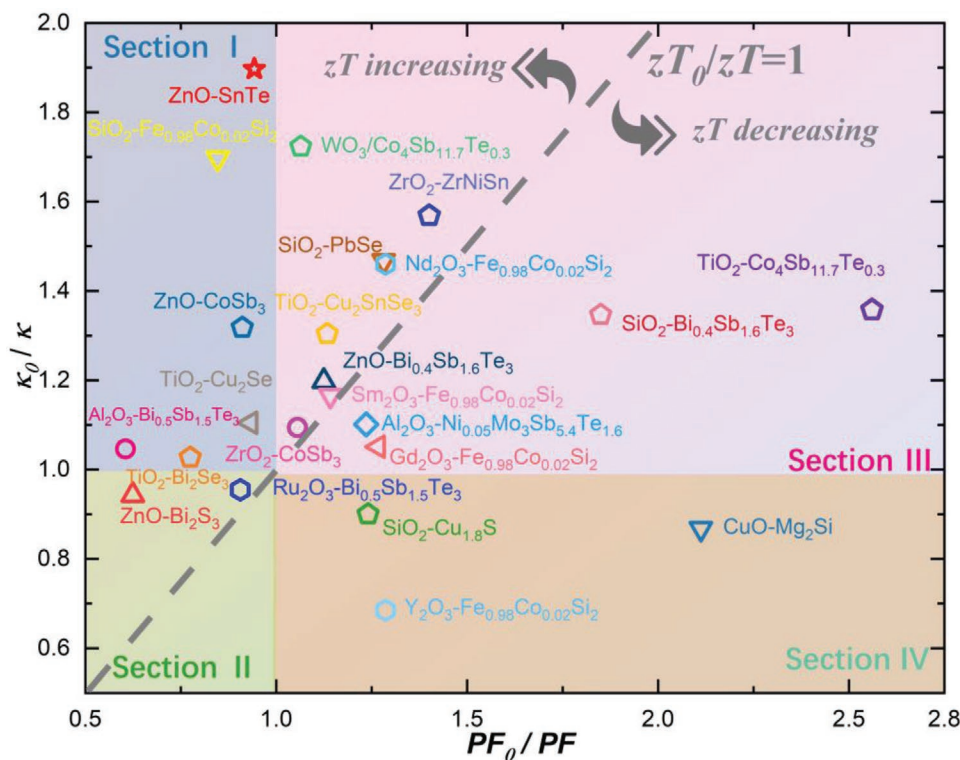


Figure 7. PF_0/PF versus κ_0/κ for some representative systems at their maximum zT values (Subscripts with zero stand for pristine materials).^[105,107–121]

onto the ZnO-CoSb₃ system (ZnO dispersed into CoSb₃ matrix).^[122] Assuming a homogeneous dispersion of ZnO particles, the dielectric peak value of the κ_1 decreased from 50 to 18 W m⁻¹ K⁻¹; furthermore, a 25% reduction in κ_1 was observed after the uniform dispersion of ZnO particles with an average size of 12 nm at 300 K. The same experimental results also proved that the incorporation of oxide nanoparticles resulted in a strong phonon scattering, which contributed to the suppression of thermal conductivity. Various oxide particles were introduced as second phases into traditional thermoelectric materials, as summarized in **Figure 7**. Since the second phase can considerably influence the thermal and/or electrical properties of the material, the PF_0/PF versus κ_0/κ graph was plotted and divided into three sections (PF_0 , PF , κ_0 , and κ are the power factors and total thermal conductivities of the parent and modified materials at maximum zT , respectively). The majority of the results are presented in section III, where it can be seen that the κ_0/κ and PF_0/PF ratios both exceeded 1 for the cases of WO_3 - $Co_4Sb_{11.7}Te_{0.3}$,^[109] SiO_2 - $PbSe$,^[108] and Al_2O_3 - $Ni_{0.05}Mo_3Sb_{5.4}Te_{1.6}$.^[118] These results verified the great decreasing of the thermal conductivities, as well as the deterioration of the electrical properties of the abovementioned materials. The systems included in section I demonstrated improvements in both their thermal and electrical properties: for example, the incorporation of ZnO nanoparticles in the SnTe matrix with the κ_0/κ and PF_0/PF ratios of 1.85 and 0.94, respectively, yielded remarkable results.^[119] Apart from the clearly discernible homogenous distribution of ZnO particles in the SnTe matrix, the phase boundaries between ZnO and SnTe (**Figure 8a**) exhibited large mismatch, thereby accumulating lattice defects,

such as dislocations and vacancies, which further contributed to phonon scattering.

In addition, the decorated and mismatched interfaces may also alter the electronic structure of the boundaries between the nanoinclusions and the matrix. As shown in the right panel of **Figure 8b**, the phase boundaries generated a potential well capable of trapping charge carriers. As recently reported,^[123] the SnTe with typical Dirac band structure can effectively scatter the long-mean-free-path electrons in electron-phonon scattering process when the size of grains is below 10 nm. These subtle features are conducive to the enhancement of S , it is possible to maintain the electrical properties even under large interface density conditions in SnTe-based materials. On a related note, metastable Y_2O_3/ZrO_2 particles embedded in BiSbTe alloy (Bi_2Te_3 +75% Sb_2Te_3) also impacted the overall electronic structure, even though the Seebeck coefficient of both significantly deviated from the Pisarenko plot (**Figure 9**).^[124,125] With the dispersion of 2–6 wt% Y_2O_3 into the matrix of the BiSbTe alloy, although there was relatively negligible change in the charge carrier concentration, the S increased by 1.5 times. However, in ZrO_2 -BiSbTe, there was a little yet noticeable change in S with increasing the ZrO_2 content, implying the alteration of the band structure with the incorporation of nanoinclusions. In addition to the aforementioned oxides, the introduction of magnetic oxides to TE matrices can alter the carrier concentration under a specific temperature range. $BaFe_{12}O_{19}$ nanoparticles with sizes ranging from 20 to 150 nm were distributed in a $Ba_{0.3}In_{0.3}Co_4Sb_{12}$ matrix as permanent magnets.^[126] To prevent the performance degradation of the TE material in its intrinsic excitation region, the Curie temperature (T_C) of the added

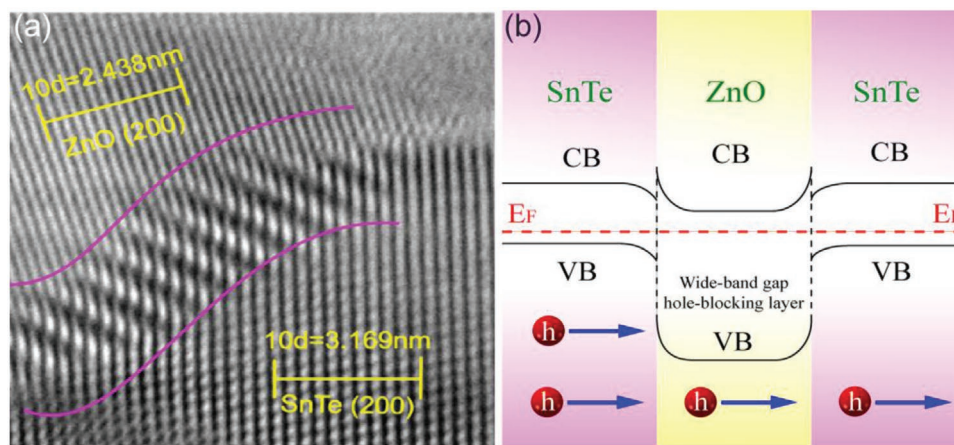


Figure 8. a) High resolution transmission electron microscopy (HRTEM) images of the ZnO–SnTe interface; b) Schematic diagram of the carrier energy barrier in the ZnO–SnTe interface.^[119] Reproduced with permission.^[119] Copyright 2017, The American Ceramic Society.

nanoparticles should be adjusted close to the intrinsic excitation temperature of the matrix material by adjusting the nanoparticle size.^[126] The strong interactions between the local magnetic moments and the carriers below T_c enable the $\text{BaFe}_{12}\text{O}_{19}$ nanoparticles with ferromagnetic states to trap electrons. Above the T_c , the nanoparticles with a paramagnetic state will release the trapped electrons, consequently increasing the carrier concentration in the matrix's intrinsic excitation region. In view of the above, the addition of magnetic oxides was verified to significantly increase the carrier concentration in the intrinsic excitation region, while also regulating the thermal conductivity, which conjointly result in an improved TE performance.

Since the stability of the oxide phases can be affected by their particle size and synthetic process, the unwanted reactions

between certain oxides and TE matrices, for example, the decomposing or reaction of the oxide with the matrix during the high-temperature pressing process, should be addressed and discussed. For instance, ZnO dispersed into a Bi_2S_3 ^[112] matrix was reported to react with sulfur elements and produce ZnS phases during the spark plasma sintering process (the system is located in section II of Figure 7). During the hot pressing of the TiO_2 - Bi_2Se_3 system,^[116] the dispersed TiO_2 was observed to transition into an anoxic non-stoichiometric TiO_{2-x} state under vacuum conditions, hence generating electrons which may influence the carrier concentration of the matrix. In the case of ZrO_2 addition into $\text{Fe}_{0.98}\text{Co}_{0.02}\text{Si}_2$,^[113] the decomposition of ZrO_2 was accompanied with the formation of ZrSi phases.

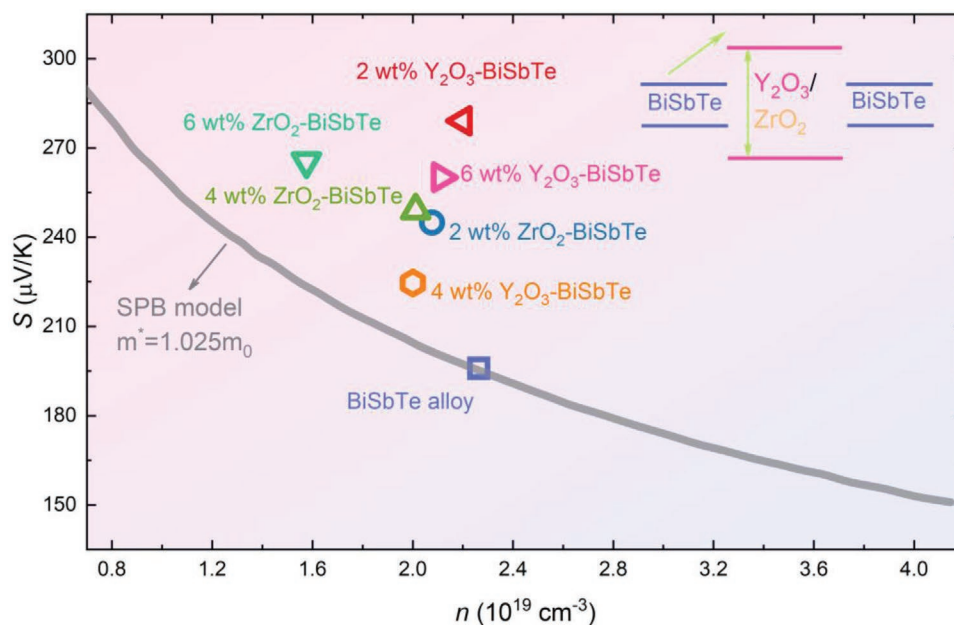


Figure 9. Seebeck coefficient versus carrier concentration of $\text{ZrO}_2/\text{Y}_2\text{O}_3$ - BiSbTe alloy at 300 K.^[124,125] The inset is illustrating the band alignment between the BiSbTe alloy and the $\text{Y}_2\text{O}_3/\text{ZrO}_2$ dispersions.

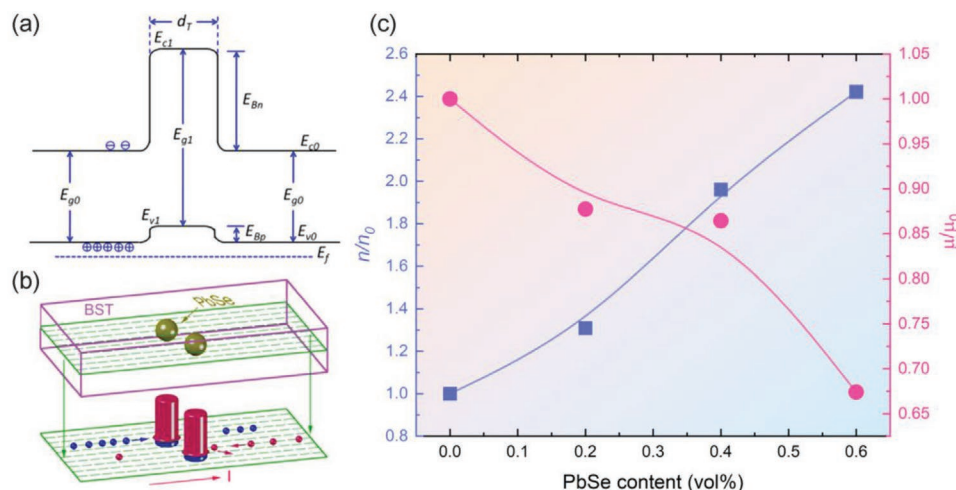


Figure 10. a) Schematic illustration of the energy bands of PbSe and $\text{Bi}_{0.48}\text{Sb}_{1.52}\text{Te}_3$ with an interfacial potential well for hole carriers; b) Schematic drawing of the formed spatial potential barrier (red cylinder) for electrons and potential well (blue (short) cylinder) for holes due to the incorporation of the PbSe; c) Dispersion content dependence of n/n_0 and μ/μ_0 at 300 K (Subscripts with zero stand for pristine materials).^[127] Reproduced with permission.^[127] Copyright 2020, American Chemical Society.

2.3. Semiconductor Dispersion

Oxide compounds and metals may lead to the degradation of the electrical properties and increase the electrical thermal conductivity of a TE material, respectively. In this aspect, semiconductors may play a moderate and compensatory role in improving the thermoelectric performance. The moderate band structure difference between the semiconductor (as the second phase) and the TE matrix will benefit the formation of potential energy wells and enhance the energy filtering effect, which may facilitate the manipulation of the electrical transports.

Besides the common method of directly ball-milling the dispersion materials and the matrix, synthesizing and mixing two semiconductor compounds in the inorganic or/and organic solution could be beneficial for obtaining fine and homogenous dispersions. Jiang et al.^[127] prepared Bi_2Te_3 and PbSe nanoflakes using a bottom-up synthesis method. The occurrence of band bending at the created interfaces in the Schottky junction, which allowed for carrier scattering, resulted in a 30% improvement of the zT . However, the interrelation between the potential barrier height and the carrier scattering intensity should be engineered. By embedding PbSe compounds into a $\text{Bi}_{0.4}\text{Sb}_{1.6}\text{Te}_3$ system, the S was notably enhanced, while inducing an insignificant bipolar effect. Considering the band gaps of $\text{Bi}_{0.4}\text{Sb}_{1.6}\text{Te}_3$ and PbSe, the potential barrier (E_{Bp}) of the holes was only 0.15–0.21 eV, whereas that for the electrons was –37 to –32 meV (Figure 10a). Stemming from the strong electron scattering induced by the large barrier, compared to the weak hole scattering by the small barrier (Figure 10b), the hole carrier concentration increased and the Hall mobility decreased, thereby benefitting the suppression of both the minority carrier transport and the bipolar effect (Figure 10c). In another study, Shi et al. dispersed Sb_2Te_3 into a $\text{Bi}_{0.48}\text{Sb}_{1.52}\text{Te}_3$ matrix.^[128] The phase boundaries between the nanoinclusions and the matrix created an effective barrier which improved the PF and increased the effective mass m^* . The interface potential bar-

riers can obstruct low-energy carriers, potentially suppressing the bipolar effect and leading to an obvious increase in carrier mobility, along with a slight decrease in carrier concentration.

Due to the different n- and p-type nature of semiconductor materials, PN junctions at the interfaces can be formed when different matrix types are dispersed in a semiconductor material. According to the schematic^[129] of a PN junction illustrated in Figure 11a and 11b, two kinds of majority carriers exist in different n- and p-type materials, and the built-in electric field will be established after voltage is applied. The band alignment in the interface will yield an ultrahigh interface potential, allowing the carrier transport to occur only along the homogeneous junctions. In principle, the reduced n in composites with PN junctions is mainly attributed to the combination of holes and electrons during the formation of the carrier-depletion layers.^[129] The decreased μ originates from the forbidden transport of electrons and holes by the built-in electric field. This decrease in carrier concentration and Hall mobility will improve the electrical properties as a result. The powders of Bi_2Te_3 and Sb_2Te_3 were separately synthesized and mixed according to the stoichiometry of $(\text{Bi}_2\text{Te}_3)_x(\text{Sb}_2\text{Te}_3)_{1-x}$.^[129] The energy-dispersive X-ray spectroscopy (EDS) line-scanning analysis of the Sb/Bi elemental distribution at the grain boundaries revealed that both constituents remained chemically intact and no solid solution was formed during the sintering process. Furthermore, compared with the Sb_2Te_3 pristine powder, the carrier concentration and Hall mobility significantly decreased (Figure 11c). As a consequence, the electrical conductivity was reduced from 2209.5 to 824.1 S cm^{-1} and the Seebeck coefficient escalated from 100.6 to 177.8 $\mu\text{V K}^{-1}$ as the x varied from 0 to 0.15, while PF exhibited a slight increase. The 50%-reduced thermal conductivity induced a 129% increase in zT , which presented an average value of 0.89 over the temperature range of 300–550 K. Similarly, the PN junction interfaces between the Pb/I co-doped SnSe ($\text{Sn}_{0.97}\text{Pb}_{0.03}\text{Se}_{0.89}\text{I}_{0.06}$) and WSe_2 ^[130] compounds created an effective boundary which decreased the

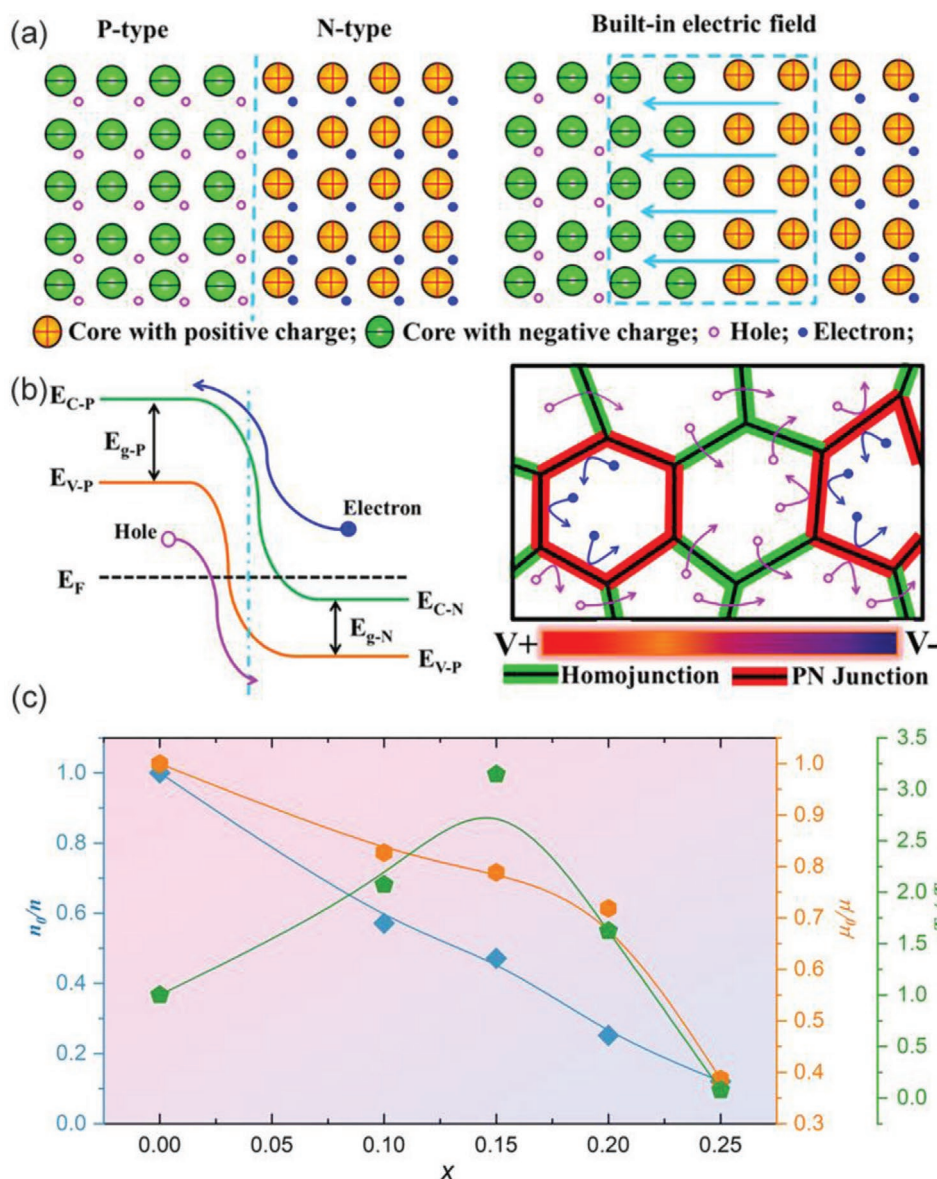


Figure 11. a) Distribution of carriers prior to the PN junction formation; b) Band alignment at the p-type Sb_2Te_3 and n-type Bi_2Te_3 interface; c) Dispersion-content dependence of n/n_0 , μ/μ_0 , and zT_0/zT at 308 K (Subscripts with zero stand for pristine materials).^[129] Reproduced with permission.^[129] Copyright 2018, American Chemical Society.

carrier concentration from 22×10^{18} to $2 \times 10^{18} \text{ cm}^{-3}$ when 1 wt% WSe_2 was dispersed. The increased effective mass was in agreement with the strong blocking effect, since the relatively low energy carriers were considerably obstructed. The final zT value can be optimized from 0.9 to 1.35 after WSe_2 dispersion, indicating that forming the appropriate PN junction interface constitutes another crucial method for attaining high TE performance.

Parallel to the fundamental requirement for a high zT , feasible thermoelectric applications demand TE materials with high thermal stability and mechanical strength, conjointly known as good service stability. The majority of TE materials with promising zT values usually lack in terms of thermal stability, while also exhibiting phase transitions and abruptly changing coefficients of thermal expansion (CTE), thus

limiting their integration into practical applications. To overcome the abovementioned obstacles, the incorporation of appropriate micro/nano second phases into the TE matrix has been verified to improve the thermoelectric performance and service stability of TE materials; however, discovering new composite materials optimized for synergetic thermal and electrical applications while also exhibiting high service stability, remains a generally challenging task. Among the several types of second phases that have been incorporated into TE materials to enhance their zT value, silicon carbide nanoparticles have attracted significant interest. Many semiconductors, such as SiC ,^[131–142] MgB_2 ,^[143,144] TiN ,^[145,146] B ,^[147–149] and others,^[150–152] have been confirmed to improve both the mechanical and thermoelectric performance of TE materials.

SiC is a wide-bandgap semiconductor with high thermal stability, elastic modulus, and hardness characteristics, rendering it favorable candidate for improving both the mechanical and thermoelectric performance of TE materials. It has been used as a second phase in a wide variety of TE materials, such as SnSe,^[153] ZnSb,^[154] Cu₂Se,^[138,155] SiGe,^[141] PbTe,^[156] Mg₂Si,^[134] etc. Along with the well-documented effects of SiC on the thermoelectric performance of TE materials,^[131,141] its influence on their mechanical stability has also been investigated. In the work of Liu et al.,^[137] the incorporation of 1 wt% SiC particles in Bi_{0.5}Sb_{1.5}Te₃ samples effectively increased their Vickers hardness (H_v), Young's modulus (E), fracture toughness (K_{IC}), and bending strength, compared with their SiC-free equivalents. The same behavior was also observed by Zhou et al., where the addition of 0.2–1 vol% of SiC nanoparticles to a Yb_{0.3}Co₄Sb₁₂ skutterudite matrix considerably increased its hardness and fracture toughness.^[140] According to the Hall–Petch equation, the presence of harder second phases has been well known to reduce the grain size of the matrix and increase the hardness of the composite.^[157,158] Also, nanoparticle dispersion aids in the dislocation of pile-up stresses and hinders the generation of cracks, as well as their further propagation, thereby strengthening the fracture toughness.^[132,134,136,159] The presence of second phases can trigger the generation of porosities, however, impacting in the process the relative density and, by extension, material hardness.^[154]

The incorporation of other second phases, such as MgB₂, nano boron, TiN, etc., can improve the mechanical properties of the TE matrix via similar mechanisms as those discussed for SiC inclusion.^[146,149,155] Wang et al. theorize that the improved mechanical properties of Ge_{0.9}Sb_{0.1}Te by MgB₂ addition may be attributed to the synergetic action of Mg dopants and segregated B elements. The Mg dopants contribute to the solid-solution strengthening effect, while the segregated B atoms contribute to the grain-boundary strengthening effect. Parallely, subtle changes in the CTE near the phase transition temperature of GeTe (680 K) have been observed for MgB₂-doped Ge_{0.9}Sb_{0.1}Te samples, a phenomenon which can be attributed to the simultaneous action of Sb and Mg alloys on tuning the chemical bonding and lattice structures, as well as the local distortions generated around the Mg sites.^[144]

From the thermoelectric performance aspect, the above-mentioned nanoparticles are primarily characterized by large S values, stemming from their wide band gaps. Even the homogeneous distribution of extremely low volume fractions of these compounds and the formation of a coherent interface with the matrix, can aggravate the collisions of the charge carriers with the nanoparticles. The particles located in planes perpendicular to the temperature gradient can filter out many low-energy carriers, while allowing the high-energy carriers to pass through the nanoparticles eventually enhancing the material's Seebeck coefficient.^[131,138] As another possible mechanism for increasing the Seebeck coefficient, enhancing the density of states in the composites has been proposed. J. Li et al.^[131] reported that the addition of nano-SiC to the Bi_{0.3}Sb_{1.7}Te₃ composite can produce an almost 50% increment in its m^* . In addition, the matrices with mismatched interfaces with SiC nanoparticles, where the energy filtering effect was not possible, exhibited evidently improved thermoelectric performances. This behavior was

attributed to the enhanced phonon scattering and reduced mean free path of the phonons, caused by the dispersion of SiC nanoparticles at the phase boundaries of the TE matrices.^[133,135,142,160] Therefore, the feasibility of improving the zT value of TE materials by dispersing SiC nanoparticles, has been confirmed.

2.4. Carbonic Dispersion

2.4.1. 1D Carbon Nanotubes Dispersion

The inclusion of 1D particles in TE matrices demonstrates the concept of employing low-dimensionality components to suppress the total thermal conductivity and thus increase the zT value of TE materials. As a first attempt, Ag nanowires have been introduced in a Bi₂Te₃ matrix to increase the zT value by constructing a 1D/3D structure.^[161] Carbon nanotubes (CNTs), as a 1D material, exhibit intriguing physical, chemical, and mechanical properties, including extremely high charge-carrier mobility,^[162] large aspect ratios,^[163] super hydrophilic properties,^[164] high thermal conduction,^[165] high strength,^[166] etc. CNTs can exhibit metallic or semiconductive electrical activity depending on their chiral indices (n , m), with metallic tubes accounting for approximately one-third of the potential armchair-type CNT structures and semiconducting tubes accounting for the other two-thirds.^[167] In general, multi-walled CNTs are characterized by metallic behavior, whereas single-walled CNTs (SWCNTs) are determined by their chirality.^[168]

Many studies have concentrated on integrating CNTs into various thermoelectric matrices, driven by the benefits discussed above.^[169–174] **Figure 12** illustrates some of these systems results. Since CNTs are 1D materials, scattered phonons with various length scales interact with each other, resulting in a substantially decreased total thermal conductivity. As shown in **Figure 12**, the addition of CNTs substantially reduced the thermal conductivities of the matrices (20–67%), as a result of carrier scattering induced by interface modification. However, because of the different preparation methods and CNT contents, a singular mechanism cannot be used to explain the variations in the electrical properties of different 1D/3D CNT-containing systems. The typical examples of incorporating CNTs into the matrix are seen in **Figure 13a**. It has been stated that the energy barrier should be adjusted to 0.2 eV in order to obtain optimal energy filtering effect.^[175] Some research found that increasing the CNT concentration increased electrical conductivity,^[172,174,176,177] whereas others found the reverse.^[178–181] The changing CNT content might explain this discrepancy. Furthermore, it is difficult to demonstrate the general changes caused in terms of thermoelectric performance based on the volume or mass of the CNTs used for TE material modification, because there is insufficient information concerning their nature (diameter, length, chirality, and conductivity). The resistance generated by poor electrical contacts between individual carbon nanotubes in nanocomposites with low CNT concentration induces a lower effective electrical conductivity.^[178] By increasing the dispersion of the second phases, additional electrical conducting paths throughout the CNTs channels will be formed, implying that controlling the CNT content is

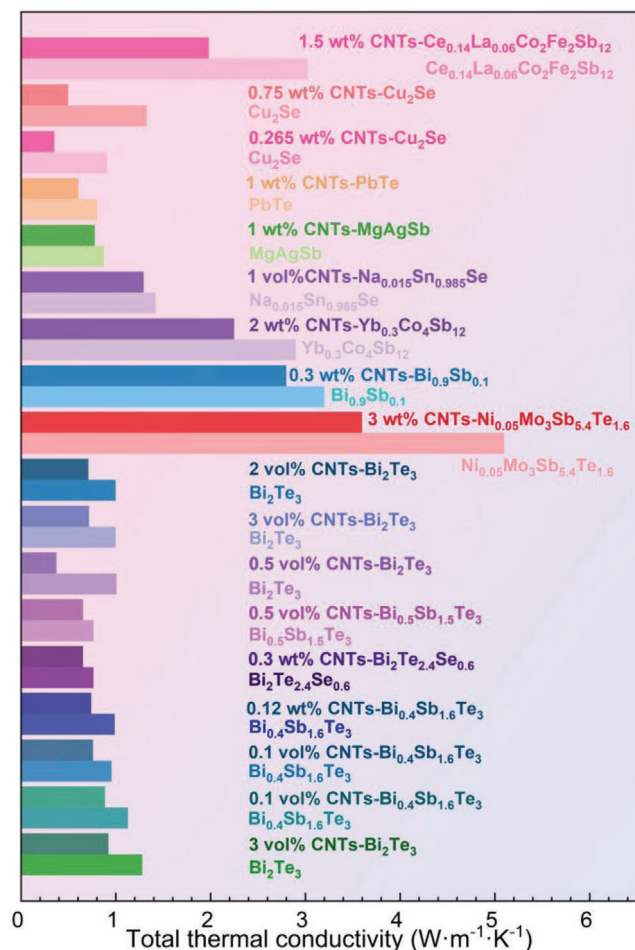


Figure 12. Comparison of total thermal conductivities before and after dispersing CNTs into different TE materials at 300 K. [171,172,174,178–180,187–199]

critical for modifying the carrier transportation at the interfaces. According to the percolation theory,^[182] an ideal model can be proposed to summarize the effects of CNT incorporation on the electrical properties of the TE matrix, as schematically illustrated in Figure 13b. The percolation threshold is determined by the aspect ratio of the CNTs and their uniform dispersion in the composites. Materials modified by CNTs with an aspect ratio of 1000 require, on average, approximately 0.1 vol% to form an interconnected network across the composites.^[178,183,184] Furthermore, the most widely observed percolation threshold in carbon nanotube-based materials ranges between 0.1 and 1.0 vol%.^[178,185,186] According to Bark et al.,^[173] in the CNTs-Bi₂Te₃ system, σ first increased and then decreased with increasing CNTs content (<20 vol%), which may corroborate our hypothesis but requires further investigation by other researchers.

However, the excessive agglomeration of CNTs seems inevitable due to their high surface energy and flexible nature. The most challenging obstacle to overcome before employing CNTs as nanoinclusions in TE materials is developing a technique to uniformly distribute them in the material matrix. Generally, two methods are being discussed in the literature to achieve the uniform dispersion of CNTs in TE matrices:^[171–173,188,191,193,199–202]

one is incorporating the CNTs via a ball-milling process into the conventionally produced TE matrix powder, as demonstrated by the typical SEM image of a CNTs-Bi₂Te₃ system in Figure 14a. The ball-milling process, however, may shorten the length of the CNTs or compromise their inherent 1D nature.^[203] The other strategy includes the use of techniques such as hydrothermal/solvothermal synthesis, in which the matrix is synthesized within a liquid and then the CNTs are added and stirred. Such wet-chemical processes can preserve the desired length of the CNTs, but they present a major drawback in the potential introduction of unexpected residual impurities, which may significantly deteriorate the thermoelectric properties of the matrix (especially for oxygen/water sensitive materials).^[193]

Nunna et al. for the first time introduced the in-situ growth of Cu₂Se on the CNTs surface, achieving a high degree of uniformity in their dispersion along the Cu₂Se matrix boundaries (the fabrication process is shown in Figure 14b).^[193] The delocalized π electrons enhance the chemical reactivity of CNTs, allowing them to interact with various oxides and metals. According to theoretical calculations, the interactions between Cu atoms and molecular CNTs are substantially strong, allowing for a bonding energy of 0.24 eV to be achieved, as the distance between Cu atoms and CNTs is 1.83 Å. The high interaction energy achieved through this in-situ method can be exploited to separate the agglomerated CNTs and incorporate the nanoinclusions into the host materials. When a Cu₂Se/CNTs system was experimentally evaluated, a ball-milling process was applied to blend the CNTs, Cu powder, and Se powder together. During the ball-milling process, the Cu powder acted as a control agent and prevented the agglomeration of CNTs, in accordance with the theory discussed above, and simultaneously reacted with the Se powder to form Cu₂Se compounds. This in-situ synthetic process assures the formation of dense and nano-grained Cu₂Se species around each separated CNT, resulting in the homogeneous distribution of CNTs while preventing re-agglomeration. Figure 14c demonstrates the uniform dispersion of a high CNTs content (0.75 wt%) in the Cu₂Se matrix. Further investigations revealed that there was no obvious crack formation or amorphous phases presence in the interfaces of the CNTs/Cu₂Se system, and also that the CNT walls were parallel with the (111) lattice planes of the Cu₂Se species in the Cu₂Se/0.75 wt% CNT sample (Figure 14c). Due to the modified interfaces, the total thermal conductivity was only 0.4 W m⁻¹ K⁻¹ for the entire temperature measuring range. Compared with pristine Cu₂Se, there was a 65% reduction of thermal conductivity at 1000 K for the 0.75 wt% CNTs sample, despite the deterioration of the PF as a result of CNTs insertion.

The extraordinary mechanical properties of CNTs have been well established in the field.^[200,201,204] Single-walled carbon nanotubes possess a Young's modulus of ≈ 1 TPa^[205] and their tensile strength can reach to ≈ 50 –200 GPa;^[206] thus, they are considered as a good alternative for strengthening the mechanical properties of TE materials. Briefly, after being dispersed among the adjacent grains of the TE material, they strengthen the adhesive forces between them and act as reinforcing “binders.” As shown in Figure 15a, the Vickers hardness and flexural strength of CNT-reinforced polycrystalline Na_{0.015}Sn_{0.985}Se increased along with the increasing CNT content.^[194] Particularly, after introducing 1.0 vol% CNTs, compared

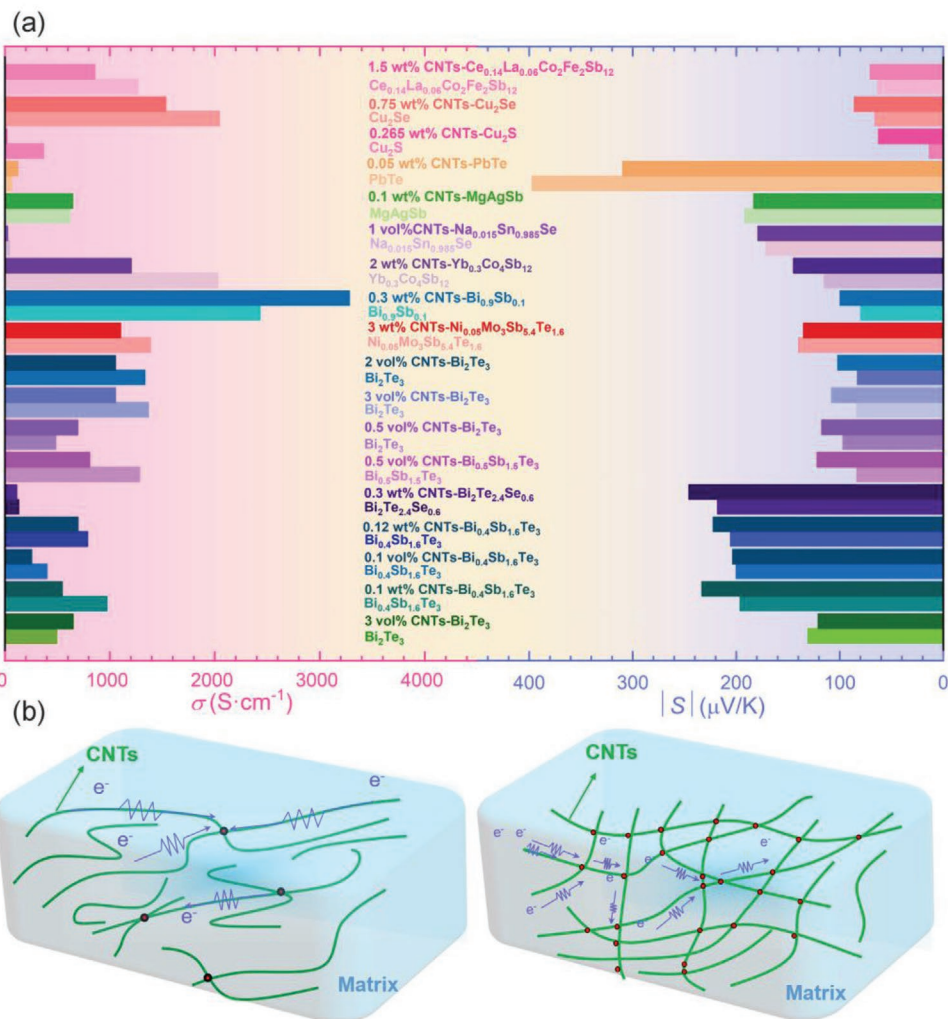


Figure 13. a) Comparison of electrical conductivity and Seebeck coefficient before and after dispersing CNTs into different TE materials at 300 K.^[171,172,174,178–180,187–199] b) Schematic diagram of electrically conductive paths under low (left) and high (right) CNTs content.

with pristine Na-doped SnSe, the Vickers hardness and flexural strength improved by 59.8% and 47.9%, respectively. These mechanical enhancements can be further elucidated with the load–displacement graph (Figure 15b). The CNT-free polycrystalline SnSe sample exhibited brittle fracturing and was unable to impede crack propagation even at the low bending force of 5 N. However, after the CNTs addition increased to 1.0 vol%, the effective load carrying capability of the sample increased by approximately 50%, as confirmed by the load–displacement curve. Figure 15c shows a SEM image of the CNTs distribution at the grain boundaries of a $\text{Bi}_{0.4}\text{Sb}_{1.6}\text{Te}_3$ composite, achieved by ball-milling $\text{Bi}_{0.4}\text{Sb}_{1.6}\text{Te}_3$ powder with multiwall CNTs, followed by sintering.^[187] The high bending strength of 90 MPa was achieved, which was almost three times higher than the maximum bending strength of the parent material (32 MPa). The strengthening mechanism was attributed to the transfer of the load from the matrix to the mechanically superior CNTs. Furthermore, the CNTs acted as bridges between the cracks and were exposed during the process of crack propagation

(Figure 15c). Such a strengthening mechanism is quite similar to steel-reinforced concrete.

2.4.2. 2D Graphene Dispersion

Interfaces, grain boundaries, and heterophane boundaries are low-dimensional structures that behave differently from 3D bulk phases.^[193] They can be collectively generalized as grain boundary complexions, which may include different amounts of impurity atoms at their interfaces. Owing to their extraordinarily high surface area and grain-boundary-like morphology, 2D nanoparticles are prospected to exhibit a rather prominent effect on improving thermoelectric performance, compared with their 1D equivalents. Theoretically, materials with quasi-layered crystal structures, such as graphene,^[207–216] are considered good dispersion candidates for TE materials.

Graphene dispersion can be viewed as the prospect of utilizing 2D components to modify the interface of TE

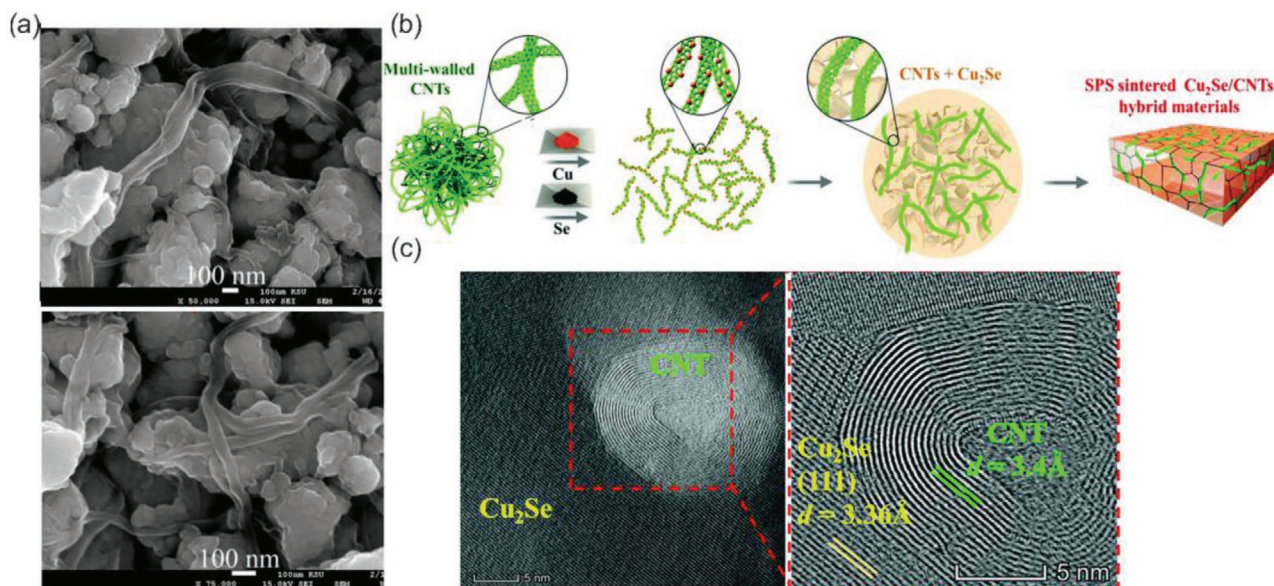


Figure 14. a) SEM image of Bi₂Te₃ with 1 vol% CNTs;^[188] Reproduced with permission.^[188] Copyright 2017, IOP Publishing Ltd. b) Fabrication process and formation mechanism of the in-situ growth of Cu₂Se on CNTs surface; c) Spherical aberration-corrected scanning transmission electron microscopy (STEM) images for the Cu₂Se sample with 0.75 wt% CNTs.^[193] Reproduced with permission.^[193] Copyright 2017, The Royal Society of Chemistry.

materials. Graphene is acclaimed as a revolutionary 2D material, given its excellent electrical conductivity,^[217] large specific surface area,^[218] high mechanical strength,^[219] and versatile functionalization.^[220] Numerous successful examples of

graphene-incorporated thermoelectric composites have been demonstrated.^[59,213,215,221,222] Increasing the electrical conductivity of compounds via graphene addition is a facile process, but it may also increase the electrical thermal conductivity.

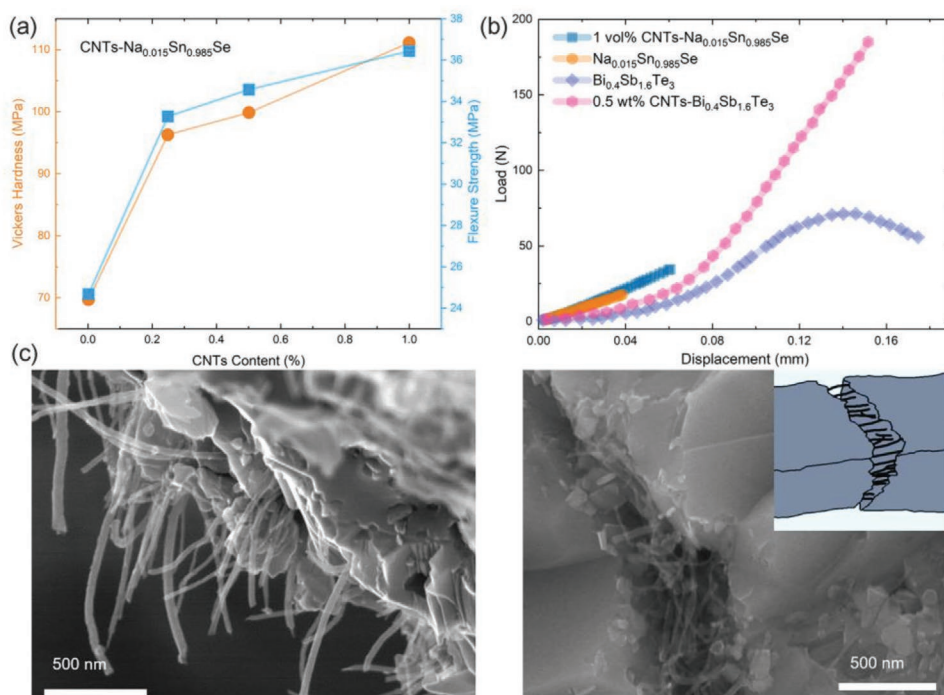


Figure 15. a) The Vickers hardness and flexural strength of a Na_{0.015}Sn_{0.985}Se composite with different CNT contents;^[194] b) Load–displacement graph of the Na_{0.015}Sn_{0.985}Se^[194] and Bi_{0.4}Sb_{1.6}Te₃^[187] composites with and without CNT addition; c) The distribution of CNTs at the grain boundaries on the fracture surface of Bi_{0.4}Sb_{1.6}Te₃.^[187] The inset shows a schematic illustration of the CNTs bridging mechanism. Reproduced with permission.^[187] Copyright 2013, AIP Publishing.

Therefore, there is a tradeoff between increasing the electronic conductivity and decreasing the lattice thermal conductivity in the process of determining the effect of graphene on the total thermal conductivity. It should be noted that the graphene used to prepare most composites is a chemically derived material (i.e., graphene oxide (GO)), with a slightly lower electrical conductivity than graphene with a perfect 2D structure, rendering the thermoelectric performance adjustment easier.^[223–226] For the first time, Feng et al.^[222] introduced a new approach for embedding GO into p-type CoSb₃ semiconductor thermoelectric systems via an in-situ solvothermal route, followed by hot pressing. For comparison, they also mixed CoSb₃ and GO powders and measured the thermoelectric performances of both systems. The in situ method for GO addition increased σ from 10.5 to 510 S cm⁻¹, while moderately decreasing S from 65 to 30 μ V K⁻¹ at 300 K (Figure 16a,b). Additionally, the charge carrier mobility of the sample prepared by mixing the constituents rose from 25 to 52 cm² V⁻¹ s⁻¹ and exhibited higher carrier concentration and Hall mobility compared to those of pristine CoSb₃. This was theoretically attributed to the inherent p-type thermoelectric properties of GO, which provided additional charge carriers,^[227,228] thereby raising the total thermal conductivity (Figure 16c). However, there are certain reports in the literature concerning a minor, if not negligible, negative effect of GO addition on the electrical conductivity of TE materials, such as the GO-Ce_{0.85}Fe₃CoSb₁₂^[229] and GO-Yb_{0.27}Co₄Sb₁₂^[230] systems, which could be due to the fabrication process and graphene thickness.

Due to its 2D nature, graphene can behave like a net, forming a stable 3D network structure that can benefit from phonon scattering to reduce thermal conductivity, as illustrated

in Figure 17a.^[175] The GO-Yb_{0.27}Co₄Sb₁₂^[230] system achieved an ultralow κ_l of ≈ 0.57 W m⁻¹ K⁻¹ at 750 K, which increased the peak zT value to 1.51 (Figure 17b). On the other hand, the carbon allotrope composition level must be carefully optimized. Increasing the amount of GO addition after reaching the optimized level (≈ 0.72 vol%) in Yb_{0.27}Co₄Sb₁₂ results in increased κ_l and deteriorated zT values, which should be primarily attributed to the increased reduced-GO (rGO) layer thickness. Further to that, at the optimized level (≈ 1.4 vol%), the p-type GO-Ce_{0.85}Fe₃CoSb₁₂ system exhibited a 20% reduced κ_l value and its zT was increased to 1.06 at 700 K, without demonstrating a significantly deteriorated electrical performance.^[229]

Aside from the effect of graphene on TE performance, graphene addition with a 3D network can inhibit grain growth during the sintering process due to graphene segregation at grain/particle boundaries, which may improve the mechanical properties of the TE matrix according to the Hall-Petch theory and pile-up of dislocations, preventing them from freely moving throughout the matrix. This extension in the dislocation paths (loops) results in higher ductility of the nanocomposites. These loops can also generate back stresses and prevent dislocation motions.^[61]

2.5. MXenes Dispersion

Transition metal carbides, carbonitrides, and nitrides (MXenes) are some of the most recent additions to the catalogue of 2D materials.^[231] Their general chemical formula is M_{n+1}X_nT_x ($n = 1-3$), where M is the transition metal, X represents carbon and/or nitrogen, and T_x corresponds to the surface terminations

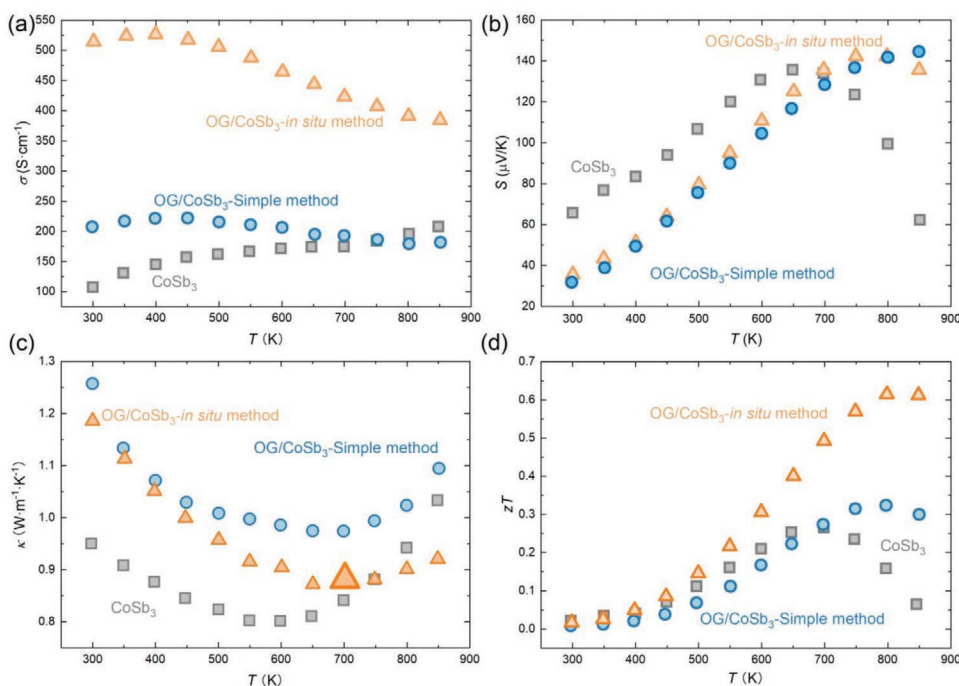


Figure 16. Temperature dependence of a) electrical conductivity, b) Seebeck coefficient, c) total thermal conductivity, and d) zT of bulk CoSb₃, CoSb₃-simple mixture, and CoSb₃-in situ method samples.^[222]

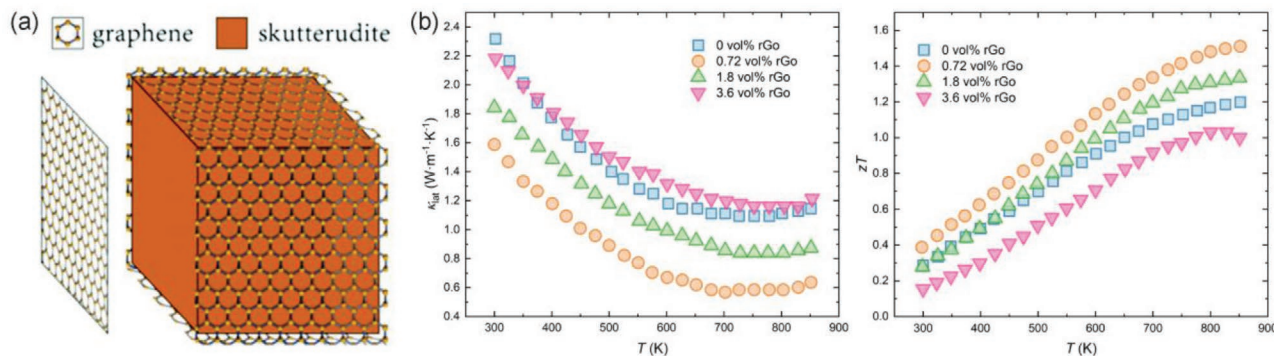


Figure 17. a) 3D network after graphene addition;^[229] b) Temperature dependence of lattice thermal conductivity and zT values of Yb_{0.27}Co₄Sb₁₂ systems with different rGO contents.^[230] Reproduced with permission.^[229] Copyright 2016, The Royal Society of Chemistry.

(e.g., hydroxyl, oxygen, fluorine, where x is the number of terminating groups).^[232] In the MXenes structure, $n+1$ layers of M cover n layers of X with the arrangement of [MX] _{n} M. Compared with chemically obtained graphene, MXenes possess both hydrophilicity and metallic transport properties, with high electrical conductivity.^[233] Their remarkable electrical properties render them auspicious candidates for improving the electrical performance of TE materials. An example of the significant improvements that they can deliver on the electrical properties can be observed by dispersing Ti₃C₂T _{x} into a ZnO matrix.^[234] The prepared MXenes solution was mixed and sonicated with the ZnO, followed by flash freezing, and then freeze-drying to obtain a homogeneous Ti₃C₂T _{x} dispersion. Subsequently, acetic acid was added to the ZnO-Ti₃C₂T _{x} mixture, which was then homogenized before hot pressing. The high-angle annular dark-field STEM (HAADF-STEM) and EDS mapping images confirmed the distribution of the Ti₃C₂T _{x} nanosheets around the ZnO grains. Following the dispersion of 1 mol% MXenes, the electrical conductivity of the

system increased by two orders of magnitude (compared to the pristine sample), and the overall PF improved dramatically, reaching 4.5×10^{-4} W m⁻¹ K². Lu et al.^[235] were the first to attempt the dispersion of highly-conductive Ti₃C₂T _{x} MXenes into a Bi_{0.4}Sb_{1.6}Te₃ matrix and explained the underlying scattering mechanism. The Ti₃C₂T _{x} nanosheets were obtained by etching Ti₃AlC₂ powder in the LiF/hydrochloric acid solution (Figure 18a). Then, the Ti₃C₂T _{x} and Bi_{0.4}Sb_{1.6}Te₃ powders were uniformly mixed by following a self-assembly protocol. The carrier concentration increased from 1.67×10^{19} to 3.7×10^{19} cm⁻³ at 300 K and the scattering mechanism was altered with the MXenes dispersion, which was theoretically attributed to the energy barrier scattering. Because of the partial elimination of the -F groups during the pressing process, the Ti₃C₂T _{x} exhibited metallic electrical conductivity behavior by forming typical metal-semiconductor contacts in the MXenes/TE matrix interfaces. According to theoretical calculations,^[235] the work function will increase with the increasing O content until being equalized with that of the matrix when $x = 1$ (Figure 18b). The

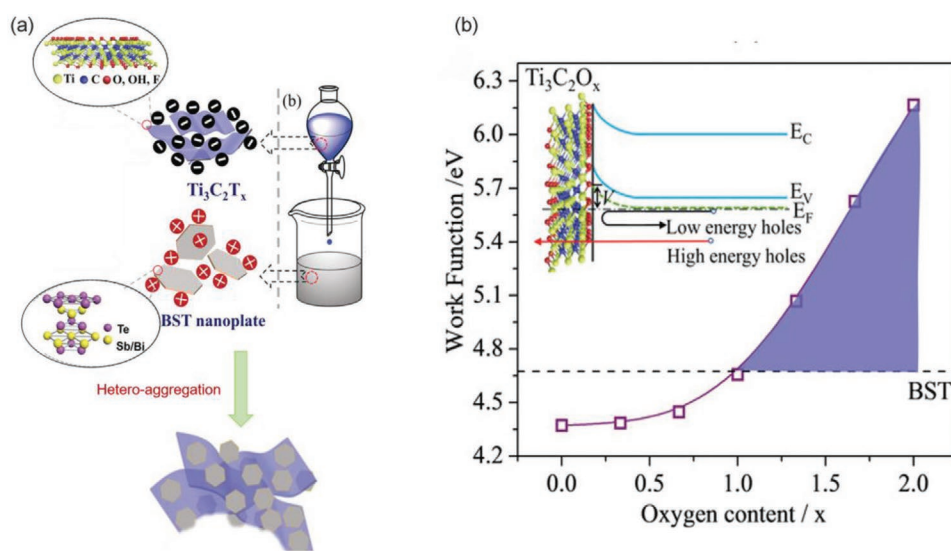


Figure 18. a) Schematic illustration of the Ti₃C₂T _{x} nanosheets/BST nanoplates system preparation method; b) The work function of Ti₃C₂T _{x} as a function of oxygen content.^[235] Reproduced with permission.^[235] Copyright 2019, WILEY-VCH Verlag GmbH & Co. KGaA, Weinheim.

X-ray photoelectron spectroscopy (XPS) results revealed a stoichiometric ratio of Ti:O \approx 3:1.5, along with a higher work function than that of the matrix, indicating that hole carriers may be injected from the MXenes to Bi_{0.4}Sb_{1.6}Te₃ (which caused the carrier concentration to increase). The above, combined with the strong scattering of phonons with short and medium wavelengths, suppressed the thermal conductivity by a great extent, thereby enhancing the zT value to 1.3 at 400 K. It should also be considered that by increasing the volume percentage of Ti₃C₂T_x, the Hall mobility decreased from 240 to 110 cm² V⁻¹ s⁻¹ at 300 K, which may have resulted from the obstruction of carrier transport at the heterointerfaces. Because Ti₃C₂T_x possesses the lowest intrinsic mobility in the MXenes family (0.7 cm² V⁻¹ s⁻¹),^[235] its 2D nanosheet conducting network cannot provide a detour for the carriers to promote mobility. However, CNTs can provide the conductive path. For instance, the Ti₃C₂T_x-CNTs system is characterized with electrical properties, which may impact its difference on Hall mobility.^[236] Summarizing, increasing the Ti₃C₂T_x content in the Ti₃C₂T_x-SWCNTs system significantly inhibits its electrical conductivity, while moderately increasing the S value. As a result, the inhibiting effect on Hall mobility discussed above, is the primary distinction between dispersing MXenes or CNTs in TE materials.

2.6. Opportunities and Challenges in Discontinuous Interface Modification

As stated in this section, most attempts to directly disperse second phase in various TE matrices have focused on increasing the Seebeck coefficient while decreasing thermal conductivity. The numerous matrix and dispersion options may contribute to the development of TE materials used from low to high temperatures. Although the benefits of adding a second phase have been extensively documented, there are certain issues that need be investigated further through experimentation.

- 1) Reduced metal particle size may result in a lower metal melting point, which may cause the diffusion of metal into the matrix and give an additional carrier. As a result, it is difficult to differentiate the increase in carrier produced from metal–semiconductor contact from the diffusion effect, as observed for Au–Bi₂Te₃^[65,91] and Au–Sb₂Te₃.^[91] To confirm the source of TE property variation, a comparison of the dispersion and doping methods on the TE properties is required. Furthermore, when the TE matrix has extremely poor electrical conductivity, it is difficult to significantly improve overall electrical conductivity, even with metal particle dispersion, as seen in the Ag–Ca₃Co₄O₉^[237] and Au–ZnO systems.^[238]
- 2) Because most oxide compounds have low electrical conductivities, degradation of electrical properties is unavoidable. To relieve the deterioration of electrical characteristics, high conductive oxide compounds such as RuO₂,^[239] ReO₃^[240] and IrO₂^[241] can be used. Among them, RuO₂ has been successfully used to improve the electrical conductivity of the BiSbTe alloy.^[242]
- 3) The energy filtering effect has been used in many studies on second phase dispersion in TE materials as an appealing explanation for the decoupling materials' Seebeck coefficient

and conductivity. However, we assess that several of those studies did not give enough data to back up their claims^[243–245] or show any advantage from energy filtering.^[246–248] For instance, Lin et al.^[58] believe that the terms of decoupling and energy filtering should be used when an experimentally self-consistent heterogeneous transport model instead of homogeneous transport assumption is applied in analysis. Therefore, these concepts should be used carefully and properly.

3. Continuous Interface Modification

The continuous interface modification strategy entails commonly used chemical routes, in which atoms or molecules are assembled into the grain boundary and heterostructures are created. In general, continuous surface modification can be divided into two categories, gas phase synthesis and liquid phase synthesis, all of which are referred to as “bottom-up” methods. On the other hand, directly mixing the second phase into the TE matrix decorates the dispersions on the boundaries and creates discontinuous islands, which can be referred to as the “top-down” process. Top-down approaches typically generate relatively large amounts of nanoparticles (\approx g scale) with wide particle size distributions, while offering easy material selectivity and require less complicated instrumentation. Conversely, bottom-up methods produce fewer nanoparticles (\approx mg scale) and have the benefits of offering better control over the morphology of the core–shell structure and can significantly improve TE performance. In either case, the use of continuous interface adjustment methods is highly encouraged for improving the zT values.

3.1. Gas Phase Methods

The above interface modification techniques primarily focus on the inclusion of second phases; however, there exists a subtraction route for the elimination of second phase by annealing in different gas atmospheres. The fine powder can be oxidized during the synthetic process due to its high specific surface area. Since certain oxides exhibit high thermal conductivity, their presence on grain interfaces can dramatically weaken the TE material's electrical properties, while increasing its thermal conductivity. For example, as polycrystalline SnSe is exposed to air, it readily oxidizes and forms a SnO/SnO₂ coating layer, resulting in an increase in total thermal conductivity and thereby obscuring the intrinsically low κ_L . Furthermore, the formation of the SnO/SnO₂ layer introduces a significant off-stoichiometric defect in the pristine SnSe. Shimizu et al. investigated the effect of air exposure on the thermoelectric properties of SnSe thin films.^[249] Before annealing, the SnSe film exhibited a large positive S of 757 μ V K⁻¹. However, its strong thermoelectric effect was fully suppressed after just a few minutes of air annealing, suggesting that oxidation can cause a dramatic thermopower inversion and that extracting the oxide compound via a gas removal method is needed for certain TE systems. Lee et al. employed the gas removal process (removing oxide layer by gas) and achieved a near-single-crystal thermoelectric performance on the resulting polycrystalline SnSe system.^[250]

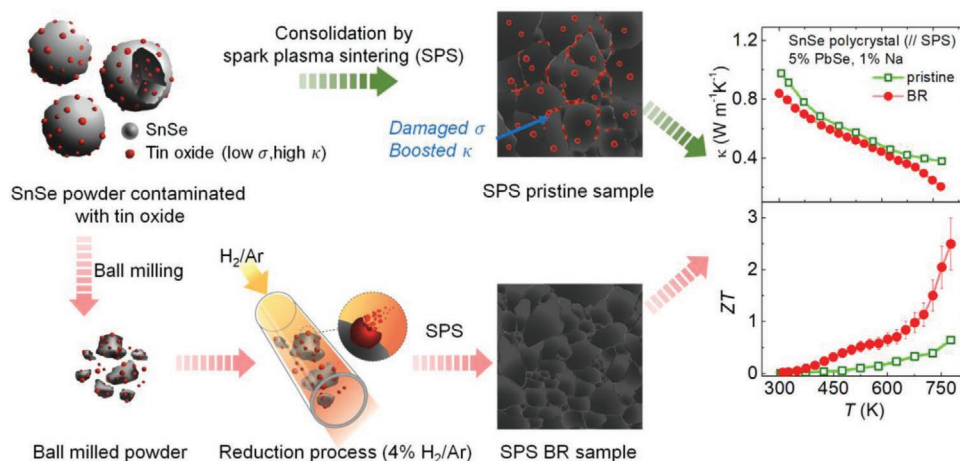


Figure 19. A schematic illustration of the oxide removal process and its effect on the thermoelectric properties of polycrystalline SnSe.^[250] Reproduced with permission.^[250] Copyright 2019, Elsevier.

By ball-milling the ingot after following traditional melting methods, and then annealing in a 4% H₂/Ar atmosphere at 613 K for 6 h, yielded the SnSe powder (Figure 19). After removing the oxide compounds, the overall thermal conductivity of the modified polycrystalline SnSe was notably lower than that of the Na-doped single crystal. The positive effect of oxide elimination is also seen in the enhancement of σ and S , leading to a 2.19-fold increase in PF as compared to pristine SnSe powder. These findings indicate that the application of the gas-phase annealing process with hydrogen would effectively strip the majority of oxide compounds from the SnSe grains, while also improving their electrical and thermal properties.

The central concept underlying the gas phase synthetic process, apart from eliminating the second phase via gas removal, is shaping the core-shell structure by uniformly depositing the “shell” materials. According to the growth mechanism, the approach of gas phase synthesis can be mainly classified into physical vapor deposition (PVD) and chemical vapor deposition (CVD). PVD methods are deposition processes where coatings are grown on the substrate, thereby necessitating the atomization or vaporization of the material from one or several solid sources (usually called targets). It should be noted that the PVD process can change the surface properties and the transition zone between the substrate and the deposited material. In addition, the substrate characteristics can also affect the film properties. The PVD deposition process can be conducted in a gaseous vacuum, plasma, or electrolytic environment.^[251,252] The top panel of Figure 20a shows the epitaxial growth of orthorhombic SnS–Sn_xSe_{1-x} core-shell structures using a two-step PVD method.^[253] The SnS flakes that were initially grown on the mica substrate and the pre-synthesized SnS/mica were used as the deposition substrate for the next step. Next, the SnSe powder was heated up to 740 °C and the gas phase was obtained. Using Ar flow, the SnSe gas phase was transferred to the pre-synthesized SnS/mica spots and deposited around the flakes. The bottom panel of Figure 20a displays the optical image of the core-shell structure and its Raman characterization, confirming the SnS and Sn_xSe_{1-x} compositions of the inner and the outer regions, respectively. Li et al. fabricated

Te-TiS₂ nanocables using a similar PVD method.^[254] The core-shell structure can be clearly observed in Figure 20b, which also illustrates the shell thickness and core diameter of 20 nm. The thermoelectric performance of the fabricated nanocables, which can be directly measured by specially designed devices, can also be affected by their different diameters. Stemming from the increased grain boundary scattering, this unique core-shell structure contributed to carrier scattering and the suppression of the phonon-drag phenomenon, leading to a significant enhancement of the zT value to 1.91 at 300 K (with 60 nm diameter). Since the PVD method is primarily based on the evaporation of the deposition materials and their subsequent removal via gas flow, it does not induce chemical bonding and may cause the formation of multilayers.^[255] As illustrated in the schematic diagram in Figure 21a, the layer-structured Bi₂Te₃ on the SWCNTs scaffold was synthesized using a magnetron sputtering technique.^[256] The highly ordered (000 l)-textured Bi₂Te₃ nanocrystals were anchored on high quality SWCNTs bundles and the crystallites were decorated on their surfaces (Figure 21b). The low lattice thermal conductivity of $0.26 \pm 0.03 \text{ W m}^{-1} \text{ K}^{-1}$ was obtained for the Bi₂Te₃-SWCNTs, which was close to the minimum lattice thermal conductivity of $0.28 \text{ W m}^{-1} \text{ K}^{-1}$.^[253] This ultralow lattice thermal conductivity was theoretically derived from the high density of multiscale defects, such as Te vacancies/Te_{Bi} antisites, dislocations, phase interfaces, stacking faults, grain/twin boundaries, and randomly distributed nanopores, which significantly contributed to the scattering of a wide wavelength-range of phonons. Combined with the moderate PF, the zT of the flexible free-standing Bi₂Te₃-SWCNTs hybrid was increased to ≈ 0.9 at 300 K (Figure 21c).

The CVD method can have similar results in regard to the interface modification of the core-shell structure. During the CVD process, the vapor-liquid-solid (VLS) mechanism serves as the typical growth model and the nanowires/nanoplates can be epitaxially grown on the substrate with the aid of precursors along a specific direction, that is controlled by the lowest formation energy. Wingert et al. fabricated p-type Si-deposited Ge nanowires with different diameter ratios ($R_{\text{Si}}/R_{\text{total}}$) using the CVD method,^[257] and by tuning the $R_{\text{Si}}/R_{\text{total}}$ ratio they achieved

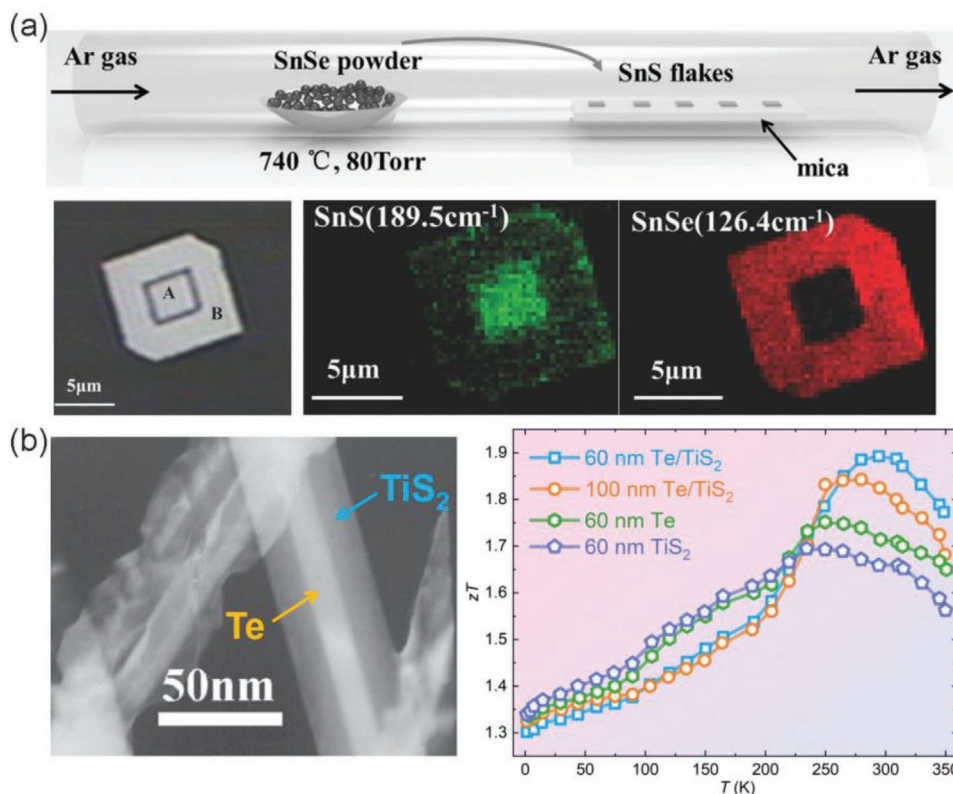


Figure 20. a) Schematic illustration of PVD growth of layered SnS–SnS₂Se_{1-x} core–shell heterostructures and the corresponding Raman intensity maps;^[253] Reproduced with permission.^[253] Copyright 2016, WILEY-VCH Verlag GmbH & Co. KGaA, Weinheim. b) TEM image and temperature dependence of *zT* values for Te–TiS₂ nanocables.^[254] Reproduced with permission.^[254] Copyright 2016, IOP Publishing Ltd.

different *S* and σ values. When the R_{Si}/R_{total} reached 0.79, the maximum PF of $36 \pm 6 \mu\text{W cm}^{-1} \text{K}^{-2}$ was obtained, which was much higher than that of bulk Ge. Similarly, the intrinsic Si nanowires were coated with B-dope Si using CVD method.^[258] The diameters of the synthesized coated nanowires ranged between 20 and 200 nm. Notably, the thermoelectric performance changed with the different diameters, indicating that the core–shell structure characteristics had a huge influence on the electrical behavior. These results verify that the appropriate core–shell structure design can be beneficial for achieving high thermoelectric performances; however, the line-of-sight transfer processes typically employed in PVD coating techniques can hinder the full coverage of complex geometries. Also, the non-conformal step coverage of CVD/PVD methods can be considered a major drawback when the modification of rugged surfaces is desired. Moreover, the above methods are mainly used in the fabrication of low-dimensional material devices, for example, nanowires or thin films, while the preparation technologies of applied thermoelectric generators are mainly dependent on bulk materials sintered from TE material powder. Thus, applying methods that enable the conformal coating of particles and complex surface geometries provide with beneficial and interesting alternatives.

As a layer-by-layer deposition technique, atomic layer deposition (ALD) is known for its unique capability of depositing highly uniform films in a controlled manner.^[259,260] Compared

with traditional CVD methods, the precursors in ALD are always kept separated and pulsed alternatively into the chamber with a purging phase in between.^[261] Thanks to the controlled layer-by-layer growth, ALD can uniformly coat any structure: from planar substrates, to 3D structures, trenches, and holes. The thickness control can be down to the atomic level, enabling the deposition of extremely thin films, even only a few atoms thick. Using this technique, Mattinen et al. deposited uniform crystalline SnS₂ films on nanoscale trench structures.^[259] Film conformality was further determined via TEM-EDS mapping, where the Sn/S elements were confirmed to homogeneously cover the nonplanar surfaces. This remarkable feature indicates that the ALD method can be effectively applied on powder surfaces. As shown in **Figure 22a**, the concept of powder ALD (PALD) can be divided into two procedures: preparing a thermoelectric powder with an adequately tiny size and coating the shell materials with a rotation process.^[262] The rotation process, combined with the small size of the powder particles, ensures a uniform coating even with a few cycles. Briefly, the powder size (*d*) and the potential energy barrier must be specifically designed to satisfy the relationship that τ_p (phonon momentum relaxation length) $< d < \tau_e$ (electron momentum relaxation length); in this manner, *S* will be improved without significantly decreasing σ , resulting in a substantial net improvement of PF.^[262] Additionally, a large reduction in thermal conductivity can be achieved by

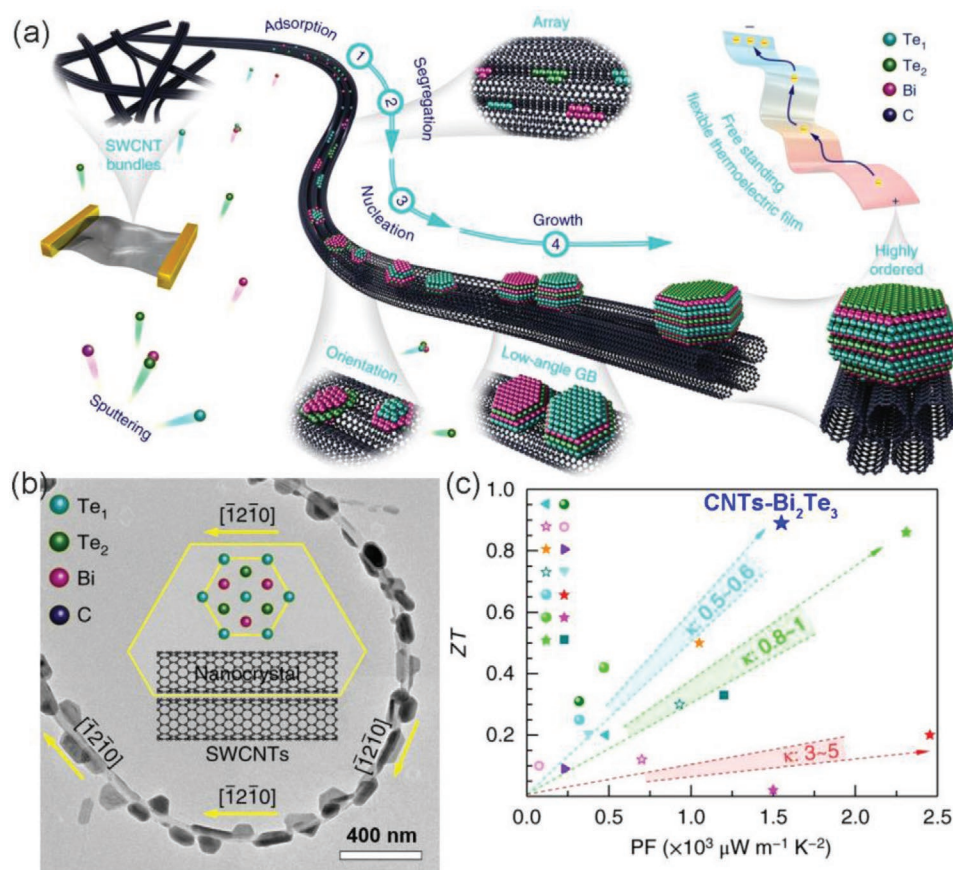


Figure 21. a) Schematic illustration of the magnetron sputtering-based fabrication process and structure of a free-standing highly ordered Bi₂Te₃-SWCNT composite; b) TEM image of the Bi₂Te₃-SWCNT composite; c) Comparison of various zT versus PF results in the literature for CNTs-Bi₂Te₃ at 300 K.^[256] Reproduced with permission.^[256] Copyright 2018, Springer Nature.

depositing a few layer of specific materials on the interfaces of the TE material particles.

The idea of modifying the interfaces of TE materials using PALD was reported for the first time by Li et al. in 2016.^[262]

By employing a continuous-flow ALD reactor, they achieved the deposition of an ultrathin ZnO layer on the surfaces of n-type Bi₂Te_{2.7}Se_{0.3} TE powder particles using the precursors of diethylzinc (DEZ) and H₂O. Intriguingly, there was a

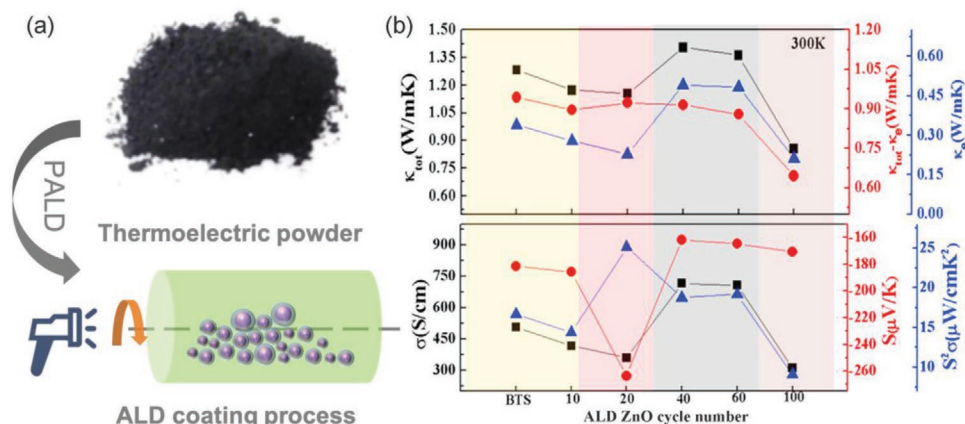


Figure 22. a) Schematic illustration of the PALD process;^[263] Reproduced with permission.^[263] Copyright 2019, American Chemical Society. b) Dependence of the ALD cycle number on the thermal and electronic transport properties of a ZnO layer at 300 K.^[264] Reproduced with permission.^[264] Copyright 2018, Elsevier.

proportional relation between the layer thickness and cycle number. Figure 22b presents the electrical and thermal transport values at 300 K for the samples coated with ZnO layers of varying thicknesses, indicating that both very thin (<1 nm) and thick (>6 nm) coating layers led to the vanishing of the carrier transports. The sample with the 2 nm-thick ZnO coating exhibited a high PF of $25.1 \mu\text{W cm}^{-1} \text{K}^{-2}$, derived from its strongly enhanced Seebeck coefficient of $-261 \mu\text{V K}^{-1}$, which resulted in a high zT value of 0.58 at 390 K. Driven from these results, ZnO was selected for PALD on the surfaces of p-type $\text{Bi}_{0.4}\text{Sb}_{1.6}\text{Te}_3$ powder particles, using the same precursors.^[263] As shown in **Figure 23a**, energy dispersive X-ray (EDX) elemental mapping revealed clear phase boundaries between the matrix and the ZnO layer of the coated sample after ten cycles. The excellent control of the PALD process increased the overall zT from 1.0 to 1.5 for the samples coated with an 8 nm-thick ZnO film. It is worth mentioning that the characterizations performed on the samples cut parallel and perpendicular to

the spark plasma sintering (SPS) direction showed the same values, indicating that coating with ZnO can eliminate anisotropies in the TE properties. Furthermore, the electrical resistivities of the samples showed a decreasing tendency between 0 and 5 cycles, whereas the opposite trend was observed between 6 and 15 cycles. This behavior induced the continuous reduction of the Hall mobility, even though the carrier concentration initially increased and then decreased. The results from the Zn K-edge extended X-ray absorption fine structure (EXAFS) analysis explained this phenomenon, by showing that Zn–Te bonds were formed during the initial growth stage (<10 cycles), which in turn caused the carrier concentration to increase (due to the interactions between DEZ and Bi_2Te_3). This phenomenon enabled the Zn ions to act as acceptors which substituted the Bi/Sb sites. As the cycle number increased (>10 cycles), however, the ZnO layer started to form and led to the decrease of the carrier concentration. This pattern was also confirmed in the $\text{ZnO}/\text{SnO}_2\text{-Bi}_2\text{Te}_{2.7}\text{Se}_{0.3}$ system after even less cycles (<10),^[265]

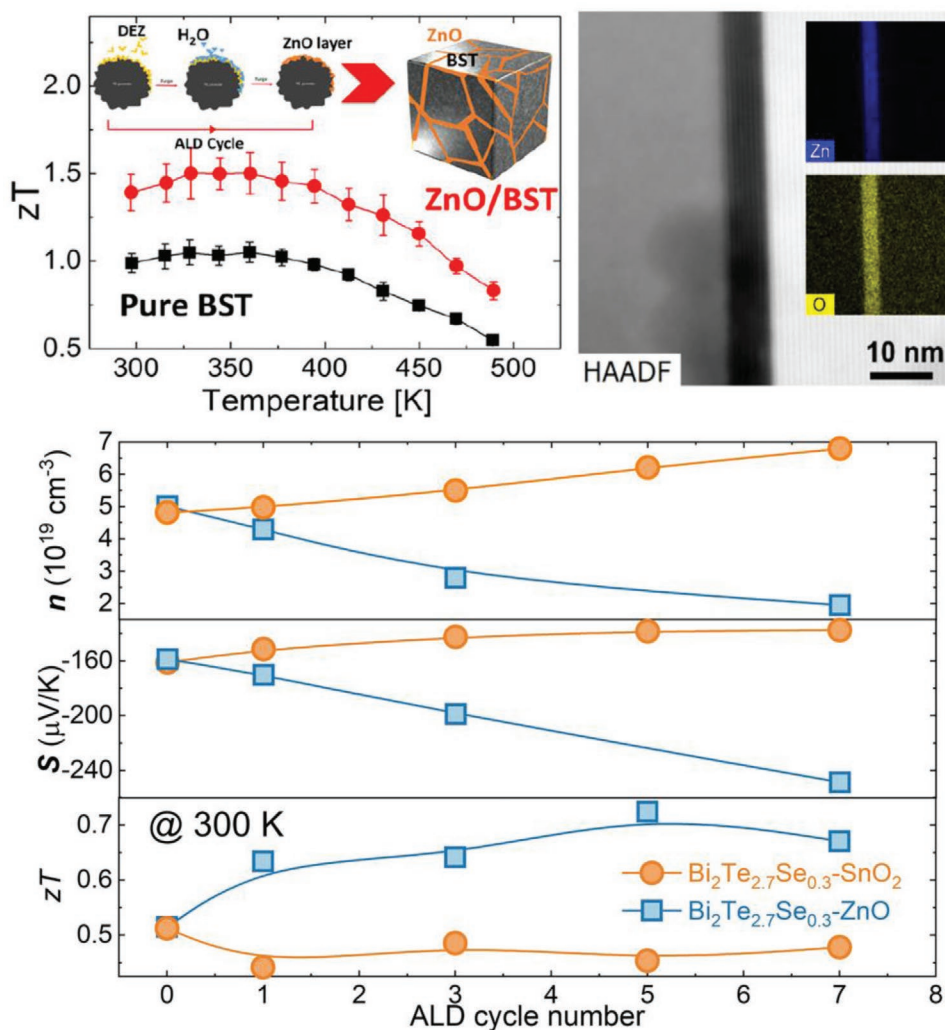


Figure 23. a) The TEM and EDS elemental mapping of the ZnO-coated $\text{Bi}_{0.4}\text{Sb}_{1.6}\text{Te}_3$ system and the temperature dependence of the zT values.^[263] b) ALD cycle number dependence on carrier concentration, Seebeck coefficients, and zT values for the SnO_2 - and ZnO-coated $\text{Bi}_2\text{Te}_{2.7}\text{Se}_{0.3}$ systems at 300 K.^[265] Reproduced with permission.^[263] Copyright 2019, American Chemical Society.

Table 2. Summary of typical TE systems coated with various materials using the PALD process.

Matrix	Shell	Optimum cycle number	Pristine maximum zT	Maximum zT after PALD	Ref.
$\text{Bi}_{0.4}\text{Sb}_{1.6}\text{Te}_3$	ZnO	10	1.06@360 K	1.52@360 K	[263]
$\text{Bi}_2\text{Te}_{2.7}\text{Se}_{0.3}$	TiO_2	10	0.69@400 K	0.91@430 K	[266]
$\text{ZrNiSn}_{0.99}\text{Sb}_{0.01}$	Al_2O_3	140	0.85@875 K	1.14@875 K	[267]
$\text{Bi}_2\text{Te}_{2.7}\text{Se}_{0.3}$	ZnO	5	0.52@300 K	0.73@300 K	[265]
$\text{Bi}_2\text{Te}_{2.7}\text{Se}_{0.3}$	SnO_2	7	0.52@300 K	0.48@300 K	[265]
$\text{Bi}_2\text{Te}_{2.7}\text{Se}_{0.3}$	ZnO	20	0.51@400 K	0.86@400 K	[269]
$\text{In}_{0.2}\text{Yb}_{0.1}\text{Co}_4\text{Sb}_{12}$	ZnO	5	0.69@687 K	0.64@687 K	[268]
$\text{In}_{0.2}\text{Yb}_{0.1}\text{Co}_4\text{Sb}_{12}$	SnO_2	1	0.69@687 K	0.57@687 K	[268]

where the carrier concentration in the ZnO-coated sample continuously decreased. On the contrary, the carrier concentration in the SnO_2 -coated sample showed the inverse trend with the increasing cycle number (Figure 23b). Thus, the S was improved after doing five ALD cycles of ZnO layer while that decreased after the same number of ALD cycles of SnO_2 layer, which can be attributed to difference of the Zn^{2+} ions and Sn^{4+} ions. The ALD-based interface engineering strategies were applied to improve the performance of TE materials which are summarized in Table 2.

It is worth noting that the coating layer may react with the core materials and form other phases during the pressing process. For instance, Zhang et al. coated a $\text{ZrNiSn}_{0.99}\text{Sb}_{0.01}$ composite with an Al_2O_3 layer and observed the formation of Zr vacancies and ZrO_2 nanoparticles during the SPS process.^[267] The combination of Zr and O formed ZrO_2 phases in the amorphous Al_2O_3 layer, which in turn caused the generation of Zr vacancies in the $\text{ZrNiSn}_{0.99}\text{Sb}_{0.01}$ matrix. Therefore, the synergetic influence of the Zr vacancies and the ZrO_2 phases optimized the carrier scattering performance, which resulted in the simultaneous enhancement of the S and σ . In a TiO_2 -coated $\text{Bi}_2\text{Te}_{2.7}\text{Se}_{0.3}$ system,^[266] Bi_2O_x and Te secondary phases appeared in the form of precipitates, indicating that a small amount of oxygen had occupied the Te sites. Apart from the second phases, high-density dislocation clusters were observed on the interfaces between the TiO_2 and $\text{Bi}_2\text{Te}_{2.7}\text{Se}_{0.3}$ molecules. The diffusion of Te atoms and ZnO/Te interfaces, which further contributed to phonon scattering, can be observed in the TEM image of the ZnO-coated $\text{Bi}_2\text{Te}_{2.7}\text{Se}_{0.3}$ system.^[264]

Although there are few studies in the literature discussing the effects of employing different precursor ligands on the core TE materials, the precursors should be meticulously selected to ensure that their reaction energy with the core materials will remain as low as possible during the coating process under high temperatures. Garcia et al. analyzed the chemical composition of core ET materials coated via PALD process with different precursors.^[269] The experimental results showed that the core material ($\gamma\text{-Fe}_2\text{O}_3$) was reduced to Fe_3O_4 after using tetrakis(dimethylamino)hafnium (TDMAHf) and tetrakis(dimethylamido)titanium (TDMATi) as precursors under a low process temperature (150 °C); however, no reduction was observed with TiCl_4 as a core material. Additionally, the reaction energy of reducing Fe_2O_3 to Fe_3O_4 exhibited different values when distinct ALD precursors were used. According

to the density functional theory (DFT) calculation results, the TDMAHf/TDMATi precursors can easily oxidize the core materials due to the low reaction energy. Thus, selecting the appropriate precursors is crucial for preventing the oxidation of specific core materials. Nevertheless, the discussed results demonstrated that ALD is a promising approach for modifying the interfaces of TE materials, with the aim of significantly improving their zT values.

3.2. Liquid Phase Methods

The high operating costs entailed in gas phase-based approaches (i.e., complex and expensive devices, use of gases and precursors) for the synthesis of thermoelectric core-shell nanoparticles can be mitigated by employing a variety of liquid phase-based synthesis methods (Table 3).^[270] In these strategies, either solid precursors are dissolved in suitable solvents or liquid precursors get in controlled contact with the core materials. These substrates can be nanowires, nano-dots, or nanoparticles in general. By using a colloidal-based synthesis approach, both the core and the shell are synthesized together in a single pot.^[271–273] The formation of the core is either achieved by reducing larger particles to the size of colloids (10^{-9} – 10^{-7} m), or via the condensation of smaller molecules. The shell thickness can be controlled by the precursor concentration^[274] and the pulsing time, that is, the duration of having the core material in contact with the liquid precursor.^[275] Additionally, in certain strategies, like precipitation- or hydrothermal-based methods, the pH value and temperature have an important influence on the shell thickness. Figure 24a illustrates the typical schematic setup of a solution-based process using a round-bottom flask under nitrogen flow to synthesize core-shell Cu–Cu₂O particles.^[276]

One of the primary advantages of solution-based over gas phase-based processes is that the precursors possessing very low vapor pressures can be used.^[277] Additionally, the functionalization of the core surface (also known as activation), or its protection or deprotection with organic functional groups, would be impossible (or very challenging) in gas phase thin film deposition-based methods, due to the fact that the amount of large and ionic species required for these processes cannot be brought into the gas phase.^[277]

Different liquid phase-based synthetic methods have been developed and improved over time, including

Table 3. Summary of references with related core–shell material synthesis methods.

Core	Shell	Method	zT	κ [Wm ⁻¹ K ⁻¹]	σ [S cm ⁻¹]	Ref.
C	PbTe	Hydrothermal	0.54 at 400 K	0.85 at 400 K	95 at 400 K	[281]
C	BCN	Wet-chemistry-assisted pretreatment and atmospheric-pressure carbothermal reaction	1.3 at 600 K	not available	12.4 at 573 K	[282]
Te	Bi/Bi ₂ Te ₃	Polymerization/precipitation	0.05 at 300 K	0.55 at 300 K	not available	[286]
TiO _y	TiC _{1-x} O _x	Anodization, sol-gel assisted	0.7 at 973 K	1.45 at 973 K	430 at 973 K	[284]
Bi _{0.5} Sb _{1.5} Te ₃	Cu	Electroless plating	>0.82 (avg over T)	0.25 at 371.5	1300 at 300 K	[285]
Ag ₂ Te	PANi	Precipitation/polymerization	2.09E-4 at 298 K	0.387 at 298 K	4.3 at 298 K	[287]
ATT/TiO ₂	PANi	In situ polymerization	0.006 at 300 K	not available	6.67 at 373 K	[288]
Au	Cu ₂ Se	Formation of functional groups by intermediate layer	0.61 at 723 K	0.8 at 723 K	not available	[286]
PbS	PbTe	Hydrothermal	not available	not available	35 at 600 K	[283]
Bi	Te	Colloidal synthesis with surface modification	0.2 at 300 K	0.8 at 200 K	not available	[272]
PbSe	PbSeTe	Solvothermal/precipitation (self-assembly)	not available	not available	not available	[289]
PbTe _x Se _{1-x}	PbSe	Solvothermal/precipitation (bottom-up assembly)	0.94 at 700 K	0.7 at 700 K	120 at 700 K	[290]
Te	TiS ₂	Solvothermal (core) + Physical vapor deposition (shell)	1.91 at 300 K	40 at 300 K	3.0E4 at 100 K	[254]
Bi ₂ Te ₃	Sb ₂ Te ₃	Solvothermal/ligand auxiliary solution process	not available	not available	792 at 300 K	[291]
Glass fiber	PbTe	Hot injection reaction/precipitation	0.75 at 400 K	0.226 at 400 K	172.4 at 400 K	[292]
PbTe	(PbS)	One-pot injection method (bottom-up assembly)	1.03 at 710 K ($x = 0.72$)	0.53 at 710 K ($x = 0.72$)	125.3 at 710 K ($x = 0.72$)	[271]
Bi ₂ Se ₃	Bi ₂ Te ₃	Solvothermal	0.71 at 450 K	0.38–0.40 at 300 K	220 at 300 K	[274]
PbTe	PbSe	Colloidal synthesis (temperature change, recrystallization)	0.35 at 570 K	1.6 at 300 K	800 at 300 K	[293]
PbTe	PbSe	Precipitation with surface modification (ligands)	not available	not available	≈110 at 700 K	[294]
Bi ₂ S ₃	Bi	Hydrothermal method	0.36 at 623 K	0.35 at 623 K	≈1000 at 623 K	[295]
PbTe	PDA:Ag	Hydrothermal/precipitation	1.3 at 723 K	not available	300 at 723 K	[296]
Cu	Cu ₂ O	Ligand-assisted solution phase method	0.61 at 723K	0.85 at 723 K	350 at 723 K	[276]

hydrothermal/solvothermal, precipitation-based, colloidal, or reduction-based synthesis, with all sharing the same core idea: to use the core TE material as a template for the controlled (and sometimes epitaxial) growth of the shell.

Hydrothermal synthesis is primarily used as a method to synthesize single crystals according to the following process: after removing the core material from an aqueous solution, it is deposited around a seed crystal and the desired crystal is slowly growing due to a temperature gradient. Therefore, this method is regarded as highly suitable for the synthesis of core–shell particles. Solvothermal synthesis shares the same core concept, except for the use of organic solvents instead of water. After being placed in a sealed autoclave (schematically illustrated in Figure 24a), the precursors, solvents, surfactants, and reduction agents react under high pressure/temperature conditions, while being exposed to microwave irradiation to accelerate the progress of the synthesis. Besides the synthesis of nanoparticles or core–shell particles, the hydrothermal method is also suitable for the surface functionalization of existing materials,^[274,278,279] with a prominent example being the control of the nanoparticles size (i.e., the nanoparticles get smaller as the volume and/or binding strength of the surface ligand increases).^[278]

A different approach for controlling the shell size of core–shell nanoparticles is regulating the precursor concentration in

the solution. Jin et al. used a hydrothermal route to synthesize Au–Cu₂Se core–shell nanoparticles with adjustable shell thicknesses in the range of 13–22 nm (cf. Figure 25a). Increasing the amount of Cu and Se precursors added to a fixed amount of Au nanoparticles causes the shell thickness to accordingly increase, thereby leading to a decreased thermal conductivity and increased zT value.^[280]

Liu et al. hydrothermally synthesized carbon spheres as a first step, and then let Pb²⁺ cations to adsorb on the surface by adding Pb(NO₃)₂.^[281] After adding NaHTe, Te²⁻ anions were adsorbed into the surface, generating a layer of PbTe around the carbon core in the process. By mixing a small weight percentage of C@PbTe particles into the PbSe matrix, they achieved a zT value of 0.54 at 400 K, which was a 13% improvement over the performance of the PbSe matrix alone.^[281] These results can be explained by the enhanced carrier scattering of the crystal lattice stemming from the increased temperature, which led to a decrease in electrical conductivity at rising temperatures. Parallely, the S was improved due to the reduction of carrier concentration combined with the energetic sharp resonance effects of the core–shell particles.^[281] Chiang et al. developed a two-step reaction route to produce C/BCN core–shell nanotubes, where they started with the dispersion of pre-synthesized CNTs, followed by the slow addition of B₂O₃ powder.^[282] The

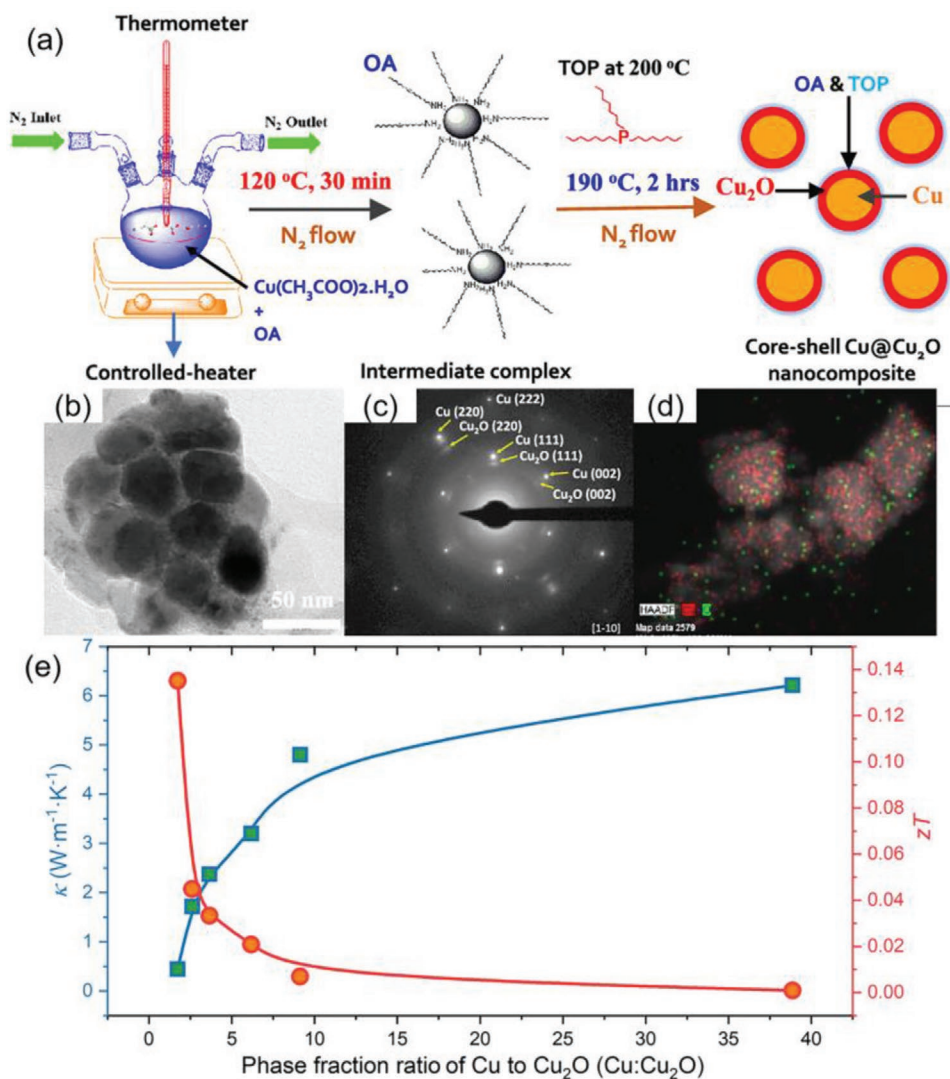


Figure 24. a) Schematic representation of the solution phase-based synthesis of core-shell Cu/Cu₂O nanocomposites; b–d) TEM analysis of core-shell Cu/Cu₂O nanocomposites with selected area diffraction (SAD) pattern and EDX mapping of the combined Cu and O species; e) Thermal conductivity (κ) and zT measurement curves against the phase fraction ratio of Cu:Cu₂O showing the increase in κ and decrease in zT with the increasing Cu content at 300 K.^[276] Reproduced with permission.^[276] Copyright 2020, American Chemical Society.

resulting paste was dried and then heated under an Argon and NH₃ flow environment (known as a carbothermic reaction). After removing excess boron/boron oxides by washing with hot water, followed by another drying step, they obtained C/BCN core-shell nanotubes with improved thermoelectric properties via B and N substitutional doping.^[282] The Seebeck coefficient was discovered to be three times larger than that of the parent CNTs, while the electrical conductivity was decreased, which enhanced the PF by 6.4 times. This was attributed to the formation of semiconducting junctions at the interfaces between the tubes, which originated from the selective BN-substitution in the outer shells, since the overall transport properties of CNT networks are limited by the carrier transmission at the CNT–CNT junctions.

The process through which a solved chemical substance reaches the solubility limit of the solution, as a result of the precipitating agents, pH, changes in temperature, and pres-

sure or polarity, is called precipitation. The phase changes from, for example, liquid to solid, renders this process suitable for layer growth around the core materials, especially when they act as seeds in the solution. By carefully controlling the precipitation, (nano)-particles with homogeneous size distribution or core-shell particles with conformally coated shells can be achieved. The condensation of small molecules within the solution causes the formation of colloidal particles, a process often termed as colloidal synthesis. Ultimately, the nanoparticles or core-shell particles can be obtained by a sedimentation process, for example, with the help of a centrifuge.

Sahu et al. synthesized several inorganic nanostructures (such as Te nanowires with and without ligands, CdSe nanocrystals, Bi₂S₃ nanoplatelets, Bi₂Te₃ nanowires, etc.) via a precipitation-based colloidal synthetic process which involved a surface functionalization step with sulfur and PEDOT:PSS (poly(3,4-ethylenedioxythiophene) polystyrene sulfonate).^[275]

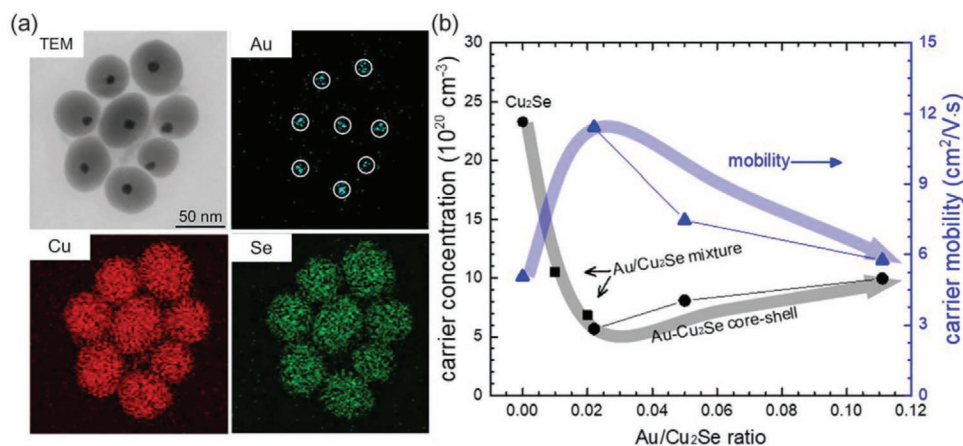


Figure 25. a) TEM images of as-prepared Au-Cu₂Se core-shell nanoparticles and the elemental mapping images of Au, Cu, Se; b) Au/Cu₂Se ratio dependence on carrier concentration (circular symbols) and mobility (triangle symbols). The filled square symbols indicate the carrier concentration of the Au/Cu₂Se mixture.^[280] Reproduced with permission.^[280] Copyright 2020, American Chemical Society.

Sulfur acted as a simple linker between the core surface and the polymer, that is, PEDOT:PSS, resulting in a robust composite. The synthesized core-shell structures demonstrated improved thermoelectric performance due to the different transport properties of the core and the shell.^[275] Interestingly, the enhancement in electrical conductivity was dependent on the Te-content in the hybrid film with PEDOT:PSS. The authors ascribed this effect to either a structural change in the polymer morphology, or a charge transfer between the inorganic nanowire and the PEDOT:PSS.^[275] Due to the incorporation of inorganic structures and the inherent differences between the transport mechanisms (i.e., polaronic/bipolaronic transport) in such hybrid materials, their thermal conductivity is very low, rendering them highly advantageous candidates for high performance TE materials.

Scheele et al. developed a novel synthesis method for near-monodispersed, sub-10 nm Bi₂Te₃ nanoparticles.^[272] By working under an inert atmosphere using standard Schlenck techniques, they mixed bismuth acetate with 1-dodecanethiol (which served as a surface functionalizing agent), eventually obtaining Bi-nanoparticles after several heating steps. By changing the amount of 1-dodecanethiol relative to the amount of stabilizing agent oleylamine, they accomplished the control of the nanoparticles size distribution. In a second step, a solution of tellurium in tetracyclophosphonic acid (TOP) was added to the as-prepared Bi-nanoparticles under stirring and heating, resulting in bismuth-tellurium alloy nanoparticles. Next, they heated the suspension to 110 °C for 18 h, resulting in the formation of Bi₂Te₃ nanoparticles. After a final washing and centrifugation step, which involved solvents like ethanol, chloroform, and hexane/hydrazine hydrate, they obtained a fine black powder. Although the electrical conductivity of the sintered pellets was nearly identical to that of the typical n-type bulk sample, the total thermal conductivity was as much as one order of magnitude smaller.

In another publication from Scheele et al. where a similar colloidal synthesis approach was used, the authors studied the thermoelectric properties of PbTe-PbSe core-shell nanoparticles.^[283] This time, lead acetate trihydrate was allowed to

slowly react with a solution of tellurium in TOP with the help of ligands like oleic acid, diphenylether, and oleylamine. The injection of a second solution containing lead acetate trihydrate and selenium in the TOP nanoparticles led to the formation of PbTe-PbSe-nanostars. Due to the thermally-induced alloying of the two chalcogenide phases, the material exhibited a p-type to n-type transformation, which resulted in a great improvement of its electrical transport properties. When the temperature rises, selenium, which is a good n-type dopant for PbTe, generates an increasing number of donor states close to the conduction band edge. Furthermore, the *S* value decreased, as a result of the holes and electrons counteracting each other and canceling their contribution to the overall thermopower. Ultimately, a maximum *zT* value of 0.35 at 570 K could be achieved.^[283]

When possessing electrical conductivity properties, nanoparticle cores can serve as electrodes and allow for a current to pass through an electrolyte, thereby leading to the transport of different (ionic) species to the surface of the core and, ultimately, deposition. This method can only be applied on electrically conductive cores, therefore limiting the possible core-shell combinations. Another disadvantage of this method is that the substrate shape influences the electrical resistance of the bath, which can lead to uneven current densities. Nevertheless, this method can improve several key parameters for achieving enhanced TE materials, as can be seen in the work by Ou et al. below.^[284]

Ou and co-workers pressed and annealed TiC_{1-x}O_x (*x* < 1) powders to yield porous pellets (preform). The powders were priorly prepared by a solid-state synthesis method. The pellets served as the anode, a silver disk as the cathode, and the electrolyte contained a phosphoric acid solution. After anodization at a certain voltage, the core-shell structure of TiC_{1-x}O_x@TiO_y (*x* < 1, 1 < *y* < 2) was obtained, which demonstrated a reduced electrical conductivity, higher Seebeck coefficient, and a higher PF.^[284] The created double-barrier effectively blocked the low-energy carriers, resulting in a decreased electrical conductivity and increase in the *S* value. At the same time, a low thermal conductivity was measured, which the authors ascribed to the

increased number of scattering centers against phonons due to the heterostructured interfaces.

Compared to the anodization process described before, this method offers the possibility to achieve the electroless plating of non-conductive materials, as well. The process requires a catalyst (which can be the substrate itself) and the reaction must be autocatalytic. This ensures the continuation of the process after the substrate is coated. The reaction is based on the chemical reduction of metal cations in a liquid solution and can be described by the general formula in Equation (7):



with M representing the metal with charge z , X representing the reducing agent, and Z is an oxidized byproduct. Huang et al. utilized the electroless plating method to prepare n-type Bi₂Te₃/Cu composites. By adjusting the pH value with sodium hydrate in a plating solution containing copper sulfate, they coated Bi₂Te₃-particles with a thin layer of metallic copper. The coating accomplished the scattering of the charge carriers, thereby improving both the electrical conductivity and the power factor. Most importantly, they achieved the highest zT value reported thus far for a copper-coated sample of nearly 1.1 at 372 K.^[285]

3.3. Opportunities and Challenges in Continuous Interface Modification

In this part, we summarize recent advances on synergistic improvement of TE performance via gas phase and wet chemical approaches, demonstrating that continuous interface modification is a viable method for improving TE performance. All of these researches are concerned with the decoupling optimization of three TE parameters utilizing submicrometric scale composition or microstructure refinement. However, as an emerging approach, there is still more work to be done to shed light on many unanswered topics.

- 1) The effect of grain boundary composition/microstructure and grain size on carrier/phonon transportation behavior should be thoroughly investigated in the continuous interface modification approaches.
- 2) Furthermore, the effect of the chemical composition of the precursors used in ALD or CVD processes in terms of residual impurities such as C, H, O, Cl, and so on in the final coated phases should be carefully examined since they may have a detrimental impact on the TE performances.
- 3) The amount of inorganic/organic impurities in the wet chemical process is rarely mentioned. During the high-temperature pressing process, remaining impurities may vaporize and produce holes in the matrix, which is unfavorable to electrical characteristics. It is still unclear how to totally eliminate the contaminant.

4. Summary and Outlook

The increasing interest in thermoelectric materials stems from the global need for renewable resources and the scaling-

up of manufacturing processes. Recent advancements in the field have progressed the mass production of conventional TE materials, such as Bi₂Te₃, half-Heuslers, skutterudites, PbTe, silicides, etc. Using advanced computational techniques, a plethora of promising TE materials with remarkable thermoelectric efficiency, such as Cu₂Se, GeTe, and SnSe, were engineered and synthesized, demonstrating maximum potential for applications in practical devices. However, several complications arise in the design and synthesis of new TE materials, as well as in the modification of existing ones. For example, the inevitable discrepancy between the nominal and the actual composition of synthesized materials, caused by the inadequate integration or segregation of the constituents, results in thermoelectric properties loss (as compared to engineered materials). In addition, for certain small-scale thermoelectric systems (e.g., Cu₂Se, SnSe, and GeTe), vacancy configuration is feasible. Furthermore, the precise monitoring of the desired dopant quantities and their excessive solubilities, combined with their homogeneous distribution across the matrix, results in precipitates that can degrade the thermoelectric efficiency of the core TE material. Aside from the above hindrances, other well-known difficulties in the synthesis of nanostructured TE materials with exceptional features is the anisotropy of thin films and certain bulk materials in terms of thermoelectric performance, as well as their severely poor mechanical properties. By employing discontinuous and continuous modification techniques on the nanostructure of certain TE material systems, we can attain beneficial changes in their electronic properties while maintaining a low κ (via broad-interface phonon scattering), ultimately achieving significantly improved PF and zT values. The interface modification approach is simple, cost-effective, and suitable for scale-up manufacturing. Furthermore, interfacial adjustment methods are scalable and adaptable in terms of fine-tuning a TE material's composition, microstructure, and final efficiency. In theory, surface modification through ball-milling, gas-phase synthesis, and (wet) chemical routes can be applied to a wide range of TE materials. As a result, several options and variations are offered for choosing the appropriate second phase and TE matrix. In this review, we summarized the current state-of-the-art pertaining to the interface/surface modification of TE materials, including all reported enhancements of their thermoelectric behavior, as well as the fundamental mechanisms underlying these phenomena. The following are the major insights and perspectives derived from our work concerning the progress of interface/surface modification techniques for TE materials:

- 1) To avoid the solubility of one phase into the other, the constituent phases (TE matrix and second phase) should be chemically, environmentally, and thermally stable, so that the microstructure does not alter during the synthesis and operation processes.
- 2) For interface modification, the homogeneous dispersion or coating of the second phase is required. To ensure a reproducible stoichiometry, it is critical to avoid agglomeration during the fabrication process for low-dimensionality materials or materials with diameters in the nano range.
- 3) It is crucial to maintain a consistent grain size. Grain growth may result from high-temperature annealing or holding for

an extended period of time. Faster annealing techniques, such as (pulsed) SPS and rapid thermal annealing, are required to effectively control the grain size and/or inhibit grain growth.

- 4) To enable the scattering of the low-energy charge carriers, an appropriate interfacial barrier or band bending technique is required, indicating that an appropriate second phase should be selected. Furthermore, the barrier height should be properly tuned to maintain or improve mobility, and the work function of the incorporated phase should be close to that of the base material.
- 5) Regarding the thermal properties, the thermal conductivity of the second phase should be less than that of the matrix; otherwise, more thermal conductive paths will be formed, potentially increasing the total thermal conductivity.
- 6) The majority of interface modifications techniques reported thus far are based on single components or structures derived from the second phase. A hierarchical heterostructure has rarely been investigated in terms of thermoelectric behavior, leaving plenty of room for further optimizing the overall performance of TE materials.

We hope that this review will aid researchers in the field to design better and novel TE inorganic materials with enhanced performance via interface/surface modification techniques.

Acknowledgements

A.B. acknowledges the Alexander von Humboldt-Stiftung for the Postdoctoral Research Fellow funding. The authors acknowledge Prof. Jun Luo from Shanghai University, Dr. Nicolas Pérez Rodríguez and Dr. Ran He from IFW-Dresden for their valuable comments. Special thanks to Ronald Uhlemann for the preparation of the illustrations.

Open access funding enabled and organized by Projekt DEAL.

Conflict of Interest

The authors declare no conflict of interest.

Keywords

artificial decoration, charger carrier scattering, core-shell structure, interface modification, surface modification, thermal conductivity suppression, thermoelectric materials

Received: June 18, 2021

Revised: July 29, 2021

Published online: August 16, 2021

- [1] A. Bahrami, G. Schierning, K. Nielsch, *Adv. Energy Mater.* **2020**, *10*, 1904159.
- [2] J. Luo, S. He, Z. Li, Y. Li, F. Wang, J. Zhang, *J. Inorg. Mater.* **2019**, *34*, 247.
- [3] X. Qi, J. Chen, K. Guo, S. He, J. Yang, Z. Li, J. Xing, J. Hu, H. Luo, W. Zhang, J. Luo, *Chem. Eng. J.* **2019**, *374*, 494.
- [4] S. He, Y. Li, L. Liu, Y. Jiang, J. Feng, W. Zhu, J. Zhang, Z. Dong, Y. Deng, J. Luo, W. Zhang, G. Chen, *Sci. Adv.* **2020**, *6*, eaaz8423.

- [5] R. He, G. Schierning, K. Nielsch, *Adv. Mater. Technol.* **2018**, *3*, 1700256.
- [6] D. Ding, C. Lu, Z. Tang, *Adv. Mater. Interfaces* **2017**, *4*, 1700517.
- [7] S. He, Y. Yang, Z. Li, J. Zhang, C. Wang, W. Zhang, J. Luo, *Sci. China Mater.* **2021**, *64*, 1751.
- [8] G. Tan, L.-D. Zhao, M. G. Kanatzidis, *Chem. Rev.* **2016**, *116*, 12123.
- [9] T. Zhu, L. Hu, X. Zhao, J. He, *Adv. Sci.* **2016**, *3*, 1600004.
- [10] J. Li, S. Zhang, F. Jia, S. Zheng, X. Shi, D. Jiang, S. Wang, G. Lu, L. Wu, Z.-G. Chen, *Mater. Today Phys.* **2020**, *15*, 100269.
- [11] L. Hu, T. Zhu, X. Liu, X. Zhao, *Adv. Funct. Mater.* **2014**, *24*, 5211.
- [12] Z. Jian, Z. Chen, W. Li, J. Yang, W. Zhang, Y. Pei, *J. Mater. Chem. C* **2015**, *3*, 12410.
- [13] C. Fu, T. Zhu, Y. Liu, H. Xie, X. Zhao, *Energy Environ. Sci.* **2015**, *8*, 216.
- [14] Y. Pei, H. Wang, G. J. Snyder, *Adv. Mater.* **2012**, *24*, 6125.
- [15] J. Jiang, L. Chen, S. Bai, Q. Yao, Q. Wang, *Mater. Sci. Eng., B* **2005**, *117*, 334.
- [16] J. Qiu, Y. Yan, T. Luo, K. Tang, L. Yao, J. Zhang, M. Zhang, X. Su, G. Tan, H. Xie, M. G. Kanatzidis, C. Uher, X. Tang, *Energy Environ. Sci.* **2019**, *12*, 3106.
- [17] S. R. Popuri, M. Pollet, R. Decourt, F. D. Morrison, N. S. Bennett, J. W. G. Bos, *J. Mater. Chem. C* **2016**, *4*, 1685.
- [18] Z. Liang, M. J. Boland, K. Butrouna, D. R. Strachan, K. R. Graham, *J. Mater. Chem. A* **2017**, *5*, 15891.
- [19] A. Soni, Y. Shen, M. Yin, Y. Zhao, L. Yu, X. Hu, Z. Dong, K. A. Khor, M. S. Dresselhaus, Q. Xiong, *Nano Lett.* **2012**, *12*, 4305.
- [20] A. Pakdel, Q. Guo, V. Nicolosi, T. Mori, *J. Mater. Chem. A* **2018**, *6*, 21341.
- [21] Y. Lan, A. J. Minnich, G. Chen, Z. Ren, *Adv. Funct. Mater.* **2010**, *20*, 357.
- [22] S. K. Bux, R. G. Blair, P. K. Gogna, H. Lee, G. Chen, M. S. Dresselhaus, R. B. Kaner, J.-P. Fleurial, *Adv. Funct. Mater.* **2009**, *19*, 2445.
- [23] G. Tan, L.-D. Zhao, F. Shi, J. W. Doak, S.-H. Lo, H. Sun, C. Wolverton, V. P. Dravid, C. Uher, M. G. Kanatzidis, *J. Am. Chem. Soc.* **2014**, *136*, 7006.
- [24] H. Liu, X. Zhang, J. Li, Z. Bu, X. Meng, R. Ang, W. Li, *ACS Appl. Mater. Interfaces* **2019**, *11*, 30756.
- [25] H. Wang, G. Luo, C. Tan, C. Xiong, Z. Guo, Y. Yin, B. Yu, Y. Xiao, H. Hu, G. Liu, X. Tan, J. G. Noudem, J. Jiang, *ACS Appl. Mater. Interfaces* **2020**, *12*, 31612.
- [26] J. S. Yoon, J. M. Song, J. U. Rahman, S. Lee, W. S. Seo, K. H. Lee, S. Kim, H.-S. Kim, S. Kim, W. H. Shin, *Acta Mater.* **2018**, *158*, 289.
- [27] K. Ahmad, C. Wan, P. Zong, *J. Mater. Sci. Mater. Electron.* **2019**, *30*, 11923.
- [28] X. Ji, J. He, Z. Su, N. Gothard, T. M. Tritt, *J. Appl. Phys.* **2008**, *104*, 034907.
- [29] M. Ibáñez, A. Genç, R. Hasler, Y. Liu, O. Dobrozhan, O. Nazarenko, M. de la Mata, J. Arbiol, A. Cabot, M. V. Kovalenko, *ACS Nano* **2019**, *13*, 6572.
- [30] W. Li, S. Lin, B. Ge, J. Yang, W. Zhang, Y. Pei, *Adv. Sci.* **2016**, *3*, 1600196.
- [31] B. Jiang, P. Qiu, E. Eikeland, H. Chen, Q. Song, D. Ren, T. Zhang, J. Yang, B. B. Iversen, X. Shi, L. Chen, *J. Mater. Chem. C* **2017**, *5*, 943.
- [32] B. Jiang, P. Qiu, H. Chen, Q. Zhang, K. Zhao, D. Ren, X. Shi, L. Chen, *Chem. Commun.* **2017**, *53*, 11658.
- [33] Y. Pei, J. Lensch-Falk, E. S. Toberer, D. L. Medlin, G. J. Snyder, *Adv. Funct. Mater.* **2011**, *21*, 241.
- [34] J. P. Heremans, V. Jovovic, E. S. Toberer, A. Saramat, K. Kurosaki, A. Charoensakdee, S. Yamanaka, G. J. Snyder, *Science* **2008**, *321*, 554.
- [35] Y. Pei, A. LaLonde, S. Iwanaga, G. J. Snyder, *Energy Environ. Sci.* **2011**, *4*, 2085.

- [36] L.-D. Zhao, C. Chang, G. Tan, M. G. Kanatzidis, *Energy Environ. Sci.* **2016**, *9*, 3044.
- [37] L.-D. Zhao, S.-H. Lo, Y. Zhang, H. Sun, G. Tan, C. Uher, C. Wolverton, V. P. Dravid, M. G. Kanatzidis, *Nature* **2014**, *508*, 373.
- [38] M. R. Burton, S. Mehraban, D. Beynon, J. McGettrick, T. Watson, N. P. Lavery, M. J. Carnie, *Adv. Energy Mater.* **2019**, *9*, 1900201.
- [39] L. Yang, Z.-G. Chen, G. Han, M. Hong, Y. Zou, J. Zou, *Nano Energy* **2015**, *16*, 367.
- [40] D. Yang, X. Su, J. Li, H. Bai, S. Wang, Z. Li, H. Tang, K. Tang, T. Luo, Y. Yan, J. Wu, J. Yang, Q. Zhang, C. Uher, M. G. Kanatzidis, X. Tang, *Adv. Mater.* **2020**, *32*, 2003730.
- [41] W.-W. Liao, L. Yang, J. Chen, D.-L. Zhou, X. Qu, K. Zheng, G. Han, J.-B. Zhou, M. Hong, Z.-G. Chen, *Chem. Eng. J.* **2019**, *371*, 593.
- [42] D. Bao, J. Chen, Y. Yu, W. Liu, L. Huang, G. Han, J. Tang, D. Zhou, L. Yang, Z.-G. Chen, *Chem. Eng. J.* **2020**, *388*, 124295.
- [43] B. Chen, S. R. Das, W. Zheng, B. Zhu, B. Xu, S. Hong, C. Sun, X. Wang, Y. Wu, J. C. Claussen, *Adv. Electron. Mater.* **2017**, *3*, 1600524.
- [44] T. He, J. Chen, H. D. Rosenfeld, M. A. Subramanian, *Chem. Mater.* **2006**, *18*, 759.
- [45] B. C. Sales, D. Mandrus, R. K. Williams, *Science* **1996**, *272*, 1325.
- [46] X. Shi, J. Yang, J. R. Salvador, M. Chi, J. Y. Cho, H. Wang, S. Bai, J. Yang, W. Zhang, L. Chen, *J. Am. Chem. Soc.* **2011**, *133*, 7837.
- [47] J. Mao, Y. Wu, S. Song, Q. Zhu, J. Shuai, Z. Liu, Y. Pei, Z. Ren, *ACS Energy Lett.* **2017**, *2*, 2245.
- [48] F. Meng, S. Sun, J. Ma, C. Chronister, J. He, W. Li, *Mater. Today Phys.* **2020**, *13*, 100217.
- [49] J. Mao, J. Shuai, S. Song, Y. Wu, R. Dally, J. Zhou, Z. Liu, J. Sun, Q. Zhang, C. dela Cruz, S. Wilson, Y. Pei, D. J. Singh, G. Chen, C.-W. Chu, Z. Ren, *Proc. Natl. Acad. Sci. U. S. A.* **2017**, *114*, 10548.
- [50] R. He, T. Zhu, Y. Wang, U. Wolff, J.-C. Jaud, A. Sotnikov, P. Potapov, D. Wolf, P. Ying, M. Wood, Z. Liu, L. Feng, N. P. Rodriguez, G. J. Snyder, J. C. Grossman, K. Nielsch, G. Schierning, *Energy Environ. Sci.* **2020**, *13*, 5165.
- [51] C. Fu, S. Bai, Y. Liu, Y. Tang, L. Chen, X. Zhao, T. Zhu, *Nat. Commun.* **2015**, *6*, 8144.
- [52] J. K. Carson, S. J. Lovatt, D. J. Tanner, A. C. Cleland, *Int. J. Heat Mass Transfer* **2005**, *48*, 2150.
- [53] X.-L. Shi, J. Zou, Z.-G. Chen, *Chem. Rev.* **2020**, *120*, 7399.
- [54] Z.-G. Chen, X. Shi, L.-D. Zhao, J. Zou, *Prog. Mater. Sci.* **2018**, *97*, 283.
- [55] C. Gayner, Y. Amouyal, *Adv. Funct. Mater.* **2020**, *30*, 1901789.
- [56] D.-K. Ko, Y. Kang, C. B. Murray, *Nano Lett.* **2011**, *11*, 2841.
- [57] T. H. Zou, X. Y. Qin, D. Li, B. J. Ren, G. L. Sun, Y. C. Dou, Y. Y. Li, L. L. Li, J. Zhang, H. X. Xin, *J. Appl. Phys.* **2014**, *115*, 053710.
- [58] Y. Lin, M. Wood, K. Imasato, J. J. Kuo, D. Lam, A. N. Mortazavi, T. J. Slade, S. A. Hodge, K. Xi, M. G. Kanatzidis, D. R. Clarke, M. C. Hersam, G. J. Snyder, *Energy Environ. Sci.* **2020**, *13*, 4114.
- [59] Y. Zheng, Y. Luo, C. Du, B. Zhu, Q. Liang, H. H. Hng, K. Hippalgaonkar, J. Xu, Q. Yan, *Mater. Chem. Front.* **2017**, *1*, 2457.
- [60] H. Jin, J. Li, J. Iocozzia, X. Zeng, P. Wei, C. Yang, N. Li, Z. Liu, J. H. He, T. Zhu, J. Wang, Z. Lin, S. Wang, *Angew. Chem., Int. Ed.* **2019**, *58*, 15206.
- [61] S. H. Zaferani, R. Ghomashchi, D. Vashae, *ACS Appl. Energy Mater.* **2021**, *4*, 3573.
- [62] S. V. Faleev, F. Léonard, *Phys. Rev. B* **2008**, *77*, 214304.
- [63] D. Narducci, E. Selezneva, G. Cerofolini, S. Frabboni, G. Ottaviani, *J. Solid State Chem.* **2012**, *193*, 19.
- [64] J. Bardeen, *Phys. Rev.* **1947**, *71*, 717.
- [65] E. Lee, J. Ko, J.-Y. Kim, W.-S. Seo, S.-M. Choi, K. H. Lee, W. Shim, W. Lee, *J. Mater. Chem. C* **2016**, *4*, 1313.
- [66] A. Popescu, L. M. Woods, J. Martin, G. S. Nolas, *Phys. Rev. B* **2009**, *79*, 205302.
- [67] S. Sumithra, N. J. Takas, D. K. Misra, W. M. Nolting, P. F. P. Poudeu, K. L. Stokes, *Adv. Energy Mater.* **2011**, *1*, 1141.
- [68] J. K. Nagle, *J. Am. Chem. Soc.* **1990**, *112*, 4741.
- [69] Q. Zhang, X. Ai, L. Wang, Y. Chang, W. Luo, W. Jiang, L. Chen, *Adv. Funct. Mater.* **2015**, *25*, 966.
- [70] M. Koirala, H. Zhao, M. Pokharel, S. Chen, T. Dahal, C. Opeil, G. Chen, Z. Ren, *Appl. Phys. Lett.* **2013**, *102*, 213111.
- [71] Y. Pei, X. Shi, A. Lalonde, H. Wang, L. Chen, G. J. Snyder, *Nature* **2011**, *473*, 66.
- [72] Q. Zhang, F. Cao, W. Liu, K. Lukas, B. Yu, S. Chen, C. Opeil, D. Broido, G. Chen, Z. Ren, *J. Am. Chem. Soc.* **2012**, *134*, 10031.
- [73] B. Yu, M. Zebarjadi, H. Wang, K. Lukas, H. Wang, D. Wang, C. Opeil, M. Dresselhaus, G. Chen, Z. Ren, *Nano Lett.* **2012**, *12*, 2077.
- [74] M. Zebarjadi, G. Joshi, G. Zhu, B. Yu, A. Minnich, Y. Lan, X. Wang, M. Dresselhaus, Z. Ren, G. Chen, *Nano Lett.* **2011**, *11*, 2225.
- [75] W. Zhu, W. Hu, P. Wei, X. Nie, W. Zhao, *J. Electron. Mater.* **2020**, *49*, 2962.
- [76] X. Lu, Q. Zheng, S. Gu, R. Guo, L. Su, J. Wang, Z. Zhou, Y. Fan, W. Jiang, L. Wang, *Chin. Chem. Lett.* **2020**, *31*, 880.
- [77] Y. Guo, C. Dun, J. Xu, P. Li, W. Huang, J. Mu, C. Hou, C. A. Hewitt, Q. Zhang, Y. Li, D. L. Carroll, H. Wang, *ACS Appl. Mater. Interfaces* **2018**, *10*, 33316.
- [78] L. Dyadyusha, H. Yin, S. Jaiswal, T. Brown, J. J. Baumberg, F. P. Booy, T. Melvin, *Chem. Commun.* **2005**, *25*, 3201.
- [79] S. Chung, R. A. Revia, M. Zhang, *Adv. Mater.* **2019**, *33*, 1904362.
- [80] Y. Wang, R. Hu, G. Lin, I. Roy, K.-T. Yong, *ACS Appl. Mater. Interfaces* **2013**, *5*, 2786.
- [81] G. S. Selopal, H. Zhao, Z. M. Wang, F. Rosei, *Adv. Funct. Mater.* **2020**, *30*, 2070086.
- [82] S. Ermin, S. P. Singh, L. Han, N. Satoh, A. Islam, *Sol. Energy* **2011**, *85*, 1264.
- [83] X. Yang, K. Wang, Y. Gu, H. Ni, X. Wang, T. Yang, Z. Wang, *Sol. Energy Mater. Sol. Cells* **2013**, *113*, 144.
- [84] Q. Sun, Y. A. Wang, L. S. Li, D. Wang, T. Zhu, J. Xu, C. Yang, Y. Li, *Nat. Photonics* **2007**, *1*, 717.
- [85] Z. Shi, Y. Li, Y. Zhang, Y. Chen, X. Li, D. Wu, T. Xu, C. Shan, G. Du, *Nano Lett.* **2017**, *17*, 313.
- [86] X. Dai, Z. Zhang, Y. Jin, Y. Niu, H. Cao, X. Liang, L. Chen, J. Wang, X. Peng, *Nature* **2014**, *515*, 96.
- [87] L. Cui, C. Li, B. Tang, C. Zhang, *Analyst* **2018**, *143*, 2469.
- [88] M. Zebarjadi, K. Esfarjani, A. Shakouri, J.-H. Bahk, Z. Bian, G. Zeng, J. Bowers, H. Lu, J. Zide, A. Gossard, *Appl. Phys. Lett.* **2009**, *94*, 202105.
- [89] S. Kabi, A. G. U. Perera, *J. Appl. Phys.* **2015**, *117*, 124303.
- [90] J. Zhou, R. Yang, *J. Appl. Phys.* **2011**, *110*, 084317.
- [91] W. Zheng, Y. Luo, Y. Liu, J. Shi, R. Xiong, Z. Wang, *J. Phys. Chem. Lett.* **2019**, *10*, 4903.
- [92] Q. Wang, S. Song, X. Yang, Z. Liu, Y. Ma, X. San, J. Wang, D. Zhang, S.-F. Wang, Z. Li, *J. Mater.* **2021**, *7*, 377.
- [93] Tarachand, B. Mukherjee, M. Saxena, Y.-K. Kuo, G. S. Okram, S. Dam, S. Hussain, A. Lakhani, U. Deshpande, T. Shripathi, *ACS Appl. Energy Mater.* **2019**, *2*, 6383.
- [94] W. Zhao, Z. Liu, Z. Sun, Q. Zhang, P. Wei, X. Mu, H. Zhou, C. Li, S. Ma, D. He, P. Ji, W. Zhu, X. Nie, X. Su, X. Tang, B. Shen, X. Dong, J. Yang, Y. Liu, J. Shi, *Nature* **2017**, *549*, 247.
- [95] Y. Zheng, T. Lu, M. M. H. Polash, M. Rasoulianboroujeni, N. Liu, M. E. Manley, Y. Deng, P. J. Sun, X. L. Chen, R. P. Hermann, D. Vashae, J. P. Heremans, H. Zhao, *Sci. Adv.* **2019**, *5*, eaat9461.
- [96] Z. Wei, C. Wang, J. Zhang, J. Yang, Z. Li, Q. Zhang, P. Luo, W. Zhang, E. Liu, J. Luo, *ACS Appl. Mater. Interfaces* **2020**, *12*, 20653.
- [97] Q. Wen, C. Chang, L. Pan, X. Li, T. Yang, H. Guo, Z. Wang, J. Zhang, F. Xu, Z. Zhang, G. Tang, *J. Mater. Chem. A* **2017**, *5*, 13392.

- [98] B. Du, X. Lai, Q. Liu, H. Liu, J. Wu, J. Liu, Z. Zhang, Y. Pei, H. Zhao, J. Jian, *ACS Appl. Mater. Interfaces* **2019**, *11*, 31816.
- [99] R. Lu, J. S. Lopez, Y. Liu, T. P. Bailey, A. A. Page, S. Wang, C. Uher, P. F. P. Poudeu, *J. Mater. Chem. A* **2019**, *7*, 11095.
- [100] L. Fu, J. Yang, J. Peng, Q. Jiang, Y. Xiao, Y. Luo, D. Zhang, Z. Zhou, M. Zhang, Y. Cheng, F. Cheng, *J. Mater. Chem. A* **2015**, *3*, 1010.
- [101] G. Kim, H. S. Kim, H. S. Lee, J. Kim, K. H. Lee, J. W. Roh, W. Lee, *Nano Energy* **2020**, *72*, 104698.
- [102] C. C. Zhao, C. Xiao, *Rare Met.* **2021**, *40*, 752.
- [103] C. P. Bean, J. D. Livingston, *J. Appl. Phys.* **1959**, *30*, S120.
- [104] M. Yaprıntsev, A. Vasil'ev, O. Ivanov, M. Zhezhu, E. Yaprıntseva, V. Novikov, *Scr. Mater.* **2021**, *194*, 113710.
- [105] F. Kong, J. Bai, Y. Zhao, Y. Liu, J. Shi, Z. Wang, R. Xiong, *Appl. Phys. Lett.* **2019**, *115*, 203901.
- [106] R. M. Costescu, *Science* **2004**, *303*, 989.
- [107] K. T. Kim, G. H. Ha, *J. Nanomater.* **2013**, *2013*, 821657.
- [108] C.-F. Wu, T.-R. Wei, F.-H. Sun, J.-F. Li, *Adv. Sci.* **2017**, *4*, 1700199.
- [109] D. Zhao, M. Zuo, Z. Wang, X. Teng, H. Geng, *J. Nanosci. Nanotechnol.* **2015**, *15*, 3076.
- [110] X. Y. Huang, Z. Xu, L. D. Chen, *Solid State Commun.* **2004**, *130*, 181.
- [111] Y. Xiao, J. Yang, Q. Jiang, L. Fu, Y. Luo, D. Zhang, Z. Zhou, *J. Electron. Mater.* **2016**, *45*, 1266.
- [112] X. Du, R. Shi, Y. Ma, F. Cai, X. Wang, Z. Yuan, *RSC Adv.* **2015**, *5*, 31004.
- [113] M. Ito, T. Tada, S. Katsuyama, *J. Alloys Compd.* **2003**, *350*, 296.
- [114] J. Ning, D. Wu, D. Zhao, *Appl. Sci.* **2017**, *7*, 1043.
- [115] L. Zou, B. P. Zhang, Z. H. Ge, C. Gao, D. B. Zhang, Y. C. Liu, *Phys. Status Solidi A* **2013**, *210*, 2550.
- [116] Y.-X. Yang, Y.-H. Wu, Q. Zhang, G.-S. Cao, T.-J. Zhu, X.-B. Zhao, *Rare Met.* **2020**, *39*, 887.
- [117] S. Fiameni, A. Famengo, S. Boldrini, S. Battiston, M. Saleemi, M. Stingaciu, M. Jhonsson, S. Barison, M. Fabrizio, *J. Electron. Mater.* **2013**, *42*, 2062.
- [118] N. Nandihalli, Q. Guo, S. Gorsse, A. U. Khan, T. Mori, H. Kleinke, *Eur. J. Inorg. Chem.* **2016**, *2016*, 853.
- [119] Z. Zhou, J. Yang, Q. Jiang, D. Zhang, J. Xin, X. Li, Y. Ren, X. He, *J. Am. Ceram. Soc.* **2017**, *100*, 5723.
- [120] Z. He, C. Stiewe, D. Platzek, G. Karpinski, E. Müller, S. Li, M. Toprak, M. Muhammed, *Nanotechnology* **2007**, *18*, 235602.
- [121] Y. Zhu, H. Shen, H. Chen, *Rare Met.* **2012**, *31*, 43.
- [122] C. Chubilleau, B. Lenoir, C. Candolfi, P. Masschelein, A. Dauscher, E. Guilmeau, C. Godart, *J. Alloys Compd.* **2014**, *589*, 513.
- [123] T.-H. Liu, J. Zhou, M. Li, Z. Ding, Q. Song, B. Liao, L. Fu, G. Chen, *Proc. Natl. Acad. Sci. U. S. A.* **2018**, *115*, 879.
- [124] B. Madavali, H.-S. Kim, K.-H. Lee, S.-J. Hong, *Intermetallics* **2017**, *82*, 68.
- [125] B. Madavali, H. S. Kim, K. H. Lee, S. J. Hong, *J. Appl. Phys.* **2017**, *121*, 225104.
- [126] W. Zhao, Z. Liu, P. Wei, Q. Zhang, W. Zhu, X. Su, X. Tang, J. Yang, Y. Liu, J. Shi, Y. Chao, S. Lin, Y. Pei, *Nat. Nanotechnol.* **2017**, *12*, 55.
- [127] Z. Jiang, H. Ming, X. Qin, D. Feng, J. Zhang, C. Song, D. Li, H. Xin, J. Li, J. He, *ACS Appl. Mater. Interfaces* **2020**, *12*, 46181.
- [128] F. Shi, C. Tan, H. Wang, X. Tan, Y. Yin, B. Yu, J. Cai, C. Xiong, G. Liu, J. Jiang, *ACS Appl. Mater. Interfaces* **2020**, *12*, 52922.
- [129] X.-Y. Wang, H.-J. Wang, B. Xiang, L.-W. Fu, H. Zhu, D. Chai, B. Zhu, Y. Yu, N. Gao, Z.-Y. Huang, F.-Q. Zu, *ACS Appl. Mater. Interfaces* **2018**, *10*, 23277.
- [130] Y.-X. Chen, X.-L. Shi, Z.-H. Zheng, F. Li, W.-D. Liu, W.-Y. Chen, X.-R. Li, G.-X. Liang, J.-T. Luo, P. Fan, Z.-G. Chen, *Mater. Today Phys.* **2021**, *16*, 100306.
- [131] J. Li, Q. Tan, J.-F. Li, D.-W. Liu, F. Li, Z.-Y. Li, M. Zou, K. Wang, *Adv. Funct. Mater.* **2013**, *23*, 4317.
- [132] L. R. Macario, Y. Shi, P. Jafarzadeh, T. Zou, J. B. Kycia, H. Kleinke, *ACS Appl. Mater. Interfaces* **2019**, *11*, 45629.
- [133] Z.-Y. Li, J.-F. Li, W.-Y. Zhao, Q. Tan, T.-R. Wei, C.-F. Wu, Z.-B. Xing, *Appl. Phys. Lett.* **2014**, *104*, 113905.
- [134] R. Inoue, J. Nakano, T. Nakamura, T. Ube, T. Iida, Y. Kogo, *J. Alloys Compd.* **2019**, *775*, 657.
- [135] Z.-B. Xing, J.-F. Li, *J. Alloys Compd.* **2016**, *687*, 246.
- [136] T. Wang, H. Wang, W. Su, J. Zhai, G. Yakovleva, X. Wang, T. Chen, A. Romanenko, C. Wang, *J. Mater. Chem. C* **2020**, *8*, 7393.
- [137] D.-W. Liu, J.-F. Li, C. Chen, B.-P. Zhang, *J. Electron. Mater.* **2011**, *40*, 992.
- [138] P. Qin, Z.-H. Ge, J. Feng, *J. Alloys Compd.* **2017**, *696*, 782.
- [139] S. Bathula, M. Jayasimhadri, B. Gahtori, A. Kumar, A. K. Srivastava, A. Dhar, *Phys. Chem. Chem. Phys.* **2017**, *19*, 25180.
- [140] Z. Zhou, J. Li, Y. Fan, Q. Zhang, X. Lu, S. Fan, K. Kikuchi, N. Nomura, A. Kawasaki, L. Wang, W. Jiang, *Scr. Mater.* **2019**, *162*, 166.
- [141] J.-F. Li, J. Liu, *Phys. Status Solidi* **2006**, *203*, 3768.
- [142] C. Ruan, H. Song, M. Fan, H. Hao, S. Liu, *Ceram. Int.* **2021**, *47*, 6548.
- [143] H. Qin, B. Cui, W. Wang, S. Sun, D. Qin, M. Guo, L. Xie, F. Guo, W. Cai, J. Sui, *Adv. Electron. Mater.* **2021**, *7*, 2100173.
- [144] L. Wang, J. Li, Y. Xie, L. Hu, F. Liu, W. Ao, J. Luo, C. Zhang, *Mater. Today Phys.* **2021**, *16*, 100308.
- [145] W. Pengfei, Z. Pengcheng, D. Shijie, D. Bo, L. Yao, *J. Electron. Mater.* **2017**, *46*, 2807.
- [146] B. Duan, P. Zhai, P. Wen, S. Zhang, L. Liu, Q. Zhang, *Scr. Mater.* **2012**, *67*, 372.
- [147] G. Yang, R. Niu, L. Sang, X. Liao, D. R. G. Mitchell, N. Ye, J. Pei, J. F. Li, X. Wang, *Adv. Energy Mater.* **2020**, *10*, 2000757.
- [148] S. M. K. Nazrul Islam, M. Li, U. Aydemir, X. Shi, L. Chen, G. J. Snyder, X. Wang, *J. Mater. Chem. A* **2018**, *6*, 18409.
- [149] M. Li, S. M. K. N. Islam, M. Yahyaoglu, D. Pan, X. Shi, L. Chen, U. Aydemir, X. Wang, *InfoMat* **2019**, *1*, 108.
- [150] R. D. Schmidt, E. D. Case, L. D. Zhao, M. G. Kanatzidis, *J. Mater. Sci.* **2015**, *50*, 1770.
- [151] K. F. Cai, C. W. Nan, *Ceram. Int.* **2000**, *26*, 523.
- [152] H. R. Williams, R. M. Ambrosi, K. Chen, U. Friedman, H. Ning, M. J. Reece, M. C. Robbins, K. Simpson, K. Stephenson, *J. Alloys Compd.* **2015**, *626*, 368.
- [153] H. Ju, J. Kim, *Ceram. Int.* **2016**, *42*, 9550.
- [154] F. Tseng, S. Li, C. Wu, Y. Pan, L. Li, *J. Mater. Sci.* **2016**, *51*, 5271.
- [155] J. Lei, Z. Ma, D. Zhang, Y. Chen, C. Wang, X. Yang, Z. Cheng, Y. Wang, *J. Mater. Chem. A* **2019**, *7*, 7006.
- [156] J. E. Ni, E. D. Case, R. D. Schmidt, C. I. Wu, T. P. Hogan, R. M. Trejo, E. Lara-Curzio, M. G. Kanatzidis, *Philos. Mag.* **2013**, *93*, 4412.
- [157] R. Deaquino-Lara, N. Soltani, A. Bahrami, E. Gutiérrez-Castañeda, E. García-Sánchez, M. A. L. Hernandez-Rodríguez, *Mater. Des.* **2015**, *67*, 224.
- [158] Y. Jin, X. Zhang, Y. Xiao, W. He, D. Wang, J. Li, S. Zheng, D. Ren, Y. Qiu, L.-D. Zhao, *Scr. Mater.* **2020**, *183*, 22.
- [159] R. D. Schmidt, X. Fan, E. D. Case, P. B. Sarac, *J. Mater. Sci.* **2015**, *50*, 4034.
- [160] Q. Hu, K. Wang, Y. Zhang, X. Li, H. Song, *Mater. Res. Express* **2018**, *5*, 045510.
- [161] Q. Zhang, X. Ai, W. Wang, L. Wang, W. Jiang, *Acta Mater.* **2014**, *73*, 37.
- [162] T. Dürkop, S. A. Getty, E. Cobas, M. S. Fuhrer, *Nano Lett.* **2004**, *4*, 35.
- [163] Y. Wang, J. Wu, F. Wei, *Carbon* **2003**, *41*, 2939.
- [164] H. Kinoshita, A. Ogasahara, Y. Fukuda, N. Ohmae, *Carbon* **2010**, *48*, 4403.
- [165] Z. Tang, D. Yao, D. Du, J. Ouyang, *J. Mater. Chem. C* **2020**, *8*, 2741.
- [166] T. Wei, Z. Fan, G. Luo, F. Wei, *Mater. Lett.* **2008**, *62*, 641.

- [167] *Carbon Nanotube and Related Field Emitters*, (Ed.: Y. Saito), Wiley-VCH Verlag GmbH & Co. KGaA, Weinheim, Germany **2010**.
- [168] I. Stavarache, A.-M. Lepadatu, V. Teodorescu, M. Ciurea, V. Iancu, M. Dragoman, G. Konstantinidis, R. Buiculescu, *Nanoscale Res. Lett.* **2011**, *6*, 88.
- [169] Y. Zhang, X. L. Wang, W. K. Yeoh, R. K. Zheng, C. Zhang, *Appl. Phys. Lett.* **2012**, *101*, 031909.
- [170] M. Yuan, L. Sun, X. W. Lu, P. Jiang, X. H. Bao, *Mater. Today Phys.* **2021**, *16*, 100311.
- [171] Q. Zhang, Z. Zhou, M. Dylla, M. T. Agne, Y. Pei, L. Wang, Y. Tang, J. Liao, J. Li, S. Bai, W. Jiang, L. Chen, G. Jeffrey Snyder, *Nano Energy* **2017**, *41*, 501.
- [172] S. Kumar, D. Chaudhary, P. Kumar Dhawan, R. R. Yadav, N. Khare, *Ceram. Int.* **2017**, *43*, 14976.
- [173] H. Bark, J.-S. Kim, H. Kim, J.-H. Yim, H. Lee, *Curr. Appl. Phys.* **2013**, *13*, S111.
- [174] K. T. Kim, S. Y. Choi, E. H. Shin, K. S. Moon, H. Y. Koo, G.-G. Lee, G. H. Ha, *Carbon* **2013**, *52*, 541.
- [175] W. Di Liu, Y. Yu, M. Dargusch, Q. Liu, Z. G. Chen, *Renewable Sustainable Energy Rev.* **2021**, *141*, 110800.
- [176] Y. Zhao, Y. Li, J. Qiao, S. Jiang, P. Mao, J. Qiu, S. Kang, J. Tan, K. Tai, C. Liu, *Carbon* **2020**, *170*, 191.
- [177] C. Dreßler, R. Löhnert, J. Gonzalez-Julian, O. Guillon, J. Töpfer, S. Teichert, *J. Electron. Mater.* **2016**, *45*, 1459.
- [178] K. Ahmad, C. Wan, M. A. Al-Eshaikh, *J. Electron. Mater.* **2017**, *46*, 1348.
- [179] N. Nandihalli, S. Gorsse, H. Kleinke, *J. Solid State Chem.* **2015**, *226*, 164.
- [180] A. Schmitz, C. Schmid, J. de Boer, E. Müller, *J. Nanosci. Nanotechnol.* **2017**, *17*, 1547.
- [181] Z. Zhang, S. Wu, Y. Niu, J. Jiang, C. Wang, *J. Mater. Sci. Mater. Electron.* **2019**, *30*, 5177.
- [182] Y. Pan, G. J. Weng, S. A. Meguid, W. S. Bao, Z.-H. Zhu, A. M. S. Hamouda, *J. Appl. Phys.* **2011**, *110*, 123715.
- [183] V. Kazukauskas, V. Kalendra, C. W. Bumby, B. M. Ludbrook, A. B. Kaiser, *Phys. Status Solidi C* **2008**, *5*, 3172.
- [184] I. Alig, P. Pötschke, D. Lellingner, T. Skipa, S. Pegel, G. R. Kasaliwal, T. Villmow, *Polymer* **2012**, *53*, 4.
- [185] Z. Ounaies, C. Park, K. E. Wise, E. J. Siochi, J. S. Harrison, *Compos. Sci. Technol.* **2003**, *63*, 1637.
- [186] K. Ahmad, W. Pan, S. L. Shi, *Appl. Phys. Lett.* **2006**, *89*, 133122.
- [187] F. Ren, H. Wang, P. A. Menchhofer, J. O. Kiggans, *Appl. Phys. Lett.* **2013**, *103*, 221907.
- [188] K. Ahmad, C. Wan, *Nanotechnology* **2017**, *28*, 415402.
- [189] Y. H. Yeo, T. S. Oh, *Mater. Res. Bull.* **2014**, *58*, 54.
- [190] Q. Lognoné, F. Gascoin, *J. Alloys Compd.* **2015**, *635*, 107.
- [191] K. T. Kim, Y. S. Eom, I. Son, *J. Nanomater.* **2015**, *2015*, 202415.
- [192] J. Lei, D. Zhang, W. Guan, Z. Ma, Z. Cheng, C. Wang, Y. Wang, *Appl. Phys. Lett.* **2018**, *113*, 083901.
- [193] R. Nunna, P. Qiu, M. Yin, H. Chen, R. Hanus, Q. Song, T. Zhang, M.-Y. Chou, M. T. Agne, J. He, G. J. Snyder, X. Shi, L. Chen, *Energy Environ. Sci.* **2017**, *10*, 1928.
- [194] F. Chu, Q. Zhang, Z. Zhou, D. Hou, L. Wang, W. Jiang, *J. Alloys Compd.* **2018**, *741*, 756.
- [195] B. Khasimsaheb, N. K. Singh, S. Bathula, B. Gahtori, D. Haranath, S. Neeleshwar, *Curr. Appl. Phys.* **2017**, *17*, 306.
- [196] L. Zhao, S. M. K. N. Islam, J. Wang, D. L. Cortie, X. Wang, Z. Cheng, J. Wang, N. Ye, S. Dou, X. Shi, L. Chen, G. J. Snyder, X. Wang, *Nano Energy* **2017**, *41*, 164.
- [197] P. Che, B. Wang, C. Sun, Y. Han, W. Li, *J. Alloys Compd.* **2017**, *695*, 1908.
- [198] K. T. Kim, T. S. Min, I. Son, *J. Nanosci. Nanotechnol.* **2016**, *16*, 10777.
- [199] E. Güneş, F. Gundlach, M. T. Elm, P. J. Klar, S. Schlecht, M. S. Wickleder, E. Müller, *ACS Appl. Mater. Interfaces* **2017**, *9*, 44756.
- [200] J. Ning, J. Zhang, Y. Pan, J. Guo, *Mater. Sci. Eng., A* **2003**, *357*, 392.
- [201] M. Wang, J. Wang, Q. Chen, L. M. Peng, *Adv. Funct. Mater.* **2005**, *15*, 1825.
- [202] R. Cao, Z. Zhu, X.-J. Li, X. Hu, H. Song, *Appl. Phys. A* **2019**, *125*, 126.
- [203] L. Forró, R. Gaal, C. Grimaldi, M. Mionić, P. R. Ribič, R. Smajda, A. Magrez, *AIP Adv.* **2013**, *3*, 092117.
- [204] R. Zhang, Q. Wen, W. Qian, D. S. Su, Q. Zhang, F. Wei, *Adv. Mater.* **2011**, *23*, 3387.
- [205] M. Terrones, *Annu. Rev. Mater. Res.* **2003**, *33*, 419.
- [206] J. Zhu, J. Kim, H. Peng, J. L. Margrave, V. N. Khabashesku, E. V. Barrera, *Nano Lett.* **2003**, *3*, 1107.
- [207] S. Kumar, S. Singh, P. K. Dhawan, R. R. Yadav, N. Khare, *Nanotechnology* **2018**, *29*, 135703.
- [208] S. Li, X. Liu, C. Fang, N. Liu, D. Liu, *RSC Adv.* **2018**, *8*, 20505.
- [209] S. Han, W. Zhai, G. Chen, X. Wang, *RSC Adv.* **2014**, *4*, 29281.
- [210] M. Li, D. L. Cortie, J. Liu, D. Yu, S. M. K. N. Islam, L. Zhao, D. R. G. Mitchell, R. A. Mole, M. B. Cortie, S. Dou, X. Wang, *Nano Energy* **2018**, *53*, 993.
- [211] C. Kulsı, M. Mitra, K. Kargupta, D. Banerjee, *J. Mater. Sci. Mater. Electron.* **2019**, *30*, 1850.
- [212] H. Ju, J. Kim, *J. Alloys Compd.* **2016**, *664*, 639.
- [213] M. Li, S. M. Kazi Nazrul Islam, S. Dou, X. Wang, *J. Alloys Compd.* **2018**, *769*, 59.
- [214] A. Dey, O. P. Bajpai, A. K. Sikder, S. Chattopadhyay, M. A. Shafeeuulla Khan, *Renewable Sustainable Energy Rev.* **2016**, *53*, 653.
- [215] B. Liang, Z. Song, M. Wang, L. Wang, W. Jiang, *J. Nanomater.* **2013**, *2013*, 210767.
- [216] K. Ahmad, C. Wan, M. A. Al-Eshaikh, A. N. Kadachi, *Appl. Surf. Sci.* **2019**, *474*, 2.
- [217] M. A. Worsley, P. J. Pauzaskie, T. Y. Olson, J. Biener, J. H. Satcher, T. F. Baumann, *J. Am. Chem. Soc.* **2010**, *132*, 14067.
- [218] S.-Y. Yang, K.-H. Chang, Y.-L. Huang, Y.-F. Lee, H.-W. Tien, S.-M. Li, Y.-H. Lee, C.-H. Liu, C.-C. M. Ma, C.-C. Hu, *Electrochem. Commun.* **2012**, *14*, 39.
- [219] P. Li, Y. Liu, S. Shi, Z. Xu, W. Ma, Z. Wang, S. Liu, C. Gao, *Adv. Funct. Mater.* **2020**, *30*, 2006584.
- [220] S. S. Nanda, G. C. Papaefthymiou, D. K. Yi, *Crit. Rev. Solid State Mater. Sci.* **2015**, *40*, 291.
- [221] H. Ju, M. Kim, J. Kim, *Chem. Eng. J.* **2015**, *275*, 102.
- [222] B. Feng, J. Xie, G. Cao, T. Zhu, X. Zhao, *J. Mater. Chem. A* **2013**, *1*, 13111.
- [223] W. H. Shin, K. Ahn, M. Jeong, J. S. Yoon, J. M. Song, S. Lee, W. S. Seo, Y. S. Lim, *J. Alloys Compd.* **2017**, *718*, 342.
- [224] J. Dong, W. Liu, H. Li, X. Su, X. Tang, C. Uher, *J. Mater. Chem. A* **2013**, *1*, 12503.
- [225] L. Huang, J. Lu, D. Ma, C. Ma, B. Zhang, H. Wang, G. Wang, D. H. Gregory, X. Zhou, G. Han, *J. Mater. Chem. A* **2020**, *8*, 1394.
- [226] S. Das, P. Singha, V. A. Kulbachinskii, V. G. Kytin, G. Das, S. Janaky, A. K. Deb, S. Mukherjee, A. Maignan, S. Hebert, R. Daou, C. Narayana, S. Bandyopadhyay, A. Banerjee, *J. Mater.* **2021**, *7*, 545.
- [227] N. Xiao, X. Dong, L. Song, D. Liu, Y. Tay, S. Wu, L. J. Li, Y. Zhao, T. Yu, H. Zhang, W. Huang, H. H. Hng, P. M. Ajayan, Q. Yan, *ACS Nano* **2011**, *5*, 2749.
- [228] D. Sim, D. Liu, X. Dong, N. Xiao, S. Li, Y. Zhao, L. J. Li, Q. Yan, H. H. Hng, *J. Phys. Chem. C* **2011**, *115*, 1780.
- [229] P. Zong, R. Hanus, M. Dylla, Y. Tang, J. Liao, Q. Zhang, G. J. Snyder, L. Chen, *Energy Environ. Sci.* **2017**, *10*, 183.
- [230] P. A. Zong, X. Chen, Y. Zhu, Z. Liu, Y. Zeng, L. Chen, *J. Mater. Chem. A* **2015**, *3*, 8643.
- [231] B. Anasori, M. R. Lukatskaya, Y. Gogotsi, *Nat. Rev. Mater.* **2017**, *2*, 16098.
- [232] M. Naguib, V. N. Mochalin, M. W. Barsoum, Y. Gogotsi, *Adv. Mater.* **2014**, *26*, 992.

- [233] A. Iqbal, P. Sambyal, C. M. Koo, *Adv. Funct. Mater.* **2020**, *30*, 2000883.
- [234] J. Guo, B. Legum, B. Anasori, K. Wang, P. Lelyukh, Y. Gogotsi, C. A. Randall, *Adv. Mater.* **2018**, *30*, 1801846.
- [235] X. Lu, Q. Zhang, J. Liao, H. Chen, Y. Fan, J. Xing, S. Gu, J. Huang, J. Ma, J. Wang, L. Wang, W. Jiang, *Adv. Energy Mater.* **2020**, *10*, 1902986.
- [236] W. Ding, P. Liu, Z. Bai, Y. Wang, G. Liu, Q. Jiang, F. Jiang, P. Liu, C. Liu, J. Xu, *Adv. Mater. Interfaces* **2020**, *7*, 2001340.
- [237] Y. Lin, S. Sun, Q. Zhang, H. Shen, Q. Shao, L. Wang, W. Jiang, *Mater. Today Commun.* **2016**, *6*, 44.
- [238] M.-H. Hong, W. Han, K.-Y. Lee, H.-H. Park, *R. Soc. Open Sci.* **2019**, *6*, 181799.
- [239] S. Yoo, J. Kim, H. Moon, S. Y. Kim, D. S. Ko, W. H. Shin, S. Hwang, D. W. Jung, S. Sul, C. Kwak, J. W. Roh, W. Lee, *Nanoscale* **2017**, *9*, 7104.
- [240] T. P. Pearsall, C. A. Lee, *Phys. Rev. B* **1974**, *10*, 2190.
- [241] Y. Liu, H. Masumoto, T. Goto, *Mater. Trans.* **2004**, *45*, 3023.
- [242] Y. K. Xiao, Z. X. Li, J. Jiang, S. H. Yang, T. Zhang, Y. B. Zhai, G. J. Xu, *Key Eng. Mater.* **2012**, 512–515, 1651.
- [243] H. T. Zhu, J. Luo, J. K. Liang, *J. Mater. Chem. A* **2014**, *2*, 12821.
- [244] M. S. El-Asfoury, M. N. A. Nasr, K. Nakamura, A. Abdel-Moneim, *J. Electron. Mater.* **2018**, *47*, 242.
- [245] B. Paul, A. Kumar, P. Banerji, *J. Appl. Phys.* **2010**, *108*, 064322.
- [246] W. J. Xie, Y. G. Yan, S. Zhu, M. Zhou, S. Populoh, K. Gałazka, S. J. Poon, A. Weidenkaff, J. He, X. F. Tang, T. M. Tritt, *Acta Mater.* **2013**, *61*, 2087.
- [247] M. S. El-Asfoury, M. N. A. Nasr, K. Nakamura, A. Abdel-Moneim, *J. Alloys Compd.* **2018**, *745*, 331.
- [248] T. H. Zou, X. Y. Qin, D. Li, B. J. Ren, G. L. Sun, Y. C. Dou, Y. Y. Li, L. L. Li, J. Zhang, H. X. Xin, *J. Appl. Phys.* **2014**, *115*, 3.
- [249] S. Shimizu, K. Miwa, T. Kobayashi, Y. Tazawa, S. Ono, *Sci. Rep.* **2021**, *11*, 1637.
- [250] Y. K. Lee, Z. Luo, S. P. Cho, M. G. Kanatzidis, I. Chung, *Joule* **2019**, *3*, 719.
- [251] D. M. Mattox, in *Handbook of Physical Vapor Deposition Processing*, Elsevier, Amsterdam **2010**, pp. 195–235.
- [252] A. Baptista, F. Silva, J. Porteiro, J. Míguez, G. Pinto, *Coatings* **2018**, *8*, 402.
- [253] J. Xia, D. Zhu, X. Li, L. Wang, L. Tian, J. Li, J. Wang, X. Huang, X.-M. Meng, *Adv. Funct. Mater.* **2016**, *26*, 4673.
- [254] R. Li, J. Dui, Y. Fu, Y. Xu, S. Zhou, *Nanotechnology* **2016**, *27*, 415704.
- [255] Y. Qi, Z. Wang, M. Zhang, F. Yang, X. Wang, *J. Mater. Chem. A* **2013**, *1*, 6110.
- [256] Q. Jin, S. Jiang, Y. Zhao, D. Wang, J. Qiu, D.-M. Tang, J. Tan, D.-M. Sun, P.-X. Hou, X.-Q. Chen, K. Tai, N. Gao, C. Liu, H.-M. Cheng, X. Jiang, *Nat. Mater.* **2019**, *18*, 62.
- [257] M. C. Wingert, Z. C. Y. Chen, E. Dechaumphai, J. Moon, J.-H. Kim, J. Xiang, R. Chen, *Nano Lett.* **2011**, *11*, 5507.
- [258] F. Zhuge, T. Yanagida, N. Fukata, K. Uchida, M. Kanai, K. Nagashima, G. Meng, Y. He, S. Rahong, X. Li, T. Kawai, *J. Am. Chem. Soc.* **2014**, *136*, 14100.
- [259] M. Mattinen, P. J. King, L. Khriachtchev, K. Meinander, J. T. Gibbon, V. R. Dhanak, J. Räisänen, M. Ritala, M. Leskelä, *Small* **2018**, *14*, 1800547.
- [260] J. Chen, J. Kim, N. Poudel, B. Hou, L. Shen, H. Shi, L. Shi, S. Cronin, *Appl. Phys. Lett.* **2018**, *113*, 083904.
- [261] C. Marichy, M. Bechelary, N. Pinna, *Adv. Mater.* **2012**, *24*, 1017.
- [262] S. Li, W. Zhu, Y. Xiao, F. Pan, *Chin. J. Struct. Chem.* **2020**, *39*, 831.
- [263] K.-C. Kim, S.-S. Lim, S. H. Lee, J. Hong, D.-Y. Cho, A. Y. Mohamed, C. M. Koo, S.-H. Baek, J.-S. Kim, S. K. Kim, *ACS Nano* **2019**, *13*, 7146.
- [264] S. Li, Y. Liu, F. Liu, D. He, J. He, J. Luo, Y. Xiao, F. Pan, *Nano Energy* **2018**, *49*, 257.
- [265] S.-S. Lim, K.-C. Kim, S. Lee, H.-H. Park, S.-H. Baek, J.-S. Kim, S. K. Kim, *Coatings* **2020**, *10*, 572.
- [266] S. Li, M. Chu, W. Zhu, R. Wang, Q. Wang, F. Liu, M. Gu, Y. Xiao, F. Pan, *Nanoscale* **2020**, *12*, 1580.
- [267] Y. Zhang, S. Li, F. Liu, C. Zhang, L. Hu, W. Ao, Y. Li, J. Li, H. Xie, Y. Xiao, F. Pan, *J. Mater. Chem. A* **2019**, *7*, 26053.
- [268] S. Kim, J. An, W.-J. Lee, S. Kwon, W. Nam, N. Du, J.-M. Oh, S.-M. Koo, J. Cho, W. Shin, *Nanomaterials* **2020**, *10*, 2270.
- [269] S. García-García, A. López-Ortega, Y. Zheng, Y. Nie, K. Cho, A. Chuvilin, M. Knez, *Chem. Sci.* **2019**, *10*, 2171.
- [270] A. Zhang, B. Zhang, W. Lu, D. Xie, H. Ou, X. Han, J. Dai, X. Lu, G. Han, G. Wang, X. Zhou, *Adv. Funct. Mater.* **2018**, *28*, 1705117.
- [271] M. Ibáñez, R. Zamani, S. Gorsse, J. Fan, S. Ortega, D. Cadavid, J. R. Morante, J. Arbiol, A. Cabot, *ACS Nano* **2013**, *7*, 2573.
- [272] M. Scheele, N. Oeschler, K. Meier, A. Kornowski, C. Klinke, H. Weller, *Adv. Funct. Mater.* **2009**, *19*, 3476.
- [273] J. Lauth, F. E. S. Gorris, M. Samadi Khoshkhou, T. Chassé, W. Friedrich, V. Lebedeva, A. Meyer, C. Klinke, A. Kornowski, M. Scheele, H. Weller, *Chem. Mater.* **2016**, *28*, 1728.
- [274] Y. Min, G. Park, B. Kim, A. Giri, J. Zeng, J. W. Roh, S. Il Kim, K. H. Lee, U. Jeong, *ACS Nano* **2015**, *9*, 6843.
- [275] A. Sahu, B. Russ, N. C. Su, J. D. Forster, P. Zhou, E. S. Cho, P. Ercius, N. E. Coates, R. A. Segalman, J. J. Urban, *J. Mater. Chem. A* **2017**, *5*, 3346.
- [276] V. Sharma, G. S. Okram, D. Verma, N. P. Lalla, Y.-K. Kuo, *ACS Appl. Mater. Interfaces* **2020**, *12*, 54742.
- [277] J. Fichtner, Y. Wu, J. Hitzengerber, T. Drewello, J. Bachmann, *ECS J. Solid State Sci. Technol.* **2017**, *6*, N171.
- [278] S. Ortega, M. Ibáñez, Y. Liu, Y. Zhang, M. V. Kovalenko, D. Cadavid, A. Cabot, *Chem. Soc. Rev.* **2017**, *46*, 3510.
- [279] S. Yazdani, M. T. Pettes, *Nanotechnology* **2018**, *29*, 432001.
- [280] Y. Jin, J. Hwang, M. K. Han, W. Shon, J. S. Rhyee, S. J. Kim, *ACS Appl. Mater. Interfaces* **2020**, *12*, 36589.
- [281] J. Liu, X. Wang, L. Wang, L. Peng, *Mater. Lett.* **2014**, *117*, 49.
- [282] W.-H. Chiang, C.-Y. Hsieh, S.-C. Lo, Y.-C. Chang, T. Kawai, Y. Nonoguchi, *Carbon* **2016**, *109*, 49.
- [283] R. Jin, G. Chen, J. Pei, C. Yan, *New J. Chem.* **2012**, *36*, 2574.
- [284] C. Ou, J. Hou, T.-R. Wei, B. Jiang, S. Jiao, J.-F. Li, H. Zhu, *NPG Asia Mater.* **2015**, *7*, e182.
- [285] Z. Huang, X. Dai, Y. Yu, C. Zhou, F. Zu, *Scr. Mater.* **2016**, *118*, 19.
- [286] G. Zhang, W. Wang, X. Li, *Adv. Mater.* **2008**, *20*, 3654.
- [287] Y. Y. Wang, K. F. Cai, J. L. Yin, Y. Du, X. Yao, *Mater. Chem. Phys.* **2012**, *133*, 808.
- [288] L. Chen, Y. Zhai, H. Ding, G. Zhou, Y. Zhu, D. Hui, *Composites, Part B* **2013**, *45*, 111.
- [289] Z. Quan, Z. Luo, W. S. Loc, J. Zhang, Y. Wang, K. Yang, N. Porter, J. Lin, H. Wang, J. Fang, *J. Am. Chem. Soc.* **2011**, *133*, 17590.
- [290] M. Ibáñez, R. J. Korkosz, Z. Luo, P. Riba, D. Cadavid, S. Ortega, A. Cabot, M. G. Kanatzidis, *J. Am. Chem. Soc.* **2015**, *137*, 4046.
- [291] L.-X. Liang, Y. Deng, Y. Wang, H.-L. Gao, *J. Nanopart. Res.* **2014**, *16*, 2138.
- [292] D. Liang, H. Yang, S. W. Finefrock, Y. Wu, *Nano Lett.* **2012**, *12*, 2140.
- [293] M. Scheele, N. Oeschler, I. Veremchuk, S.-O. Peters, A. Littig, A. Kornowski, C. Klinke, H. Weller, *ACS Nano* **2011**, *5*, 8541.
- [294] S. Ortega, M. Ibáñez, D. Cadavid, A. Cabot, *Int. J. Nanotechnol.* **2014**, *11*, 955.
- [295] Z. H. Ge, P. Qin, D. He, X. Chong, D. Feng, Y. H. Ji, J. Feng, J. He, *ACS Appl. Mater. Interfaces* **2017**, *9*, 4828.
- [296] B. Xiang, J. Liu, J. Yan, M. Xia, Q. Zhang, L. Chen, J. Li, X. Y. Tan, Q. Yan, Y. Wu, *J. Mater. Chem. A* **2019**, *7*, 18458.



Shiyang He works as a Ph.D. student at Leibniz-Institute for Solid State and Materials Research in Dresden, Germany. He got his B.Sc. degree in Materials Science and Engineering from Zhengzhou University in 2017, and Master degree from Shanghai University in 2020. His research focuses on thermoelectric material surface modification using the atomic layer deposition method, flexible thermoelectric materials, and the synthesis and development of new thermoelectric materials.



Sebastian Lehmann is the powder ALD lab manager at Leibniz-Institute for Solid State and Materials Research in Dresden, Germany. In 2020, he obtained his Ph.D. in Materials Science from the Technical University Darmstadt. His current research interests include surface modification and functionalization of various powders such as metals, oxides, and semiconductors utilizing the atomic layer deposition method.



Amin Bahrami is an Alexander von Humboldt research fellow at Leibniz-Institute for Solid State and Materials Research in Dresden, Germany. In 2016 he received his Ph.D. in Materials Science from CINVESTAV (México). He worked as a post-doctoral researcher at Universidad Nacional Autónoma de México (UNAM) until end of 2018. His present research activity is focused on the synthesis of new bulk and thin film thermoelectric materials and surface modification of thermoelectric materials using ALD method.



Kornelius Nielsch has studied physics at the University Duisburg and received the Master degree from Lund University in 1997. For Ph.D. he joined the Goesele group at the Max-Planck-Institute Halle. In 2002/2003, he worked as a postdoc at MIT. Subsequently, he led a young investigator group at Max-Planck-Institute Halle. In 2006, the Hamburg University has appointed him as W2 professor. In 2015, he became the director of the Institute of Metallic Materials at IFW Dresden.